# **Technical Report**

# High-resolution Lidar Observations of Rookery Islands in the Upper Laguna Madre to Define a Monitoring

# **Prepared For:**

Texas General Land Office
Coastal Management Program Cycle 19
TGLO Contract # 15-050-000-8395
(Reporting Period: October 2014 to June 30, 2016)







# **Principal Investigator:**

Dr. Michael Starek
Texas A&M University-Corpus Christi
School of Engineering and Computing Sciences
MANTIS Research Lab



Conrad Blucher Institute
6300 Ocean Drive, Unit 5868, Corpus Christi, TX 78412
Ph: 361-825-2714, Fax: 361-825-5848, Email: michael.starek@tamucc.edu

#### Acknowledgement

This report was funded in part, through a grant agreement from the Texas General Land Office, Coastal Management Program, by a grant provided by the Office of Ocean and Coastal Resource Management under the Coastal Zone Management Act of 1972, as amended, National Oceanic and Atmospheric Administration Award No. NA14NOS4190139; TGLO Contract No. 15-050-000-8395. The views, statements, findings, conclusions and recommendations expressed herein are those of the author(s) and do not necessarily reflect the views of the State of Texas, NOAA or any of their subagencies.

# **Table of Contents**

1. Project Overview	3
2. Background	5
3. Lidar Survey (Task 1)	7
3.1 Introduction	7
3.2 Survey Parameters	7
3.3 RTK GPS Survey	ε
3.4 Methodology	9
3.5 Results	10
3.6 Conclusion	13
4. Derelict Structure Mapping in Shamrock Cove (Task 2)	14
4.1 Introduction	14
4.2 Study Area	14
4.3 Data Set	14
4.4 Methods	15
4.5 Results	24
4.6 Conclusion	32
5. Rookery Island Characterization and Vulnerability (Task 3, 4, 5)	34
5.1 Introduction	34
5.2 Methods	36
5.3 Results	43
5.4 Conclusion	44
6. Conclusion	46
7. Acknowledgements	47
8. References	48
Appendix A. RTK GPS vs. LiDAR Statistics	50
Appendix B. Results from Bathymetric DEM Interpolation at Shamrock Cove	52
Appendix C. SLAMM SLR Inundation Models of the Upper Laguna Madre	
Appendix D. Data Dissemination for Web Accessibility	
Appendix E. Conference Presentations and Publications	

# 1. Project Overview

Numerous small islands in the Upper Laguna Madre are used as rookeries by a diversity of colonial waterbird species including skimmers, terns, egrets, and pelicans. Colonial waterbird populations are key environmental indicators of an estuary system's health. Communities along the Texas coast enjoy economic benefits from birding ecotourism, especially colonial waterbirds. However, recent studies show a dramatic decline in certain colonial waterbird populations in the region.

The majority of rookeries in the Upper Laguna Madre are spoil islands created from dredged material. Due to their low elevation and small extent, these islands are vulnerable to wave-driven erosion, storm impact, and relative sea level rise. This vulnerability is expected to amplify with a projected growth in sea level rise. Resource managers concerned with impacts of habitat loss on colonial waterbird populations stress the need for detailed information about rookery island topography. Presently, only very sparse elevation data exists. Without baseline topographic data, resource managers are limited in their ability to effectively characterize nesting habitat.

This project utilizes airborne light detection and ranging (lidar) measurements of island topography within the Upper Laguna Madre to characterize rookery vulnerability. The analysis targets the chain of islands near the JFK causeway and along the Intracoastal Waterway from Corpus Christi bay south to the land bridge below Baffin Bay (~120 sq. km). Figure 1 shows the project study area.

The lidar data was collected over the study region by the University of Texas (UT) Bureau Of Economic Geology (BEG). The BEG provides research-grade lidar data. Research-grade refers to quality standards that exceed industry standards with targeted vertical accuracies of < 10 cm. This level of accuracy is important for mapping rookery islands where subtle changes in elevation can result in submergence of nesting habitat. The BEG has a new state-of-the-art topo-bathymetric lidar system called, Chiroptera. The system is designed for high-resolution (sub-meter), simultaneous mapping of terrain and shallow-water bathymetry.

Success of the project is measured by the following deliverables: (1) high-resolution digital elevation models of island terrain; (2) GIS-layer to describe island morphometrics; and (3) inundation maps of island vulnerability to sea level rise. The project outputs can be applied by resource managers to monitor island evolution, identify vulnerable habitat or alternative habitat, derive new understanding about nesting and landscape interaction, and assess coastal hazards impacts.

As a separate component to this project, UT BEG conducted a lower altitude bathymetric lidar survey of a small area (~20 square kilometers) around Shamrock Island located on the northern edge of the study zone in support of regional Texas General Land Office (TGLO) initiatives (see Figure 1). The purpose of this survey is to investigate the potential of bathymetric lidar and aerial imagery in fusion to map submerged structures. TGLO has an initiative to detect and remove derelict structures (e.g. abandoned pipelines) in the region that pose a hazard to recreation and navigation.

Success of the project for this second component is measured by the following deliverables: (1) high-resolution topo-bathymetric digital elevation models of exposed and submerged features; (2) GIS polygon shapefile of delineated submerged pipelines and derelict structures.

The purpose of this report is to provide technical details on the methods and results of the approaches utilized to meet the required deliverable tasks as outlined in the agreed scope of work. Details on deliverable production time frames and stakeholder outreach are outlined in the quarterly progress reports. Appendix D provides details on web-based data hosting and dissemination of project deliverables.

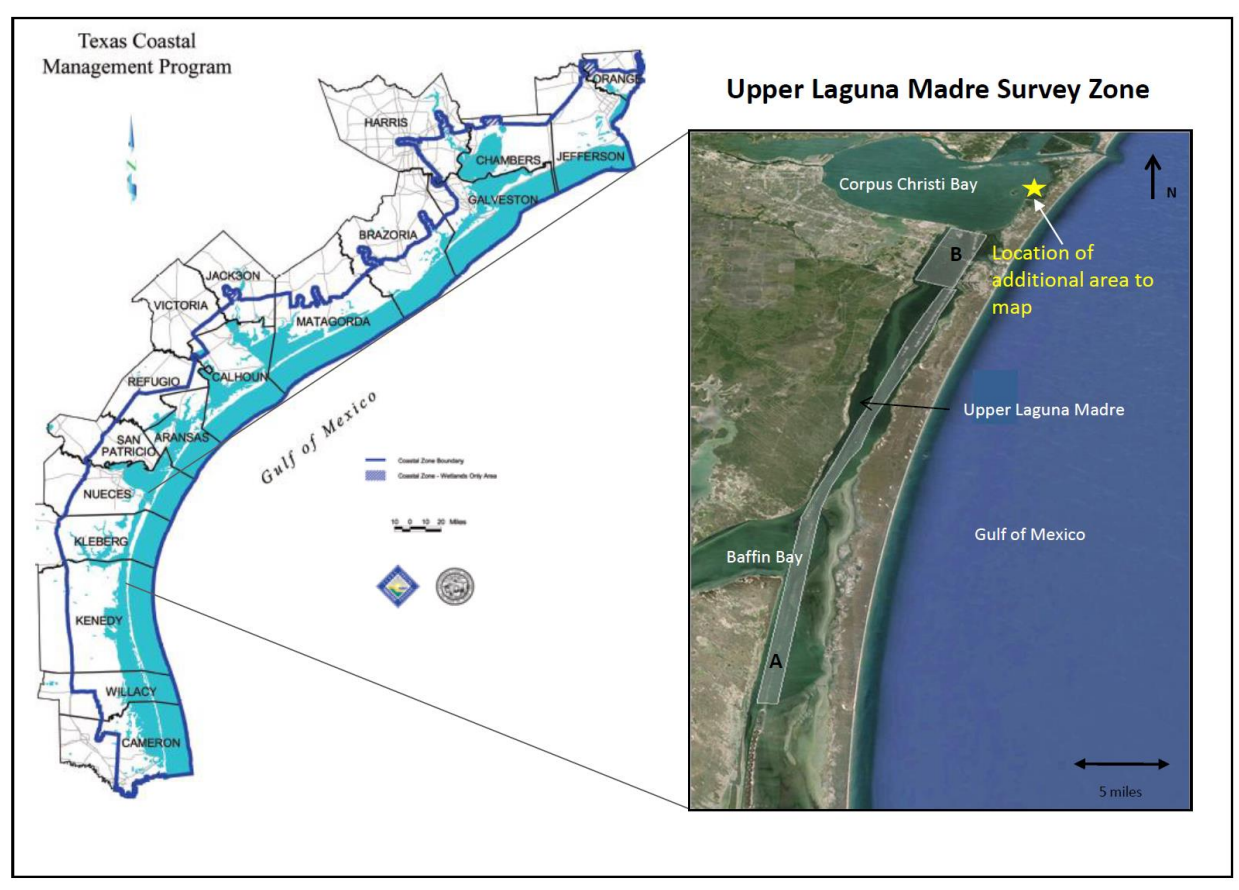
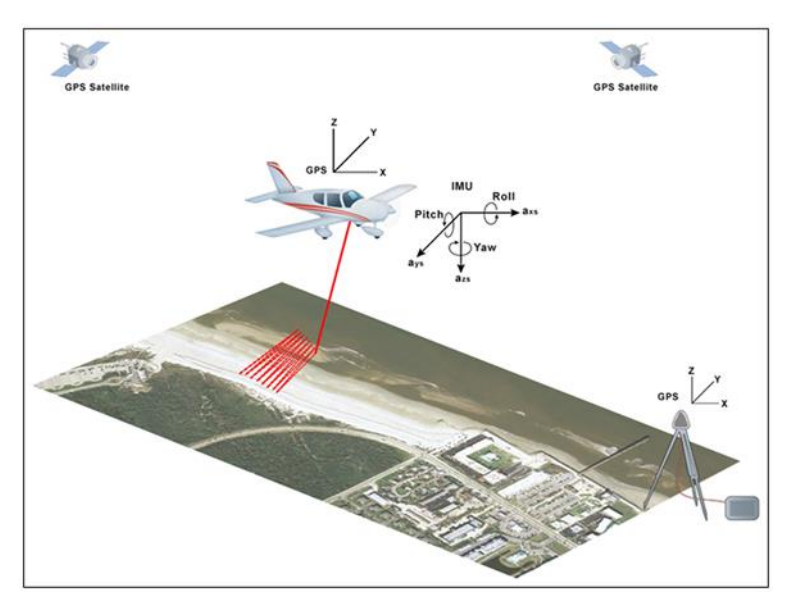


Figure 1. Map on right shows the Lidar survey area for rookery island vulnerability assessment. Zone A focuses on islands along the Intracoastal Waterway from the JFK Causeway south to the land bridge entrance (~80sq.km). Zone B focuses on islands north and south of the JFK Causeway (~40 sq.km). The star shows the location of the bathymetric lidar survey around Shamrock Island in Corpus Christi Bay, which relates to the second component of this project to map derelict structures in that area.

# 2. Background

Airborne scanning light detection and ranging (lidar) is a method that pulses a laser to measure the range between an airborne platform and the Earth's surface many thousands of times per second. Light travels approximately 30 centimeters in one nanosecond. By accurately timing the round trip travel time of the light pulses from the laser to a reflecting surface it is possible to determine the distance from the laser to the target. Because it is active, unlike aerial photography, it does not depend on ambient light which makes it operable during day or night. Using a rotating mirror or other scanning mechanism inside the laser transmitter, the laser pulses can be made to sweep through an angle, tracing out a line or other pattern on the reflecting surface. With the scan line oriented perpendicular to the direction of flight, it produces a saw tooth pattern of ranges within a strip centered directly along the flight path (Figure 2). The aircraft position and orientation information is then combined with the scan angle and round-trip travel time for each pulse to determine the geo-referenced location of the sample points on the reflecting surface [1],[2]. The result is a densely sampled, three-dimensional representation (point cloud) of the ground and land cover.



**Figure 2.** Illustration of a light aircraft collecting topographic lidar data over a beach. An onboard oscillating mirror distributes infrared laser pulses generating a saw-tooth pattern. GPS receivers onboard the aircraft and at a location on the ground are used to determine the instantaneous location of the aircraft. The orientation (roll, pitch, yaw) of the sensor head is determined from an inertial measurement unit. The position and orientation information along with the scanner angle and measured ranges are integrated to determine the x,y,z georeferenced coordinates of the illuminated surface points.

Airborne lidar has revolutionized coastal monitoring making it possible to measure three-dimensional changes in topography at spatial resolutions needed to advance science and monitor erosion along coastlines efficiently and accurately [3],[4]. This revolution has been propelled by topographic lidar systems that operate in the near-IR portion of the electromagnetic spectrum and bathymetric systems that operate in the blue-green range of the spectrum [5],[6]. Small-footprint, discrete-return systems enable beach and upland mapping with average spatial resolutions greater than 1 point per m² and achievable positional accuracies of 15-30 cm horizontal (x, y) and 5–10 cm vertical (z) [3],[4]. However, point density will vary locally depending on flight parameters, scan angle, beam divergence, surface properties, and pulse repetition rate among other factors [5].

Numerous studies have demonstrated the application of repeat lidar surveys for quantifying spatial patterns in landform evolution and coastal erosion (e.g. [4], [7], [8], [9], [10], [11]). Generally this is accomplished by differencing lidar-derived digital elevation models (DEMs) or contour vectors to estimate change in sediment volume or shoreline position between surveys. In addition to elevation change, many different morphometric parameters can be extracted for the scanned landscape, such as slope, surface roughness, or volume.

Lidar surveys generate irregularly spaced x,y,z point cloud data representing the ground and landcover. The desired end-product for many scientific and engineering applications is to derive a bare-earth DEM from the data. Modern discrete-return lidar systems record multiple returns per transmitted pulse (including first and last). Typically, only the last return points are utilized for generating bare-earth DEMs under canopy because they have a higher probability of reflecting from the true ground surface. Prior to DEM generation, the point data typically undergo a computational process called filtering to try and remove non-ground points due to such things as buildings, vegetation and other occluding objects. Many different filtering algorithms have been proposed for airborne lidar data; however, no single filter or filter parameter setting is ideal for all data scenarios or terrain types (e.g. [12]). Once the ground points are obtained through filtering, a spatial interpolation method is applied to generate a regularly spaced grid of bare-earth elevations (Figure 3). The achievable spatial resolution of the resultant bare-earth DEMs will depend on the lidar system sampling density and properties of the landcover but achievable resolutions can easily exceed 1 meter. In addition to bare-earth DEMs, the first return, non-filtered points are often used to generate digital surface models (DSMs) of the landcover elevation, such as forest canopy or buildings in urban areas. Furthermore, the lidar intensity values for each point can be used to derive texture information about the relative surface reflectance and applied to segment objects captured in the point cloud data.

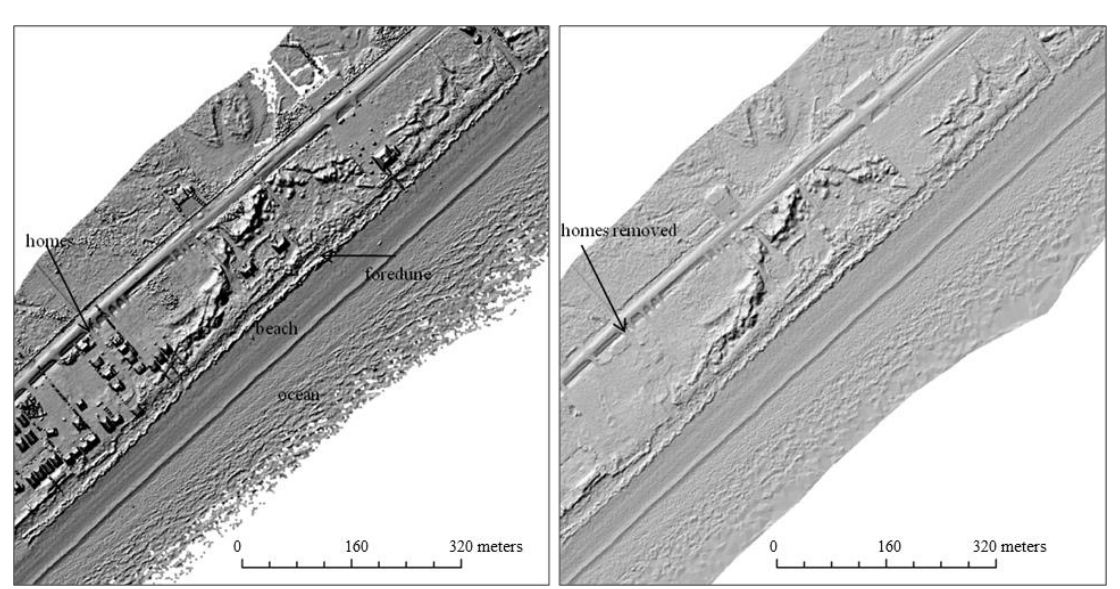


**Figure 3.** (Left) Shaded-relief image of an ALTM-derived 1-m resolution digital elevation model (DEM) of a section of beach along the Texas coast. (Right) Objects, such as homes and vegetation, can be removed through a process called filtering to generate a bare-earth DEM.

# 3. Lidar Survey (Task 1)

#### 3.1 Introduction

The Bureau of Economic Geology (BEG) at the University of Texas at Austin (UT) conducted an airborne light detection and ranging (lidar) survey of spoil islands focused along the intracoastal waterway of the Upper Laguna Madre region of the lower Texas coast. The survey also mapped Shamrock Island located in Corpus Christi Bay on the backside of Mustang Island, Texas. The purpose of this report is to provide a vertical accuracy assessment of the topographic and bathymetric elevation data generated by the UT BEG lidar survey based on a high accuracy RTK GPS survey for ground-validation conducted at Shamrock Island.

#### 3.2 Survey Parameters

The lidar surveys were flown in the winter of 2015. The purpose was to collect high resolution elevation data within the Upper Laguna Madre and Corpus Christi Bay region along the Intracoastal Waterway. The surveys were designed to support a maximum final post spacing of greater than 4 points per square meter over the exposed terrain. The elevation data were provided in NAVD88 orthometric heights converted using Geoid12a and georeferenced using WGS84 UTM Zone 14 meters.

Survey Dates

January 29: Upper Laguna Madre

January 30 and February 5: Shamrock Cove

All flights were conducted by the BEG at the University of Texas at Austin utilizing their topo-bathymetric aerial laser scanner called Chiroptera. The system was developed and manufactured by Airborne Hydrography AB (AHAB). The topographic LiDAR scanner operates at a wavelength of 1 um, a pulse rate as high as 400 kHz, and swath width of 28 to 40 degrees. It can operate to a maximum height of about 1500 m, allowing the system to be used to rapidly scan large areas with a range accuracy of about 2 cm over a flat target. The bathymetric LiDAR scanner operates at a shorter wavelength (0.5 um) and a lower pulse rate (36 kHz). The shorter wavelength allows the laser to penetrate water of reasonable clarity. After the laser reflects off the bottom surface and back to the source, the transit-time delay between water-surface and water bottom reflections can be used to determine water depths to a flat-bottom accuracy of about 15 cm. Also mounted in the Chiroptera chassis is a Hasselblad DigiCAM 50 megapixel natural color or color infrared camera that acquires frame images at a resolution of 8,176 by 6,132 pixels [source UT BEG metadata].

The BEG conducts their own accuracy assessment and validation of their lidar elevation products. The following is the method and quoted accuracy provided in the BEG metadata.

#### Horizontal Accuracy

Selected portions from each lidar data set were used to generate a 1m x 1m digital elevation model (DEM). Data estimated to have a horizontal accuracy of 0.01-0.05m from ground surveys using kinematic GPS techniques were superimposed on the lidar DEM and examined for any mismatch between the horizontal position of the ground GPS and the corresponding feature on the lidar DEM. Horizontal agreement between the ground kinematic GPS and the lidar was within the resolution of the 1m x 1m DEM. Opposing flight lines crossing the calibration target, roads within the survey area, and buildings with

slanted roofs are examined to remove roll, pitch, and heading errors. Several iterations of adjustments were made to minimize these errors caused by IMU misalignment [source BEG metadata].

# Vertical Accuracy

Ground GPS surveys were conducted near the lidar survey area to acquire ground truth information to refine the processing calibration file to remove elevation biases. The ground survey points are estimated to have a vertical accuracy of 0.05-0.10m. Roads or runways, which are typically flat areas with an unambiguous surface, were surveyed using kinematic GPS techniques. The lidar data set is sorted to find data points that fall within 1 m of a ground GPS survey point. In the project calibration file, slant range correction is adjusted to remove the elevation biases. The standard deviation of the final elevation differences provides estimates of the lidar precision. Water depth accuracy for flat bottom bathymetry is quoted to be 15 cm [source BEG metadata].

# 3.3 RTK GPS Survey

Researchers at Texas A&M University-Corpus Christi with the Measurement Analytics Lab (MANTIS) and Conrad Blucher Institute for Surveying and Science conducted an RTK GPS survey of Shamrock Island to perform an independent validation of the lidar bare-earth elevation product. Understanding the uncertainty in the elevation product is important for modeling its propagation into any subsequent analyses performed with the data (e.g. erosion change detection or vulnerability assessment of sea level inundation).

The GPS survey was conducted on January 29, 2015 using an Altus ASP-3 RTK dual-frequency GPS receiver, and the data were differentially corrected using the TxDOT Virtual Reference System (VRS) network. Reported mean accuracies of the positional data: horizontal < 2 cm, vertical < 4 cm. Spatial referencing was NAD83 State Plane Texas South (2011) Epoch 2010 (meters) with the elevations in NAVD88 using Geiod 12A. The survey was conducted within 24 hours of the airborne lidar survey by the BEG ensuring no natural surface change would impact elevation differences.

Cross-shore GPS transects were collected to measure elevation from the shallow water transgressing inland (Figure 4). This provided data from a variety of terrain types to assess their effects on the vertical accuracy. Over 800 independent GPS measurements were collected and used for the analysis. Landcover types included: Water (0 to 1.5 meter depth), Short Vegetation, Tall Vegetation, Shore (wet/dry line to water line at time of survey), Beach (wet/dry line to vegetation line), Marsh, Mangrove, Grass, and Cactus.



**Figure 4.** Aerial image from the UT BEG survey of Shamrock Island showing the RTK GPS profiles of bare earth elevation collected for different terrain types in the cross-shore from shallow water to vegetated and marsh inland surfaces.

# 3.4 Methodology

The last-return points from the lidar point cloud were filtered to remove non-ground points using a triangulated irregular network (TIN) densification filter based on the method in [20] implemented with LAStools post- processing software. The filter parameters were tuned based on visual inspection and comparisons of DEM shaded relief products derived from different parameter settings. Most importantly is the filter parameter called "step size", which governs the size of objects (buildings, vegetation) and level of detail to retain in the point cloud. For this work, a step size of 4 meters was determined "optimal" based on the filter tuning process. This step size allowed for the majority of above ground features to be removed while retaining the bare-earth surface area of the island (Figure 5). Seafloor points were based on the BEG classified bathymetry dataset and integrated into the model without alteration. The density of the classified ground points on land was 9.71 points per square meter enabling bare-earth DEM to be generated at a resolution of 0.25 meters. TIN natural neighbor interpolation was applied to create the DEM. After the DEM was generated, the GPS elevations were differenced from the lidar-derived DEM based on the grid cell that the point fell within [Lidar-GPS]. This was then used to compute bare-earth elevation differences.

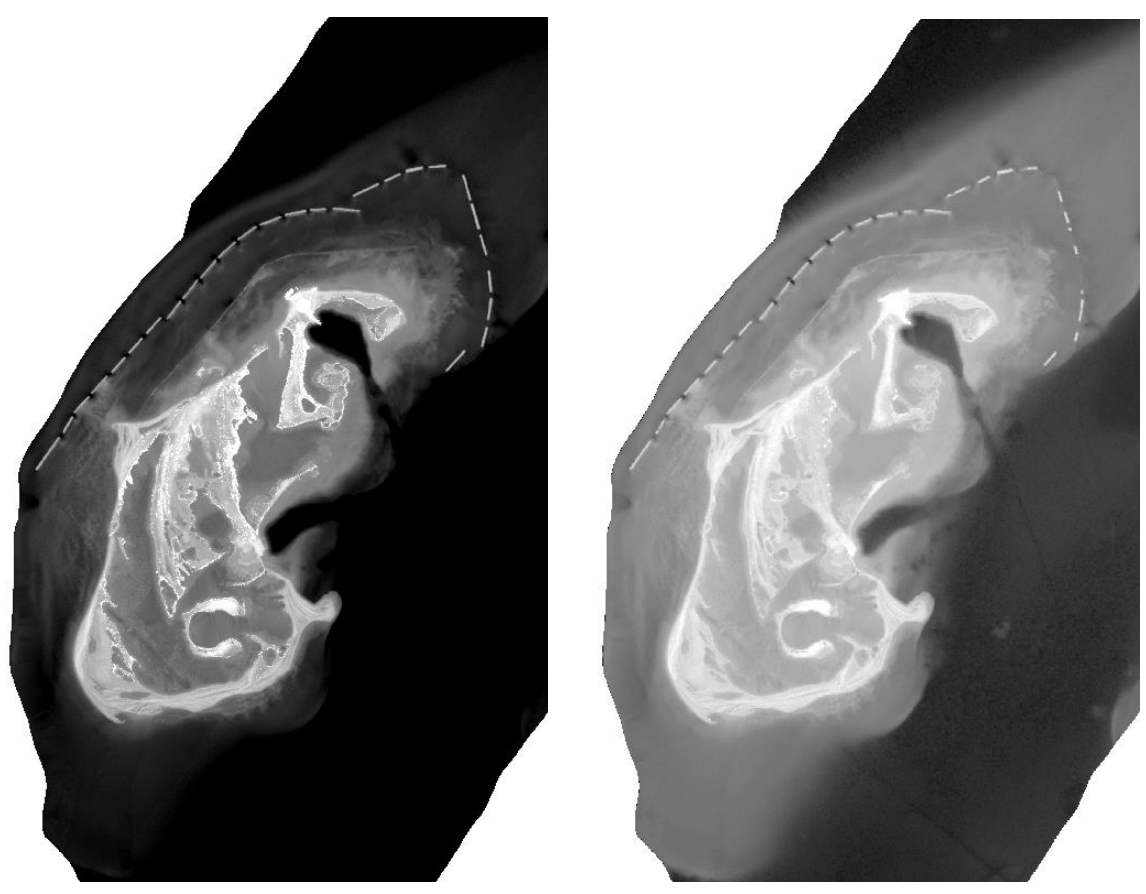


Figure 5. Example of non-filtered (left) and filtered (right) lidar-derived DEMs for Shamrock Island.

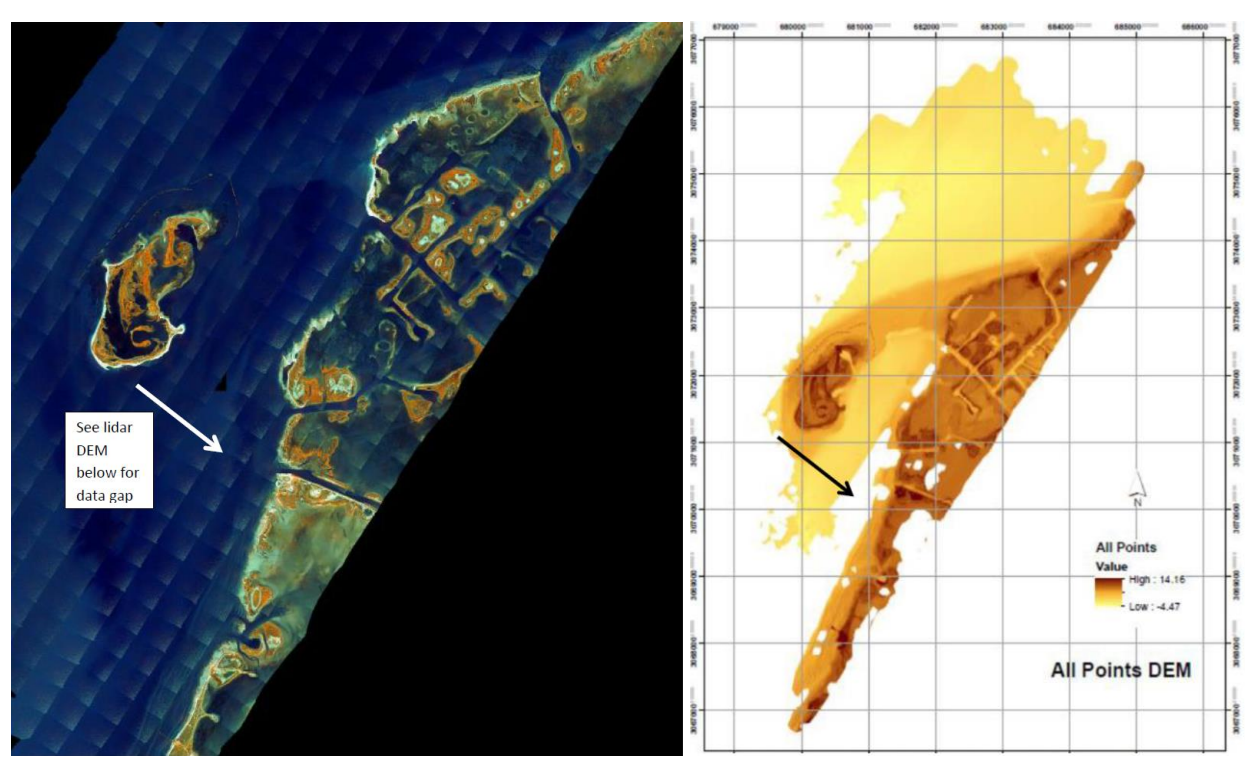
#### 3.5 Results

Table 1 shows statistics for the elevation differences computed between the lidar elevation measurements and GPS elevation measurements by landcover type. As observed, the largest RMSE between the two measurement sources occurred in the littoral zone between water and the wet/dry line. This is unexpected given that this area was exposed and non-vegetated; however, there are ridges and steeper slopes in portions of this foreshore zone. Slope amplifies lidar vertical error. Furthermore, this may be showing an effect of tidal inundation during the time of the lidar survey (recall the GPS was conducted the previous day). The second largest RMSE occurred within the mangroves and marsh landcover where we expect taller and denser vegetation cover to impact lidar accuracy. Lidar showed a mean positive bias and lower precision (more variation) in these vegetation areas. This is expected behavior for lidar over dense, short vegetation because the pulse is occluded from the bare-earth surface and becomes convolved. This typically results in a positive vertical bias of the lidar elevation points relative to the true ground surface. The mangrove also showed the largest recorded elevation difference. Lowest RMSE occurred in short vegetation and surprisingly in areas of cactus cover. The cactus cover on Shamrock has many gaps. Therefore, it is likely the laser pulse penetrated through gaps and is mostly representing bare-earth elevation in these areas. The lowest mean error occurred within short vegetation and exposed beach; the main difference being the higher variation experienced on the beach. The short vegetation resides on more uniform, flat terrain whereas the beach is more sloped and contains ridges and pockets. These differences likely led to the higher variation observed over the sandy beach. Appendix A shows histograms of the results.

Table 1. Comparison of lidar and GPS elevation data by landcover type [Lidar - GPS].

	Water	Vegetation	Tall Vegetation	Shore	Marsh	Mangrove	Grass	Contour Zero	Cactus	Beach
Count	143	117	53	33	85	66	19	6	11	274
Min (m)	-0.3711	-0.2853	-0.1746	0.1548	-0.121	-0.0115	-0.1634	0.1913	-0.0686	-0.3751
Max (m)	0.4343	0.1567	0.2364	0.3572	0.8488	0.8388	0.1263	0.3299	0.0942	0.4163
Mean (m)	0.0706	-0.0025	0.061	0.2581	0.1423	0.1983	-0.045	0.2267	0.063	-0.0423
Std Dev (m)	0.1156	0.0691	0.0807	0.0631	0.1228	0.1556	0.0729	0.0472	0.045	0.1252
RMSE (m)	0.1304	0.0691	0.1006	0.2657	0.188	0.2521	0.0857	0.2316	0.0711	0.1321

Another component of this project was to examine the use of the bathymetric lidar measurements to detect submerged pipelines in the Shamrock Cove area of the bay. Initial inspection of the bathymetric lidar survey revealed a data gap due to attenuation of the laser pulse in the water column (Figure 6). After discussions with the BEG, this data gap was determined to be caused by increased water turbidity. The first leg of the survey was mapped on January 30, 2015 during ideal water conditions; however, due to system issues the survey could not be completed. During the second phase of the survey conducted on February 5, 2015, water quality had deteriorated and turbidity increased. This region of the study area was primarily mapped on this later survey date in poor water conditions. The area also contains deeper water where the pulse will be more attenuated as it tries to propagate towards the seafloor.



**Figure 6.** (left) Location of lidar penetration gap in the aerial imagery. (right)Topo-bathymetric DEM generated from the initial UT BEG survey product at Shamrock (all points here means topographic and bathymetric). Elevation in meters.

To try and resolve more bathymetry in the data gap zone, UT BEG reprocessed the raw waveform returns over that portion of the study site using a turbid water enhancement algorithm provided by the software of the lidar system manufacture. This new dataset was provided to us and fused with the original dataset to try and derive a complete topo-bathymetric DEM for the purposes of mapping submerged structure.

Figure 7 and 8 show the results. As observed, the new dataset did provide returns from the data gap zone shown in Figure 6, but very few returns appear to reflect from the bottom. It was determined that the majority of these data points stemmed from the water column or near the surface. As such, the new dataset was not deemed useful for the purposes of pipeline detection in the data gap zone.

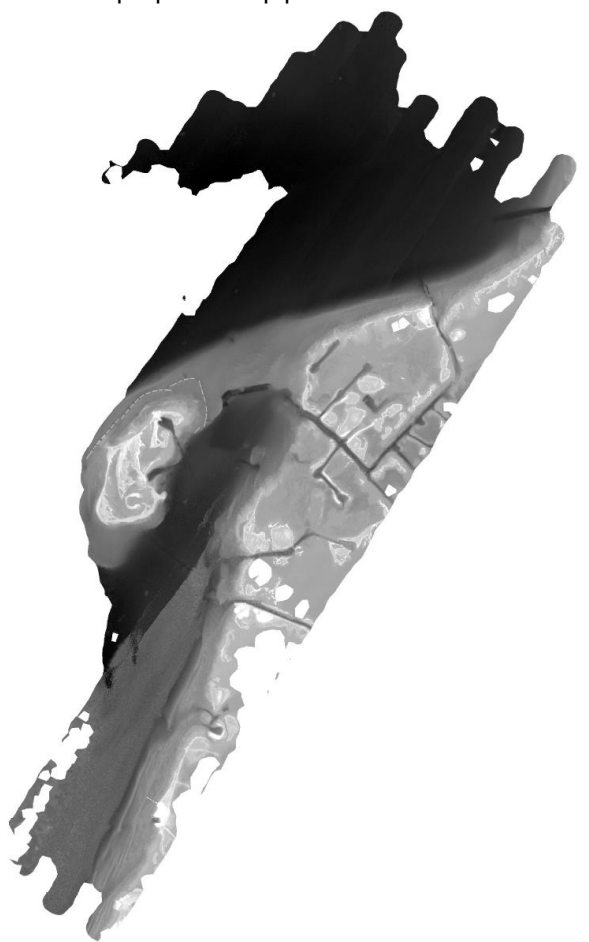


**Figure 7.** Topo-bathymetric DEM color-coded by elevation (brighter = higher elevation) at Shamrock Cove generated by fusing the "good" lidar data with the turbid water enhancement data over the data gap zone. Results show limited to no bottom detection.



**Figure 8.** Shaded relief of a topo-bathymetric DEM at Shamrock Cove generated by fusing the "good" lidar data with the turbid water enhancement data over the data gap zone. Results show limited to no bottom detection.

#### 3.6 Conclusion

This chapter provided an assessment of the UT BEG topo-bathymetric lidar survey of Shamrock Cove conducted in the winter of 2015. Vertical accuracies measured here, both in water and on land, compared fairly well with the accuracy quotes reported within the BEG metadata for exposed surfaces. However, the vertical accuracy measured here is more degraded, on average, due to the effects of landcover and terrain variability, such as vegetation and surface slope. The BEG accuracy assessment reported in the metadata is based on more exposed and flat surfaces where optimal vertical accuracy is expected. This difference is considered for the purposes of this study. Overall, given the dense sampling and high fidelity of the data, the lidar survey is deemed to be of good quality for the main objective of this study, which is to define a monitoring benchmark for vulnerability assessment of rookery islands in the region. It is reasonable to assume that the results on accuracy computed here are generalizable to the entire Upper Laguna Madre topographic lidar survey dataset collected by the BEG. This is because of the same calibration and processing procedure employed during both surveys.

# 4. Derelict Structure Mapping in Shamrock Cove (Task 2)

#### 4.1 Introduction

For this component of the project, bathymetric lidar data and airborne high resolution imagery were evaluated for their capability to map derelict submerged structures in the Shamrock Cove region of Corpus Christi Bay, TX, in support of regional TGLO clean up and mitigation efforts in the area (Ms. Amy Nunez and Mr. Tony Williams). Image enhancement methods including glint correction and edge detection were applied to improve mapping benthic structures using the aerial imagery and results compared with the lidar data.

For the bathymetric lidar data, three spatial interpolation methods including Delaunay Triangulated Irregular Network (TIN), Inverse Distance Weighted averaging (IDW), and B-spline multilevel interpolation were examined to create bathymetric digital elevation models (DEMs) from classified point cloud data. The effect of interpolation on submerged pipeline delineation utilizing the DEMs was then assessed. For the acquired aerial imagery, three different algorithms including Sobel, Prewitt, and Canny were examined in edge detection image processing to illustrate the potential pipelines and their performance quantified. Furthermore, the impact of glint correction algorithms for enhancing the visualization of submerged structures in shallow water was investigated.

# 4.2 Study Area

The study area is located in the Shamrock Cove region of the Corpus Christi Bay system along the lower-central Texas Gulf Coast (Figure 9). Corpus Christi Bay is a shallow embayment in the Texas Coastal Bend region with a flat bottom between 3 and 4 m deep over roughly 90% of the bay (Montagna and Ritter 2006; Simms et al., 2008). It is connected with the Gulf of Mexico through a narrow ship channel (15 m depth), which runs from east to west. Corpus Christi Bay is the nation's seventh largest port, with numerous petrochemical facilities (Islam et al., 2011). The importance of the study area is because of the heavy oil and gas exploration activities in the area resulting derelict structures including pipelines, which may influence the marine environment, shipping navigation, and recreational boating.

#### 4.3 Data Set

As explained in Chapter 3, the lidar data were acquired by the University of Texas Bureau of Economic Geology (BEG) on January 30<sup>th</sup> and February 5, 2015 using their Chiropetra airborne lidar system, which is developed and manufactured by Airborne Hydrography AB (AHAB). The system is capable of recording up to 4 returns per a transmitted laser pulse and enables simultaneous topographic and bathymetric scanning. The topographic lidar scanner was operated at a wavelength of 1 um, a pulse rate as high as 400 kHz while the bathymetric lidar scanner was operated at a shorter wavelength (0.5 um) and a lower pulse rate (36 kHz). The shorter wavelength allows the laser to penetrate water of reasonable clarity. Vertical accuracy for flat bottom bathymetry is quoted to be 15 cm (BEG metadata). Refer to Chapter 3 for details on the accuracy assessment of the data performed for this project. The point density for the topographic lidar data and bathymetric lidar data were approximately 7 points per square meter and 3 points per square meter respectively. The coordinate system utilized is WGS84 UTM- 14N and NAVD88 (Geoid 12) as the vertical datum.

Aerial images were also recorded using the DigiCAM 50 megapixel color infrared camera that acquires frame images at a resolution of 8,176 by 6,132 pixels. Image sets were acquired from a maximum altitude of 1500 m above ground level. The horizontal accuracy was +/- 5 meters to true ground at 95 percent confidence. The images contain three bands based on the metadata. First band is near infrared, the second one is red, and the third band is green (see Figure 6).



Figure 9. Shamrock Cove study area (source: google & TGLO website)

#### 4.4 Methods

#### 4.4.1 Bathymetric Lidar

#### Lidar Data Classification

Classification is the process of distinguishing and assigning individual 3D points to objects or terrain classes, so that in subsequent processing, surface and object modelling may be based only on the points from relevant surfaces. The last-return points from the lidar point cloud were filtered to remove nonground points using a TIN densification filter implemented (see [12]) with LAStools lidar post-processing software. The classification is important because generating a bare earth DEM from lidar and performing further analysis, such as deriving the elevation information for benthic features, is possible via classification.

Different parameter settings were examined to find a suitable combination for the given dataset. The filter parameters were tuned based on visual inspection and comparisons of DEM shaded relief products derived from the ground point set generated for different filter runs. Most importantly is the filter parameter called "step size", which governs the size of objects and level of detail to retain. Filter performance was

examined in 3, 5, 10, and 15 meter step sizes in combination with different search cases including standard, fine, and hyper fine using the LASTools ground point filter algorithm (see Table 2).

Table 2. Point cloud classification settings and results

No	STEP	SEARCHING CASE	# GROUND	# NON-GROUND
1	3m	Standard	1268270	671207
2	3m	Fine	1321125	618354
3	3m	Hyper-Fine	N/A	N/A
4	5m	Standard	1091551	847928
5	5m	Fine	1120655	818824
6	5m	Hyper-Fine	1140119	799360
7	10m	Standard	832133	1107346
8	10m	Fine	841215	1099264
9	10m	Hyper-Fine	849923	1089556
10	15m	Standard	654516	1284963
11	15m	Fine	658215	1281264
12	15m	Hyper-Fine	669681	1269798

All values in Table 2 were examined and as a result the hyper-fine case with a step size of 15 meters was determined "optimal" based on the filter tuning process. This step size allowed for the majority of above ground features to be removed while retaining the bare-earth surface area of the island. The data provided from UT-BEG was reclassified to better refine benthic characterization. The ground points in the water and land were merged and duplicate points were removed from the new data set to derive a complete topo-bathymetric DEM for the purposes of mapping submerged structure (Figure 10-11). Duplicate points might occur when two points have the same x, y coordinates and different z value or have the same x, y, and z coordinates in the data set. As shown in Figure 10, very few returns appear to reflect from the bottom in the data gap zone due to turbidity. It was determined that the majority of these data points stemmed from the water column or near the surface. As such, this area of data coverage was deemed not useful for the purposes of pipeline detection.

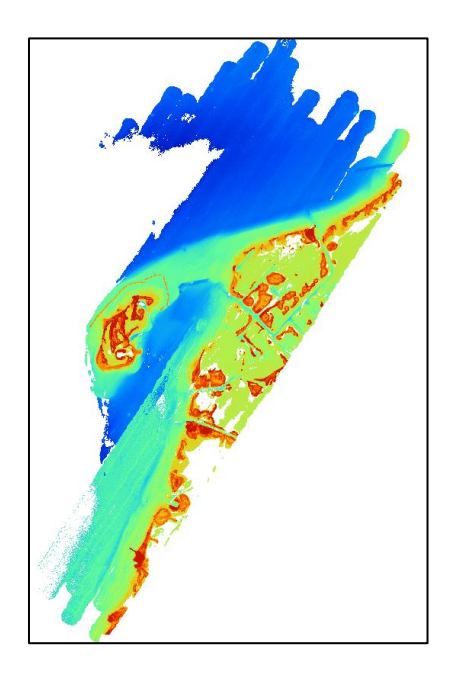


**Figure 10**. Topo-bathymetric lidar point cloud color-coded by elevation (blue = lower elevation and red = higher elevation). The color of the gap area shows the turbidity of water occluding the bottom.

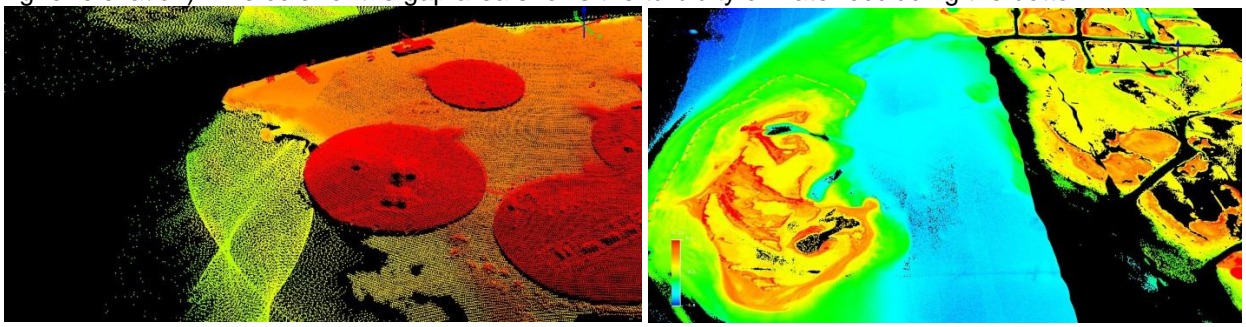


**Figure 11**. (left) Zoomed in view of the topo-bathy lidar point cloud showing oil and gas land structures. (right) Zoomed in view of the topo-bathymetric lidar point cloud color-coded by elevation (blue = lower elevation and red = higher elevation) showing Shamrock Island and the surrounding bathymetry.

#### **DEM Generation**

In this step, bathymetric DEMs from the classified lidar ground point data were created. In this study, three spatial interpolation methods were evaluated for DEM generation: multilevel B-spline, inverse distance weighted averaging (IDW), and Delaunay triangulation (TIN interpolation) [13]. Different spatial resolutions (cell size) were examined for each method: 0.50 m, 1 m, and 2 m respectively.

LASTools was used to create DEMs with TIN interpolation. For TIN interpolation, the main control parameter is the max length of a triangular edge to remove, which was set at the default of 100 m. This length is more than sufficient for the bathymetric point density here of ~3 pts per square meter.

ArcGIS was used in order to evaluate the IDW method. Several parameters are needed for this method, which are cell size, power, number of points, and maximum distance or search radius. The power is the exponent of inverse distance that controls the significance of surrounding points on the interpolated value for considering the weight. A lower power results in more influence from distant points. 'Number of point' indicates how many points should be used to perform interpolation. Maximum distance specifies the distance, in map units, by which to limit the search for the nearest input sample points. Table 3 shows the IDW parameters utilized.

Table 3. IDW interpolation parameter settings

No	Cell size	Power	Search radius
1	0.50	1	30
2	0.50	2	50
3	1	1	30
4	1	2	50
5	2	1	30
6	2	2	50

SAGA open source GIS was used to generate DEMs by multilevel B-spline method [13]. In this method two parameters are set: cell size and the maximum level that determines the maximum size of the final B-spline matrix and increases exponential with each level. This parameter can be set between 1 and 14.

Maximum level was set to 10, 11, and 12. Shaded reliefs were created for each DEM from the three interpolation methods for better visualization. A shaded relief (hillshade) is just a model for visualization derived from a DEM that is used to visualize the DEM by making it look 3D. The values of the shaded relief model no longer have any relevance to elevation and refer to shading values used by the software to view the surface to make it appear 3D. The parameters that should be mentioned in shaded relief are azimuth, altitude, and z factor. Table 4 shows the shaded relief parameters evaluated.

Table 4. Shaded relief parameter settings

No	AZ	Height	Exaggeration (Z factor)
1	315	30	1
2	315	30	2
3	315	45	1
4	315	45	2
5	315	60	1
6	315	60	2

#### Vertical Accuracy Assessment

There are many factors that affect the DEM accuracy. In other words, accuracy of a DEM derived from lidar data stems from lidar point vertical/horizontal accuracy, complexity of the terrain surface, sampling density, classification or filtering error of the data, and finally the interpolation method used to create the DEM. The overall performance of the interpolator was evaluated by the Root Mean Square Error (RMSE). In general, RMSE is calculated by observed value and predicted value as follows:

$$RMSE = \sqrt{(\frac{1}{n} \sum_{i=1}^{n} (y_{i} - \bar{y}_{i}))^{2}}$$
 (1)

where  $y_i$  is predicted value,  $\overline{y}_i$  is observed value and n is number of points in the sample. Here, observed values are RTK GPS observations and predicted values are the values of the same points derived from DEM. In other words, GPS observations were used to assess the vertical accuracy of the lidar-derived DEMs based on the different interpolation methods. The RTK GPS data collected at Shamrock Island (Figure 4) were used to assess interpolation error. 879 land and shallow water RTK measurements were collected in depths of about one meter or less, so vertical error near shore can be assessed. Refer to Chapter 3 for more details on the RTK GPS survey of Shamrock Island.

#### DEM Assessment for Delineating Submerged Pipelines

Different DEMs were created based on the three interpolation methods and by adjusting their different parameter settings including cell size. A TGLO shapefile capturing some of the existing pipelines in the area was overlaid on the DEMs to serve as ground truth and assess pipeline structure delineation. The relative performance of the different interpolation methods for segmentation was then measured.

#### 4.4.2 Aerial Imagery

The acquired imagery was exposed to varying degrees of sun glint that can occlude visibility below the water surface. Therefore, two sun glint correction algorithms were applied to the images to determine

their effectiveness in improving submerged pipeline detection: Hedley et al. (2005) and Lyzenga et al. (2006) [14], [15]. Then, edge detection image processing was applied to the imagery in order to assess their ability to help automate detection of linear features including submerged pipelines. Three different algorithms were examined including Sobel, Prewitt, and Canny. The chosen methods were run over the original and glint corrected images and results compared for pipeline delineation.

#### Sun Glint Correction

The principle of all glint correction methods is to estimate the glint contribution to the radiance meeting the sensor, and then subtract it from the received signal. There are two main categories for sun glint removal. The first category deals with resolutions at the scale of 100-1000 m which is used for Open Ocean and deep water imagery. The second category is used for coastal and shallow water images with a pixel size less than 10 m. These methods use the near-infrared (NIR) channel on the sensor to indicate the amount of glint in the received signal [16]. Based on the location of the study area, which is in shallow water, the method used in this project fell in the second category.

Hedley et al. (2005) [14] is a regression-based method that deals with NIR. Therefore, it is a suitable method for conducting sun glint removal on this data set. The method works as follows. The imagery consists of three bands, which are NIR, red, and green. Each image is split based on its components. The regression slope is calculated for each image to measure the relationship between the visible (green and red) and NIR bands. In other words, the relationship between green band and NIR is established. This same process also occurs for the red band and NIR. The pixel value is adjusted by using the following formula:

$$L_i(VIS)' = L_i(VIS) - b_i [L(NIR) - L_{min}(NIR)]$$
(2)

where  $L_i(VIS)'$ = the corrected pixel value,  $L_i(VIS)$  = the initial pixel value,  $b_i$  = the regression line slope, L(NIR) = the corresponding pixel value in NIR band and  $L_{min}$  (NIR) = the minimum NIR value existing in the sample. The corrected bands (green and red) are combined again at the end of processing. The output of this process is a deglint image. Figure 12 illustrates the processing steps in the workflow.

Lyzenga et al. (2006) [1]5 is the other algorithm in the second category that was used to conduct sun glint removal from the aerial imagery. This method uses the covariance between each visible band (green and red) and the NIR instead of the regression used in the Hedley et al. (2005) method. In addition, this algorithm uses the mean NIR in the region of interest instead of minimum NIR. This method was applied on sample images and compared with the previous method. Figure 13 shows the process of the Lyzenga et al. (2006) method.

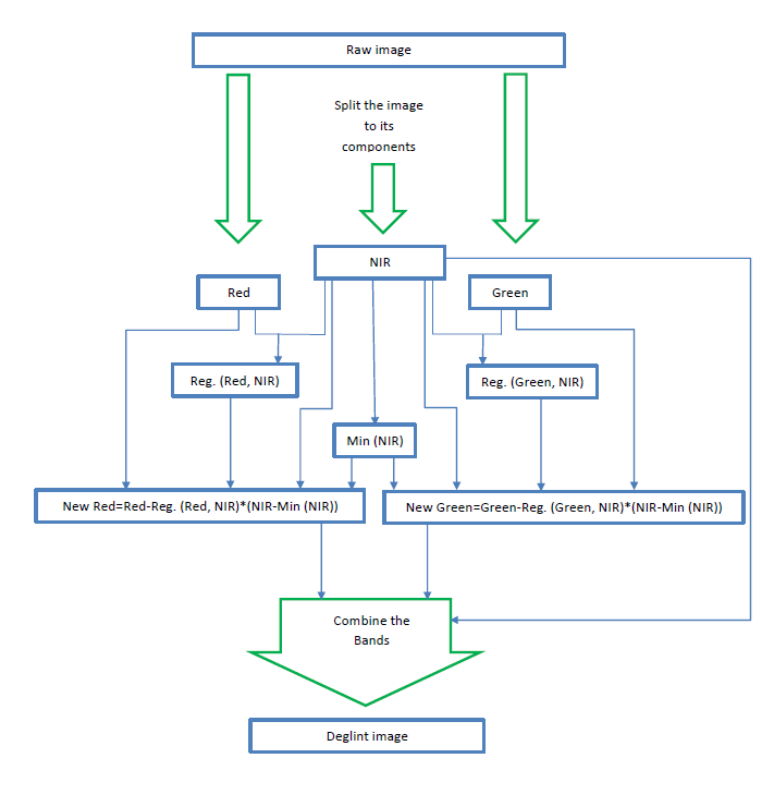


Figure 12. Flowchart of Hedley et al. (2005) algorithm for glint removal.

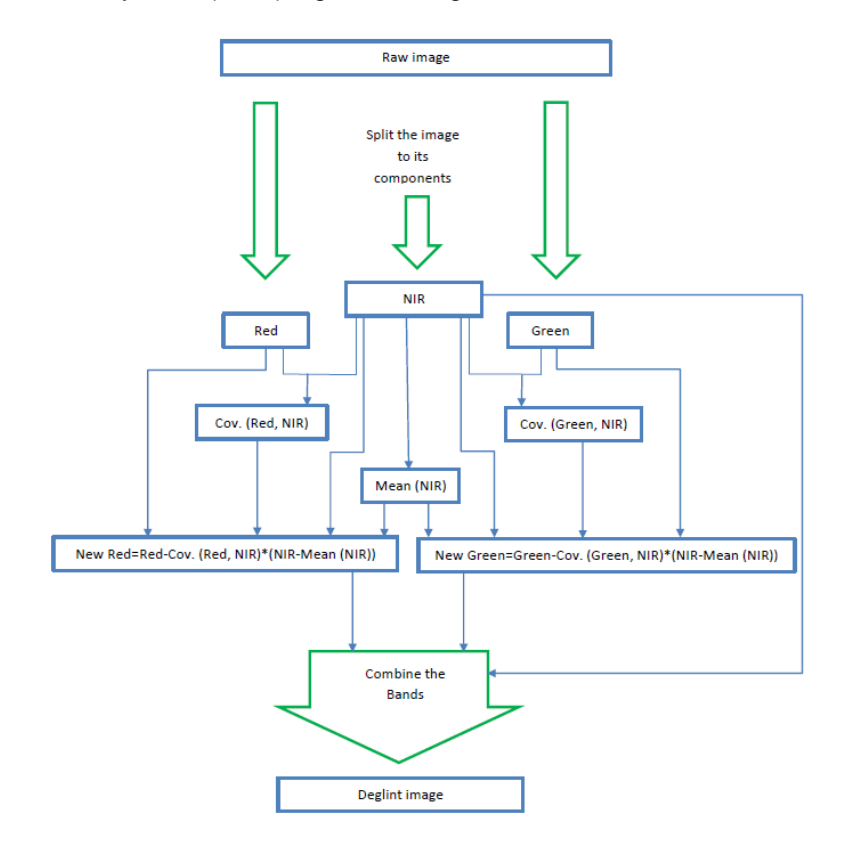


Figure 13. Flowchart of Lyzenga et al. (2006) algorithm for glint removal.

Matlab code was developed to implement these two algorithms and process the imagery. The imagery was then exported and analyzed in ArcGIS. The effectiveness of sun glint removal was examined in two ways: first, the submerged pipelines were delineated manually via visual inspection and the result compared to the submerged pipeline delineation in the original imagery (performed within ArcGIS). Second, imagery with the two glint correction methods applied was used as input into edge detection image processing discussed below. The edge detection results were compared to the original non-glint corrected imagery results in terms of noise and number of detected edges.

#### Edge Detection

In this section, three different methods (Sobel, Prewitt, and Canny) are examined to detect edges in the imagery in order to delineate submerged pipelines. In all three methods, the multiband image was converted to gray cell images and then processed. Routines were developed in Matlab to implement these algorithms. The outputs were then exported in ArcGIS to analyze and illustrate pipeline structures.

## Sobel Edge Detection

In this method, a pair of 3 x 3 convolution masks (Figure 14) is slid over the image as a focal operator manipulating a square of pixels at a time. The first convolution mask estimates gradient in the x-direction and the second estimates gradient in the y-direction. This operator works better on pixels that are closer to the center of the masks. In other words, edges of an image will contain some error because of this mask. An example for a sample image is shown in Figure 15.

-1	-2	-1
0	0	0
1	2	1

-1	0	-1
-2	0	2
-1	0	1

a) Convolution template  $S_x$ 

b) Convolution template  $S_{\nu}$ 

Figure 14. Two convolution masks in Sobel method [17].



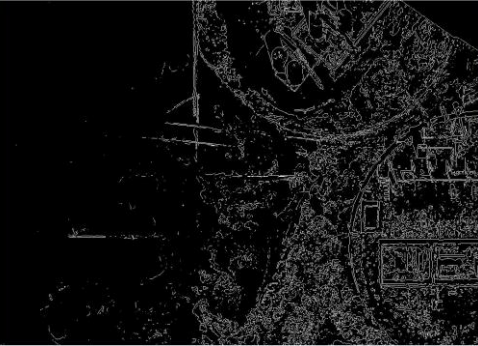


Figure 15. Sobel edge detection sample in Shamrock Cove shoreline

#### Prewitt

This method works similar to the Sobel method. However, its masks are different from the Sobel method (Figure 16). In addition, unlike the Sobel operator, Prewitt operator does not place any emphasis on pixels that are closer to the center of the masks. Sample output of the Prewitt method along the Shamrock Cove shoreline is shown in Figure 17.

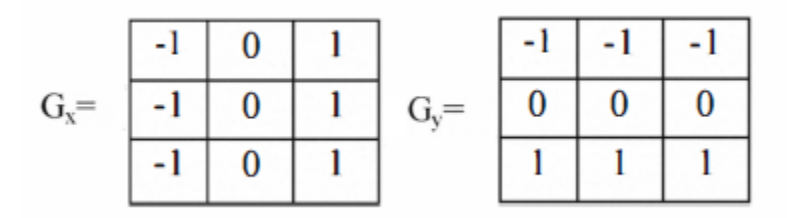


Figure 16. The horizontal and vertical Prewitt edge detection masks [18].

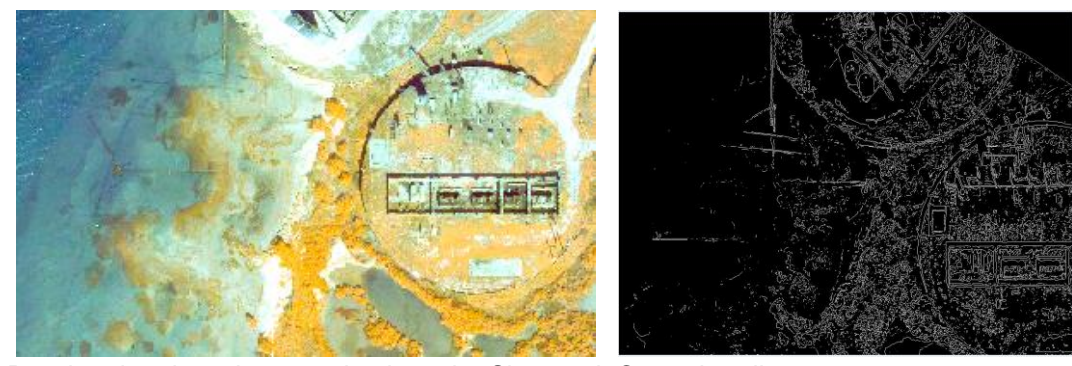


Figure 17. Prewitt edge detection sample along the Shamrock Cove shoreline.

#### Canny

Canny edge detection uses linear filtering with a Gaussian kernel to smooth noise, and then computes the edge strength and direction for each pixel in the smoothing image. In what follows, the steps of Canny edge detection are explained. In the first step, the image becomes smooth with a Gaussian filter. Then the gradient magnitude and orientation is computed using finite-difference approximations for the partial derivatives. In the last step, non-maxima suppression (thinning process) is applied to the gradient magnitude using the double thresholding algorithm (Otsu) to detect and link edges. In this process, the edge strength of each candidate edge pixel is set to zero if its edge strength is not larger than the edge strength of the two adjacent pixels in the gradient direction. Thresholding is then done on the thinned edge magnitude image using hysteresis. In hysteresis, two edge strength thresholds are used. All candidate edge pixels below the lower threshold are labeled as non-edges. All pixels above the low threshold that can be connected to any pixel above the high threshold through a chain of edge pixels are then labeled as edge pixels [19].

Canny method is a tradeoff between three parameters which are sigma, low threshold, and high threshold. By changing the value of these parameters, the connectivity and noise will be changed in the output image. These parameters were chosen here based on trial and error in terms of noise and edge connectivity in the output. Therefore, in order to find the optimal values for the parameters, different values were given to the sigma and threshold parameter to examine the noise of the output and the connectivity of the detected edges (Table 5). First, the values of low threshold and high threshold were set as [low T=.5, high T=1(pixel size)]. Then the other values were examined as [low T=5, high T=10]. In 22

this case, the output showed that most of the edges were lost. When the value of low threshold and high threshold were given 1 and 3 respectively, the results were much better when compared to other threshold values tested. Different values of sigma were examined as well. The results showed that small values of sigma that are less than one, for example 0.1 or 0.5, make more noise in the output while detection with large values resulted in blurry edges. Figure 18 shows the effect of different parameter settings on the results of the Canny edge detector. In addition, the Canny edge detector was run on deglint images using both glint removal methods and outputs compared.

**Table 5.** Canny edge detection parameter settings evaluated.

No	Operator	Sigma	Low Threshold	High Threshold
1	Canny	1	.5	1
2	Canny	1	5	15
3	Canny	1	1	3
4	Canny	0.1	1	3
5	Canny	0.5	1	3
6	Canny	2	1	3
7	Canny	5	1	3
8	Canny	10	1	3

#### Evaluating Results of Edge Detection

Two sources are used for ground truth. The first one is the existing shape file of pipelines obtained from the TGLO. The second source is submerged pipelines manually delineated using the aerial imagery. ArcGIS was used for the geodatabase and the outputs overlaid with each other. The evaluation was based on visual inspection, which means that the pipes could be confidently detected by the analyst in the imagery. To quantitatively assess performance, a set of four metrics were defined: number of edges, noise or unwanted detail, localization or displacement from the original position, and edge continuity. Noise is salt and pepper effect in the result or unwanted edges that causes ambiguity in the result. Edge continuity means the detected edge is a continuous line, not a fragmented line dependent on local scale. Noise and edge continuity are described as the attributes: High, Medium, and Low. Noise and edge continuity are not absolute. The metrics were manually measured for each result. For example, detected edges were counted manually by comparing to ground truth. Furthermore, the three edge detection methods were run over glint corrected images and results compared to the original images. The processing approach utilized was the same as the original images.

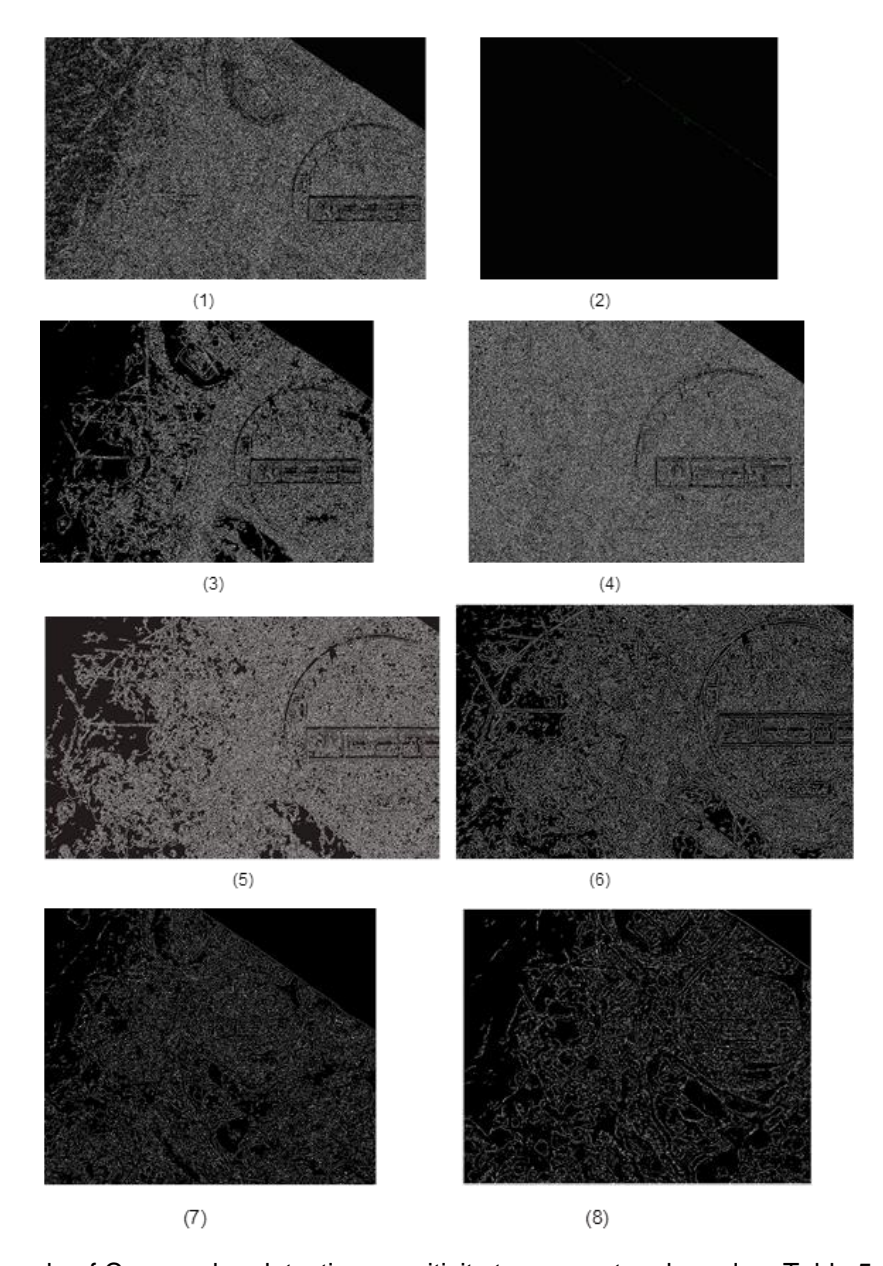


Figure 18. Example of Canny edge detection sensitivity to parameters based on Table 5.

#### 4.5 Results

# 4.5.1 Bathymetric Lidar

DEMs were generated for three cell sizes (0.50, 1, and 2 m) in each interpolation method: TIN, IDW, and B-spline. Effects of shaded relief settings for the different settings were also investigated (see Appendix B, Figures B1-B5). The output of the three methods was compared in terms of vertical accuracy and effectiveness for delineating pipelines. RMSE was calculated for each cell size (0.5, 1, and 2 m) relative to the RTK GPS points. Table 6 shows the result for each method evaluated. In addition, RMSE based on

landcover (bathymetry, land, and vegetation) was calculated for each cell size and interpolation method (Tables 7 to 9).

**Table 6.** Interpolation method vertical RMSE by cell size – all points

No	Interpolation Method	RMSE (m) Cell size =0.50 m	RMSE (m) Cell size =1 m	RMSE (m) Cell size =2 m
1	Multilevel B-Spline	0.16	0.17	0.21
2	2D Delaunay TIN	0.30	0.24	0.27
3	IDW	0.29	0.25	.28

**Table 7**. Interpolation method vertical RMSE by cell size – bathymetry

NO	Interpolation Method	RMSE (m) Cell size =0.50 m	RMSE (m) Cell size =1 m	RMSE (m) Cell size =2 m
1	Multilevel B-Spline	0.17	0.06	0.28
2	2D Delaunay TIN	0.09	0.07	0.10
3	IDW	0.10	0.14	.15

Table 8. Interpolation method vertical RMSE by cell size – exposed land

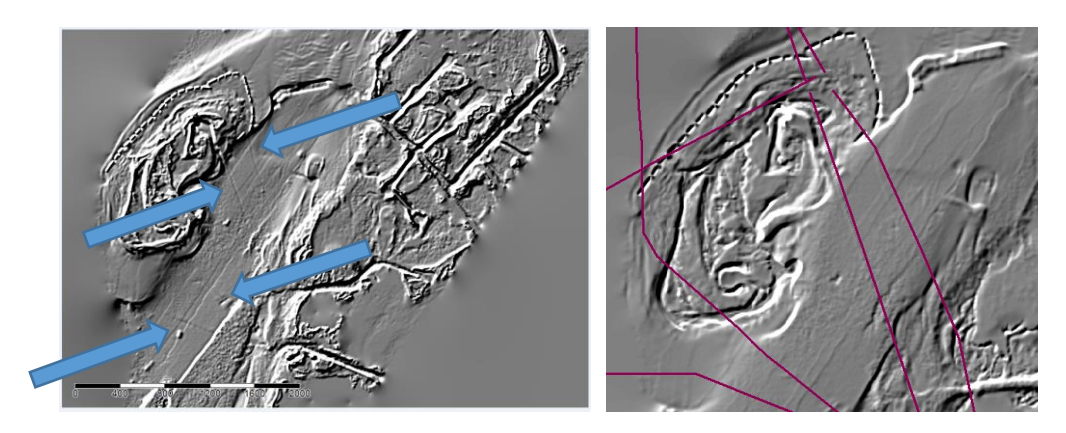
NO	Interpolation Method	RMSE (m) Cell size =0.50 m	RMSE (m) Cell size =1 m	RMSE (m) Cell size =2 m
1	Multilevel B-Spline	0.13	0.09	0.20
2	2D Delaunay TIN	0.08	80.0	0.13
3	IDW	0.13	0.28	0.31

Table 9. Interpolation method vertical RMSE by cell size – vegetated land

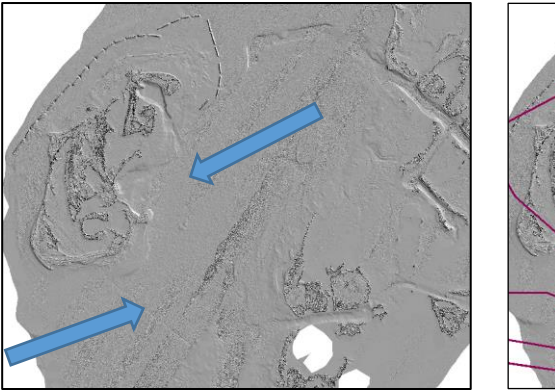
NO	Interpolation Method	RMSE (m) Cell size =0.50 m	RMSE (m) Cell size =1 m	RMSE (m) Cell size =2 m
1	Multilevel B-Spline	0.11	0.05	0.13
2	2D Delaunay TIN	0.43	0.44	0.27
3	IDW	0.15	0.06	0.30

RMSE based on all RTK GPS points showed that the multilevel B-spline method had the lowest RMSE between all three interpolation methods for all three cell sizes. In this case, it showed slightly more accurate surface reconstruction compared to the other methods tested here. In the bathymetry part, the multilevel B-spline performed best for cell size 1 m compared to TIN and IDW at the same cell size, while this method had the worst result for cell size 2 m. TIN method had the best result for RMSE over exposed land while it had the worst result in vegetation for all cell sizes. IDW had the lowest RMSE in vegetation compared to land and bathymetry.

For submerged pipeline delineation, shaded reliefs of the DEMs were generated for each interpolation method using three sun angles (30, 45, 60 degrees) and the parameter settings in Table 4. Visual inspection showed that the B-spline interpolation proved superior for this application. As shown in Figure 19, four major submerged pipelines are readily apparent in the multilevel B-spline DEM for all three cell sizes tested. In comparison, only two pipelines are readily identifiable in the 2D TIN Delaunay DEM (Figure 20) and only one pipeline is readily apparent in the IDW DEM (Figure 21). To verify results, the existing pipeline shapefile from the TGLO was overlaid on the shaded reliefs as ground truth. It should be noted that some of the pipes in the DEM do not coincide with those in the TGLO shapefile. The misplacement may occur because of differences in georeferencing accuracy between datasets. Furthermore, the shapefile dataset may have some outdated information relative to the lidar survey. The B-spline interpolation method was used to delineate pipelines in ArcGIS, because of its performance. Due to the B-spline's performance, it was used to interpolate a topo-bathymetric DEM at 1 m resolution for the purpose of delineating pipelines within ArcGIS.



**Figure 19.** (left) Results of multilevel B-spline interpolation show four major pipelines in the shaded relief DEM. (right) GLO shapefile is overlaid on the shaded relief as ground truth.



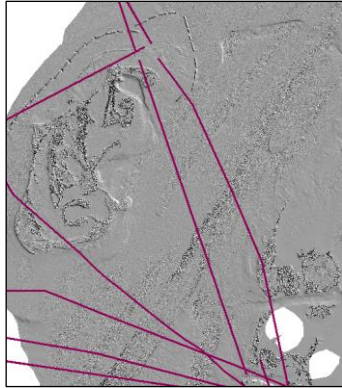


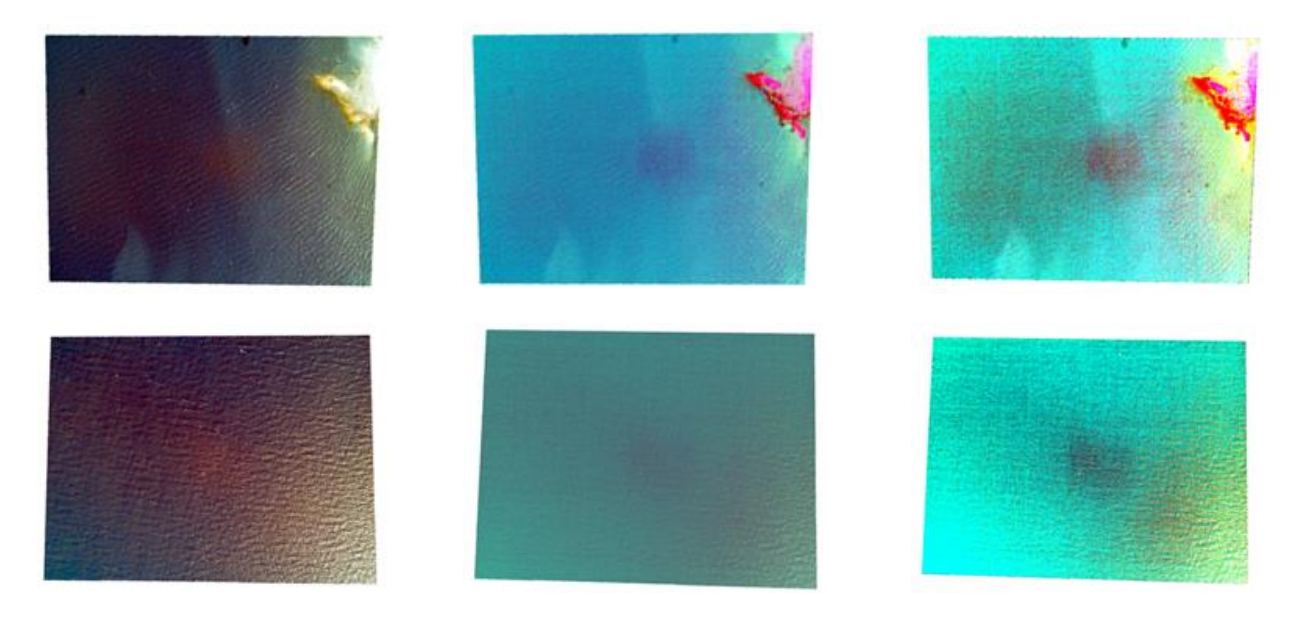
**Figure 20.** (left) Results of TIN interpolation show two major pipelines in the shaded relief DEM. (right) GLO shapefile is overlaid on the shaded relief as ground truth.



**Figure 21.** (left) Results of IDW interpolation shows only one major pipeline in the shaded relief DEM. (right) GLO shapefile is overlaid on the shaded relief as ground truth.

#### 4.5.2 Aerial Imagery – Glint Correction

Image enhancement was applied to the airborne images as a preprocessing approach prior to any further image processing. As mentioned in the methodology, two algorithms in sun glint correction were evaluated: Hedley et al. (2005) and Lyzenga et al. (2006) [14], [15]. Sun glint contamination can cause substantial loss in data fidelity below the water surface. In fact, these methods can generally only correct moderate glint and large errors may still remain in the brightest glint areas. The Hedley et al. (2005) method uses the minimum NIR in its calculations while the Lyzenga uses mean NIR. Both methods have been successful in increasing the proportion of data below the surface that can be retrieved from shallow water. Hedley et al. (2005) loses less data compared to Lyzenga et al. (2006) in the airborne imagery, because it subtracts minimum NIR from the image whereas Lyzenga et al. (2006) subtracts the average NIR from the image. Figure 22 shows sample results of glint correction by the two methods on a set of 4 images.



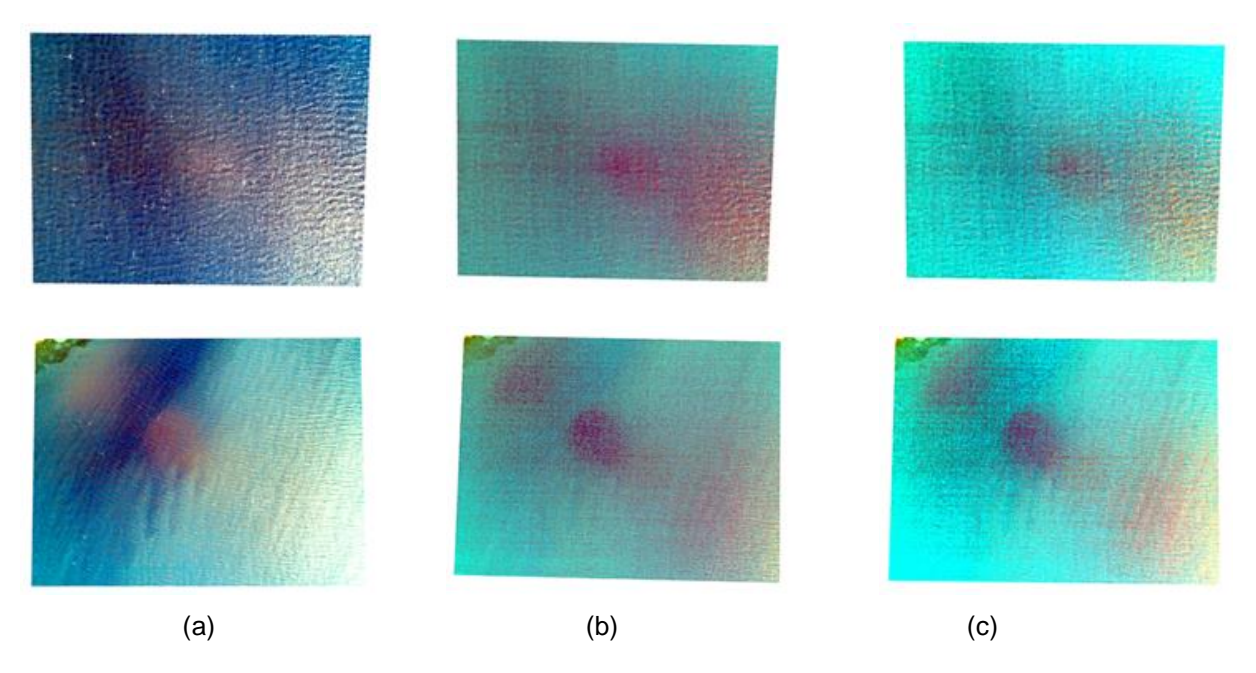


**Figure 22.** Glint results for four representative imges by the two methods. (a) Original Image, (b) Deglint Image (Hedley et al., 2005), (c) Deglint Image (Lyzenga et al., 2006) (image size 355 x 267 meters).

Sun glint occurs when sun radiation is directly reflected to the sensor over the water surface. To examine this effect, the behavior of radiation in a sample image over shallow water before and after glint correction for each method was computed. Figure 23 below shows the effect of glint removal on a sample image based on digital number value and wavelength of the three bands (NIR, Green, and Red). The result shows that the brightness decreases when glint is removed from the image due to the subtraction of digital number values from the imagery. Hedley et al. (2005) method has lower radiance compared to the Lyzenga et al. (2006) because the NIR values are taken towards the minimum value while the mean NIR is used in the Lyzenga method. Both methods were used for further processing on the data set. Figure 24 shows a mosaic of the deglint images using the Hedley method.

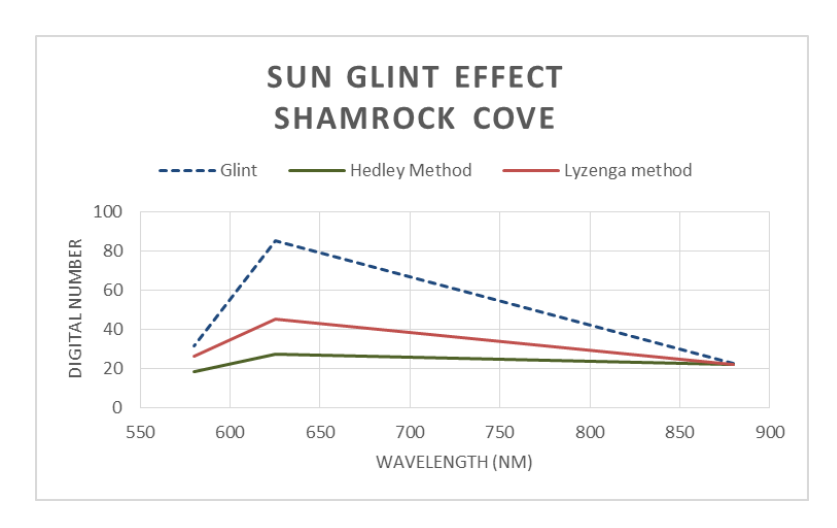


Figure 23. Sun glint removal effect on digital numbers averaged across several pixels in a sample image.

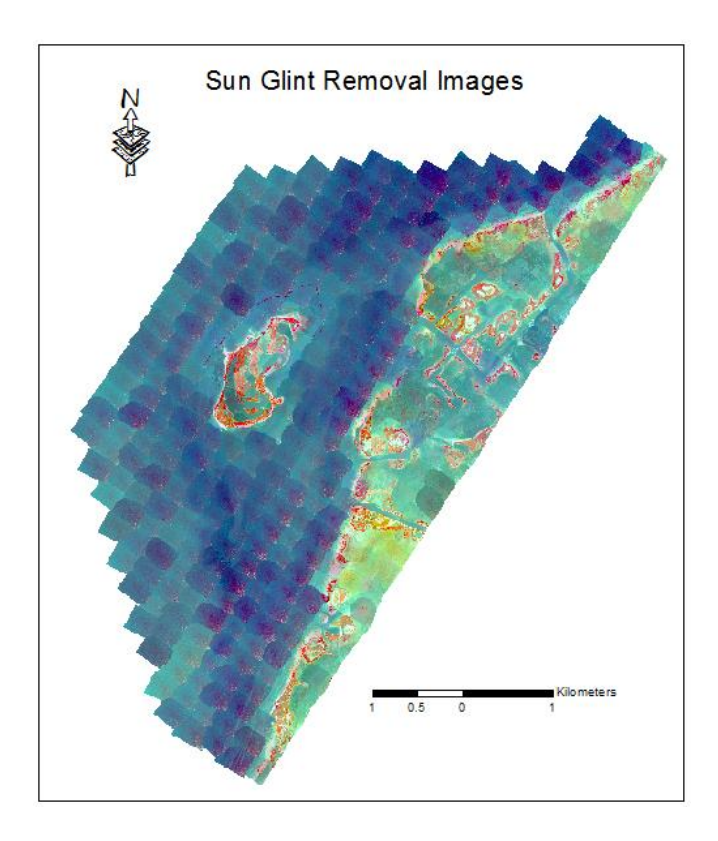


Figure 24. Deglint mosaicked data set using the Hedley method.

A shape file was created in ArcGIS and the submerged pipelines manually delineated based on visual inspection in the original and sun glint corrected imagery. Sun glint corrected imagery provided better visualization to detect the pipes. However, the number of detected pipelines was the same. In both data sets, 125 pipes were delineated.

# 4.5.3 Aerial Imagery – Edge Detection

As mentioned in the methods section, three different methods of edge detection were examined to detect submerged pipelines: Sobel, Prewitt, and Canny. Each method was assessed based on parameters including detected edges, noise, displacement from center, and edge continuity. Edge detection operations were run on the set of images and these parameters were measured manually for each result by visual inspection to ground truth in ArcGIS. The TGLO pipeline shapefile coupled with pipelines delineated using the glint corrected aerial imagery served as the "ground truth" feature class for comparison. Table 10 shows results of the evaluation for each edge detection method.

**Table 10.** Evaluation based on ground truth.

No	Approach	Edge Detection	Noise	Localization	Edge Continuity
1	Canny(1,[1,3])	74 out of 125	Medium	0.25 m off from center	High
2	Sobel	50 out of 125	Low	0.35 m off from center	Low
3	Prewitt	50 out of 125	Low	0.35 m off from center	Low

Referring to Table 10, results in this case show that Sobel and Prewitt methods work closely to each other in terms of delineating pipelines and noise. These operators can only delineate the pipelines up to 40%, although their noise is less than the Canny method (Figure 25). Canny method depends on its parameters in delineating the features. In other words, decreasing " $\sigma$ " would show more detail, and changing thresholds would change edge linkage. The parameter values of " $\sigma$ " and threshold shown in Table 5 were evaluated. Results showed that  $\sigma=1$ , Low T =1, and High T= 3 resulted in the best combination of the values tested providing more than 60% of pipelines automatically detected. Figure 26 shows the result of the Canny method.





**Figure 25.** Ground truth: Sobel edge detection (Left); Prewitt edge detection (Right); the red lines in both pictures show the ground truth.

Although Sobel and Prewitt's methods created lower noise in the image, they could not find as many edges as the Canny did. The result shows that the output of these methods is generally similar to each other. In spite of the Canny method having more noise in its results, it can detect more edges; many of which are pipelines in this case study. Therefore, neither Sobel nor Prewitt's methods were determined effective for operation on this data set. The important note is that the parameter values of Canny method in this study will not necessarily perform well on other data sets. The optimal parameter settings may vary from one data set to another. It depends on many other factors including imagery type, quality, blurring, benthic type, ambient conditions, etc.

It should be mentioned that the chance of detecting submerged features in clear water is better than turbid water due to deeper visible light penetration. Glint corrected images did not prove more useful for visual delineation of submerged pipelines in this case based on no measurable improvement in the number of pipes identified. However, edge detection algorithms were run over the two sun glint corrected images. Canny operator detected more edges compared to the original imagery, while the result did not change for the other edge detection operators. Table 11 shows the result in terms of number of detected edges in all three methods. The other evaluation parameters did not change. Results show that in spite of the output having more noise than the output on raw images, the Canny method applied to glint corrected imagery improved the ability to detect more edges (pipes) in shallow water. By removing glint from the surface water reflection, reflection through the water column and underlying surface structure below provided enough enhancement to track more linear features. Therefore, deglint imagery was helpful for edge detection image processing of this data set and resulted in the detection of more edges. Figure 27 shows an example of an extra edge detected by the Canny operator when using glint corrected imagery.

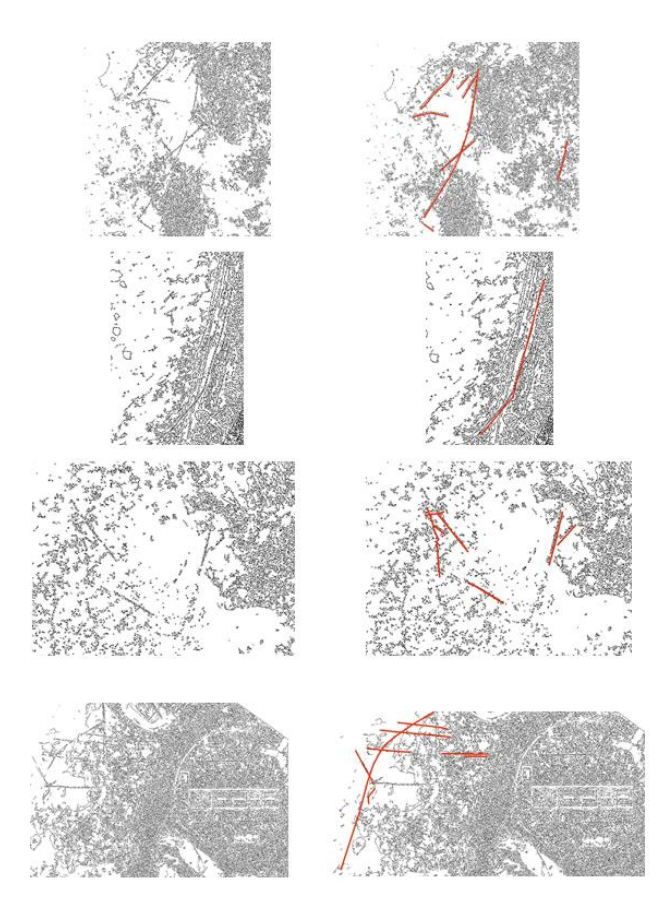


**Figure 26.** Results of Canny edge detection using the parameter settings: [1, [1, 3]]. Left column shows edge detection results for different regions. Right shows the same but with ground truth pipelines overlaid.

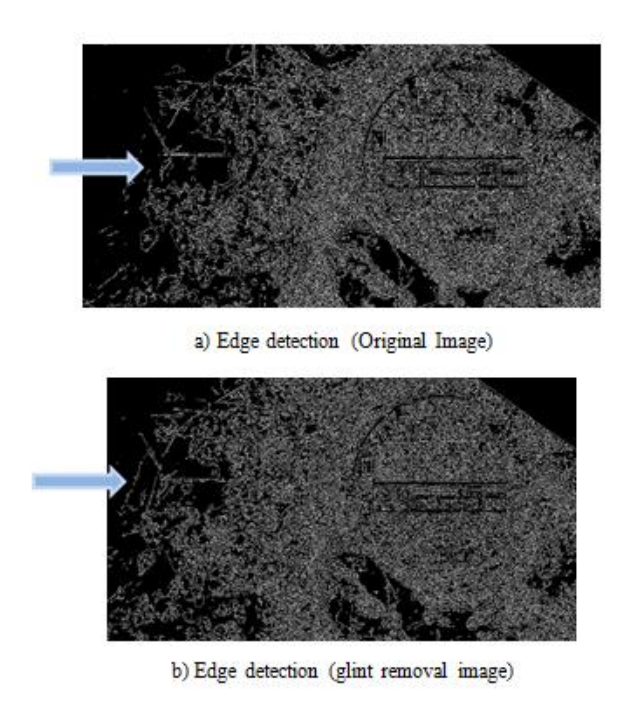


**Figure 27.** Comparing edge detection in original and deglint image sample using the Canny operator. The blue arrow shows the location of a pipe. a) Original image (with glint) b) glint corrected image.

**Table 11.** Evaluation based on ground truth-deglint imagery

No	Approach	Detected edges (Hedley	Detected edges (Lyzenga	
		2005)	2006)	
1	Canny(1,[1,3])	85 out of 125	85 out of 125	
2	Sobel	51 out of 125	50 out of 125	
3	Prewitt	50 out of 125	50 out of 125	

#### 4.6 Conclusion

Figure 28 shows the final results of pipeline delineation created by fusing pipelines manually delineated from the bathymetric lidar data and aerial imagery. Manual delineation of pipelines within the aerial imagery was enhanced using glint correction and edge detection image processing methods in fusion. Based on the results, the outputs showed that four major pipes with 8" to 12" diameter were detected by processing bathymetric lidar data and generating DEMs by B-spline interpolation (red arrows point to the pipes in Figure 28). Other pipes, which were located near shoreline, were not detected by the lidar approach. Existing features at the level of the pipes, the size of the pipes, and the turbidity of the water can interfere with detecting pipes through a lidar DEM. Also, pulse length of the lidar is a limiting factor in resolving water surface from bottom. As water depth becomes shallower the signal from the surface and features on bottom gets convolved reducing discrimination. If some features like sea grass, mud, or reef exist near or at the level of the pipes, there is not enough height difference to be distinguished in the DEM. Small pipes also could not be detected with this data set because of the point density of the bathymetric lidar data and consequently the resolution of the DEM. The most important factor is the turbidity of water, which impedes laser penetration through the water column. Edge detection image processing helped detect more pipes using visual inspection but not ones in the deeper water where turbidity limited depth penetration for passive imaging (visible bands). Therefore, only submerged pipes near the shoreline in shallower water were detected using the aerial imagery (blue arrows point to the pipes delineated from the imagery in Figure 28). In contrast, lidar was superior for detecting pipes in deeper water but restricted to larger pipes.

The bathymetric lidar dataset was deemed to be not as useful as anticipated. This was not a failure of the survey method employed by the BEG. Rather it is due to inherent limitations in current bathymetric lidar system resolvance power when trying to delineate small pipeline structures (e.g. < 6 cm) with sizes smaller than the laser diameter footprint. Based on this analysis it is recommended that future surveys targeted for this objective plan as best as possible for ideal water conditions, employ more scan overlap, and fly at minimum allowed altitudes with as high a pulse rate as is functional for dense sampling and high signal-to-noise. Nonetheless, the bathymetric lidar still proved useful in detecting larger submerged pipelines in deeper water, and coupled with the aerial imagery proved to be a value added product. Development of automated approaches and improved methods to better exploit the bathymetric lidar data for detection of submerged pipelines is a work in progress.

Based on the edge detection results, the performance of the Canny operator was better than the Sobel and Prewitt methods in terms of detecting the edges. As mentioned above, turbidity of the water is one of the impeding parameters in edge detection methods. The other issue with the edge detection methods

observed in this analysis is the existence of noise (unwanted edges) in the output. The existing noise decreased the effectiveness of the edge detection methods. Such methods will perform better if the existing noise is suppressed in one way or another using filtering and edge contiguity approaches.

Finally, two methods were used to remove the sun glint from high resolution aerial imagery, which were the Hedley et al. (2005) and the Lyzenga et al. (2006) [14], [15]. These two methods rest on the assumption that all NIR radiation is absorbed by the water, and hence the water-leaving radiance shall be zero. The accuracy of that assumption depends on local conditions; for example, in shallow or turbid water NIR radiation may be reflected into the air by the seabed or sediment before absorption. The only difference between the methods of Hedley et al. (2005) and Lyzenga et al. (2006) is how they handle the water-leaving NIR to apply the correction. Based on the results in this study, sun glint removal image preprocessing did not succeed in enhancing visual delineation of submerged pipelines as much as anticipated. However, results of the Canny edge detection method were improved for imagery with sun glint correction applied. In contrast, results for the Sobel and Prewitt methods did not change. Further analysis on the optimal synergism of these methods to improve aerial imagery of submerged structures is needed. With the advent of unmanned aircraft systems (UAS), such methods will become even more valuable for benthic mapping and hazards detection in the littoral zone.

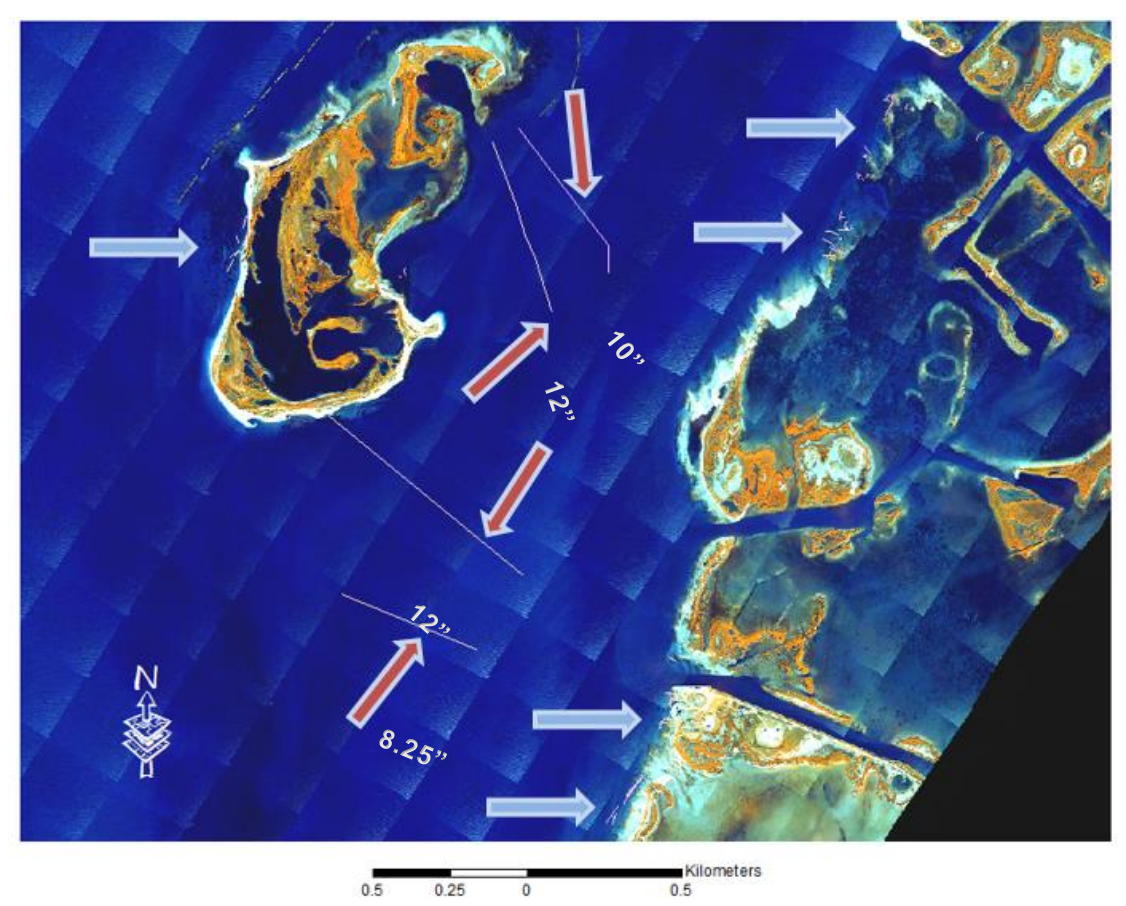


**Figure 28**. Final result of submerged pipeline delineation in Shamrock Cove overlaid on the aerial iamge mosaic. Results show structure based on a January 29, 2015 airborne lidar and imaging survey. Red arrows are detected by the lidar DEM and blue arrows are detected by aerial imagery. The size of the pipelines is provided by the TGLO GIS pipeline layer.

# 5. Rookery Island Characterization and Vulnerability (Task 3, 4, 5)

#### 5.1 Introduction

This component of the project utilizes airborne lidar measurements of spoil island topography within the Upper Laguna Madre to define a monitoring benchmark for characterization of rookery island habitat vulnerability. Due to their low elevation and small extent, these islands are vulnerable to wave-driven erosion, storm impact, and relative sea level rise (Figure 29). The area under observation for this study is a chain of islands extending from the JFK causeway and along the Intracoastal Waterway from Corpus Christi Bay south to the Land Cut below Baffin Bay (~100 sq. km). A map of the region can be seen in Figure 30 (and Figure 1). It is important to mention that not all islands in the study region serve as waterbird rookery habitat due to different factors such as their size, predation activity, and/or human activity.

The lidar data set was collected by the University Of Texas BEG on January 29, 2015 using their Chiroptera topo-bathometric LiDAR system. Only the topographic lidar points were used for this analysis. Point densities of > 4 points/m² were obtained over exposed land. Figure 31 shows an example of the topographic lidar point cloud over Shamrock Island investigated in Task 2 (refer to Chapter 4). The World Geodetic System of 1984 (WGS84) is the geodetic model for the data, which is projected using Universal Transverse Mercator (UTM) Zone 14N meters. Elevation is referenced to the North American Vertical Datum of 1988 (NAVD88, Geoid 12). Refer to Chapter 3 for more details on the lidar survey.



Figure 29. Images of spoil islands in the study site illustrating their low elevation and small extent.



Figure 30. Map showing the location and extent of the study site.

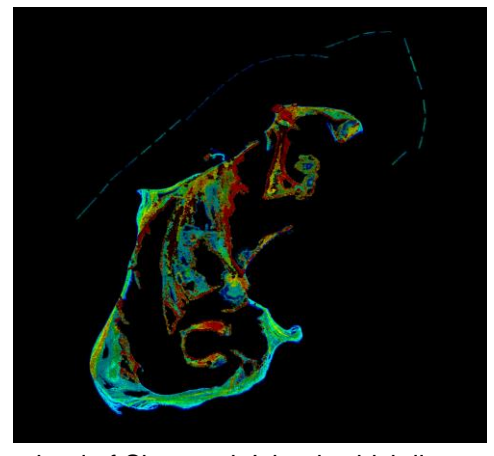


Figure 31. Topograhic lidar point cloud of Shamrock Island, which lies to the north of the study zone.

#### 5.2 Methods

There are three main tasks for this component of the project: 1) create accurate, high-resolution digital elevation models (DEM) of island terrain (Task 3 in scope of work), 2) create a GIS layer to describe spoil/rookery island morphometrics (Task 4 in scope of work), and 3) create inundation maps of island vulnerability (Task 5 in scope of work). Figure 32 shows a conceptual framework of the overall approach. Each task will be discussed in a separate section below.

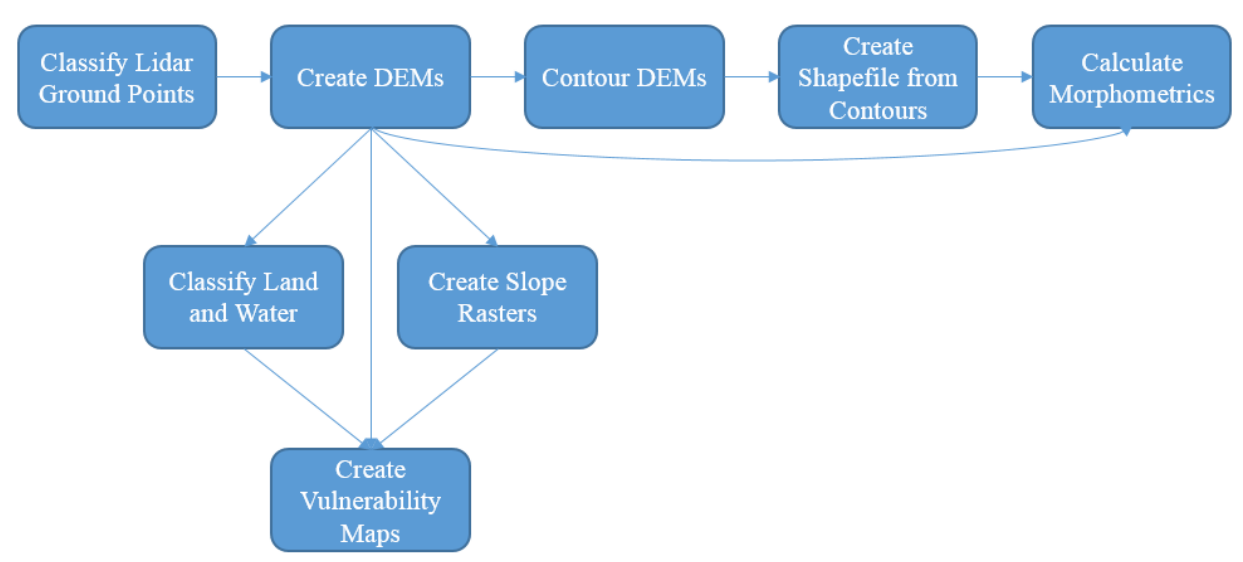


Figure 32. A conceptual framework showing the workflow for this component of the project.

#### 5.2.1 DEM Generation (Task 3)

#### Ground Point Filtering

A set of command line tools used for point cloud processing called LAStools was used to filter and process all of the point clouds. The lasground filtering tool was used to classify points into ground or nonground points for the purpose of generating bare-earth DEMs of each island. The tool implements a progressive TIN densification filter based on [20] and provides three main parameters to adjust (there are others for fine tuning): step size, intensity, and mode. The step size is an area in meters that evaluates the points that fall within it. Larger objects such as buildings can be resolved and filtered out with a larger step size and more detailed objects can be retained with a smaller step size. Larger step sizes result in more non-ground points being correctly identified and removed but at the expense of removing more true ground points. In contrast, smaller step sizes retain a larger number of ground points at the expense of retaining more non-ground features. Because of this tradeoff, the step size parameter requires tuning. Lidar data points from Shamrock Island area where the RTK GPS survey was conducted (refer to Chapter 3) were used to tune the filter step size. The point cloud was filtered with a range of step sizes and then visually analyzed in QuickTerrain Modeler, a 3D point cloud rendering software. A step size of 8 meters appeared to remove most vegetation and all of the structures without removing too many ground points. Any step size much less than 8 meters was not successful at removing dense groves of vegetation or large buildings. Filtering then took place on all of the point clouds using an 8 meter step size (Figure 33). Once the point clouds were filtered they were opened in QuickTerrain Modeler where they were quality checked to ensure that buildings and large vegetation features had been properly removed.

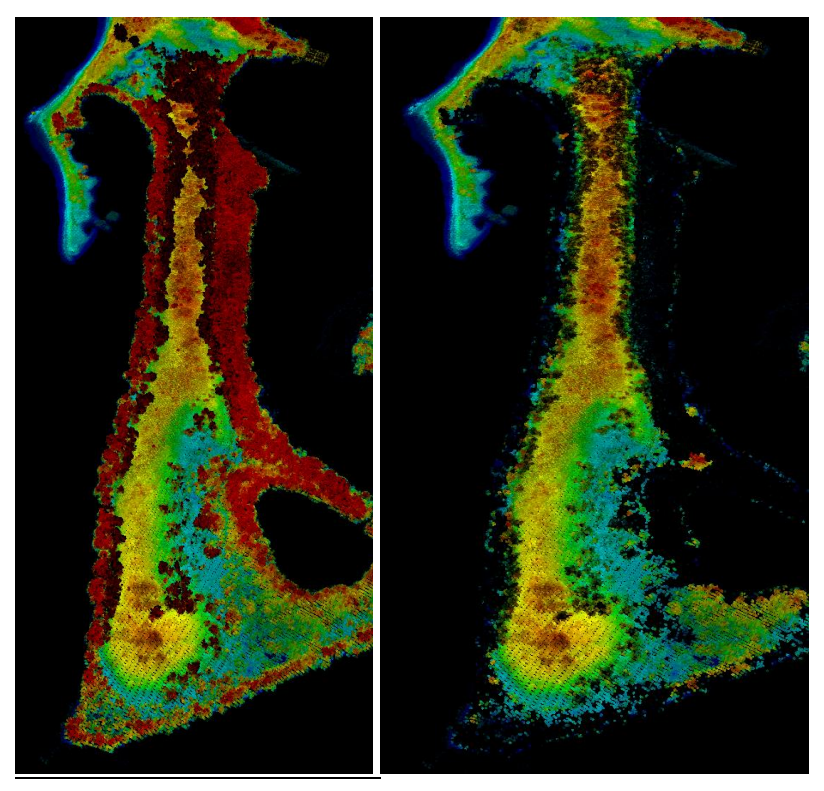
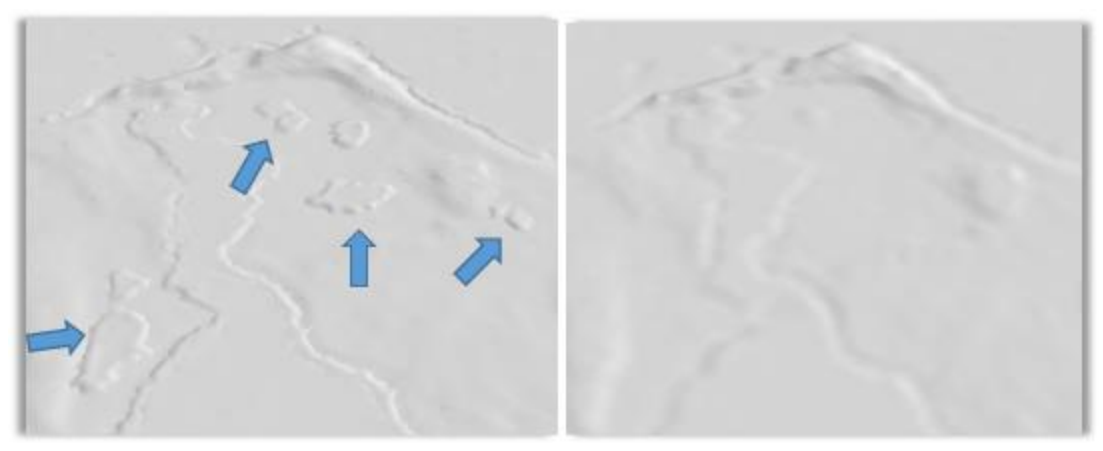


Figure 33. Images of a non-filtered (left) and filtered island point cloud (right).

### Ground Points to DEM Interpolation

LAStools offers an interpolation tool called Blast2dem. This tool is capable of reading in billions of LiDAR points from the LAS/LAZ binary formats commonly used to share lidar data. It then triangulates them into a seamless triangulated irregular network (TIN) which is then rasterized into a DEM. Only classified ground points were used for DEM creation. The resolution for all generated DEMs was set to 1 meter based on the average ground point density after filtering. A parameter was set to not allow triangles with edges greater than 50 meters to be rasterized. This was to prevent individual islands in close proximity to each other from being rasterized into a single DEM. Each island's DEM was visually inspected to verify that all large vegetation and buildings had been properly removed (Figure 34). If any artifacts were observed, the point cloud for that island was re-filtered by incrementally increasing or decreasing the step size. The DEM for that island was then regenerated, inspected, and the process repeated until a sufficient result was obtained (Figure 35). Refer to Chapter 3 for details on vertical accuracy of the lidar-derived DEMs.



**Figure 34.** Features such as building and vegetation exist in the left DEM where they have been removed in the right. This type of visual inspection took place over every DEM.

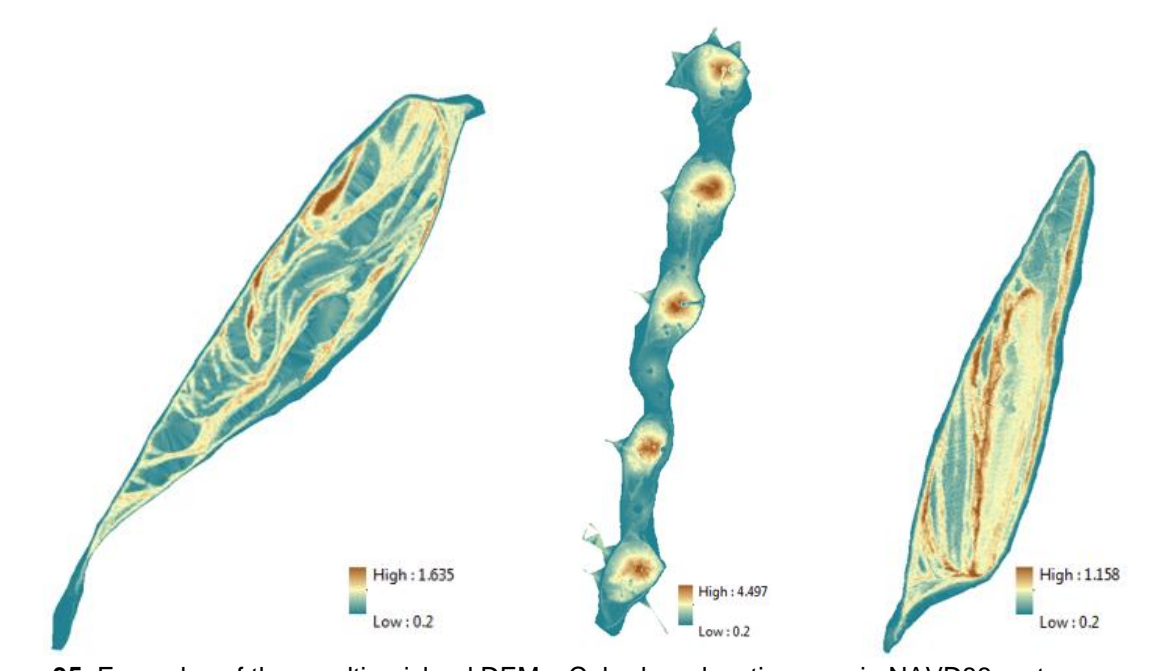


Figure 35. Examples of the resulting island DEMs. Color-bar elevations are in NAVD88 meters.

### 5.2.2 GIS-Layer of Island Morphometrics (Task 4)

### Creating the GIS Shapefile

The shapefile of the islands was created by contouring each island DEM at an elevation of 0.3 meters. An elevation of 0.3 meters served as an average mean sea level (MSL) among all islands in the upper Laguna Madre plus 10 cm error to account for lidar vertical uncertainty. This 0.3 meter shoreline contor elevation provides a baseline elevation for future monitoring efforts to assess island volumetrics from lidar surveys. Furthermore, this value helped ensure the removal of spurious lidar water surface returns. Below this 0.3 m elevation cutoff there were many points stemming from the water surface. Before the DEMs were contoured, a smoothing 5x5 low pass filter was used to smooth the DEMs. This smoothing step allowed for the contour lines to be continuous. Once the countour line was created it was manually traced 38

using an ArcGIS tracing tool to create the shapefile (Figure 36). The resulting shapefile consists of 172 islands. The island shapefile uses WGS84 UTM Zone 14N meters as a spatial reference system.

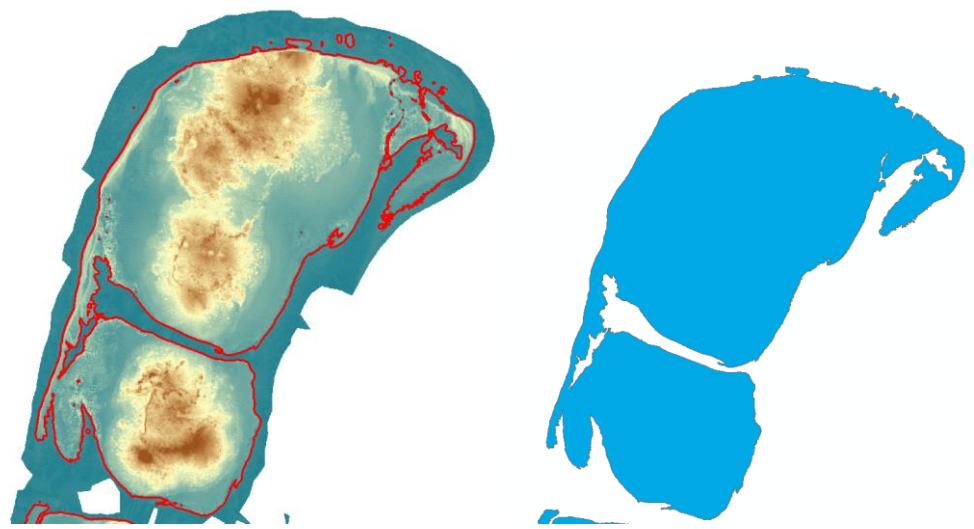


**Figure 36.** The image on the left shows the DEM with the 0.3 meter contour line drawn. The image on the right is the resulting shapefile after manually tracing the contour line.

### Calculating Island Morphometrics

With the DEM and shapefile of each island, it was possible to calculate morphometrics that describe the island characteristics. For each island the following statistics and morphometris were calculated: x centroid, y centroid, perimeter, area, volume, standard deviation of elevation, mean of elevation, range of elevation, maximum elevation, and pixel count. Zonal statistics within ArcMap was used to calculate all statistics and the Calculate Geometry tool was used to determine the perimeter, x centroid, and y centroid. The volume of each island was determined by calculating the height above the 0.3 m NAVD88 shoreline contour elevation for each pixel that was coincident with the shapefile. Because the DEM resolution was 1 m, volume per a cell was easily computed by taking the difference between the height of that cell and 0.3 m x 1 square meter. The volume of all pixels was then summed to derive the total island volume. Note that the volume above 0 m NAVD88, which is often used for volumetrics, can easily be computed from this GIS-layer by multiplying the island area times 0.3 m then adding that total to the volumetric total for the island.

### 5.2.3 Vulnerability Maps of Rookery Island Inundation to Sea Level Rise

#### Introduction

Created by Warren Pinnacle Consulting, the Sea Level Affecting Marshes Model (SLAMM) simulates the process of wetland conversions and shoreline modifications during long term sea level rise. SLAMM is utilized by a number of organizations including the National Oceanic and Atmospheric Administration (NOAA), the Environmental Protection Agency (EPA), the National Wildlife Federation (NWF) and many more. The model allows for the input of specific and unique data that describes the topology and sea level characteristics at a local level. For this reason we chose to use SLAMM for modeling a set of spoil islands in the Upper Laguna Madre and their vulnerability to long term sea level rise.

The model requires three raster inputs of the study site, 1) a digital elevation model (DEM), 2) a land type classification raster, and 3) a raster that describes the slope of the area. Also required are parameters that describe the local sea level such as the historic sea level rise trend (mm/yr), the mean sea level (MSL), and the great diurnal tide range (The difference in height between mean higher high water and mean lower low water).

#### DEM

Lidar-DEMs at 1 meter resolution were created from the January 29, 2015 UT BEG lidar survey data; the process for their creation is described above.

### Land Classification

The resulting DEMs were used to classify two land cover types, land and water. All pixels above the local MSL were classified to undeveloped dry land and the pixels equal to or below the MSL were classified as estuarine open water (Figure 37). The MSL was determined by the Texas Coastal Ocean Observation Network (TCOON) buoy reading relative to NAVD88 (vertical datum used for referencing of the LiDAR elevations). Because there is a slight downward trend in MSL from the northern end to the southern end of our study site, the site was broken up into three sections and each section utilized the MSL that was most appropriate. A map of the MSL values can be seen in Figure 38.

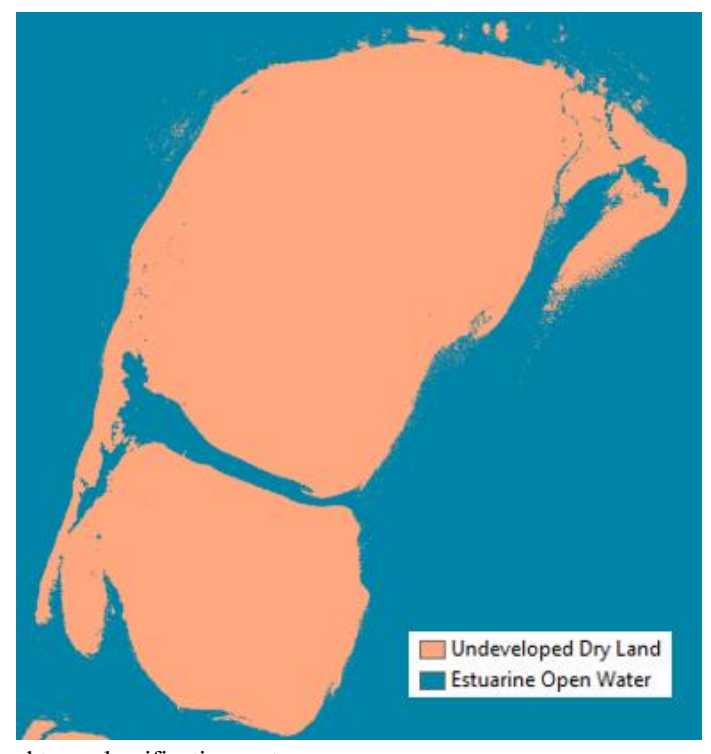


Figure 37. Example of land type classification raster.

#### (Data from lighthouse Database stations Datum pages accessed 1/3/2016)



Conrad Blucher Institute - 2016

**Figure 38.** NAVD88 referenced MSL, or Average Water Levels, along the southern Texas coast. The three sites used for this study were Packery Channel, South Bird Island, and Baffin Bay, north to south respectively. Source: Conrad Blucher Institute for Surveying and Science.

#### Slope

The slope of each island was determined by utilizing the Slope (Spatial Analysis) tool within ArcMap. Units are in degrees. An example of a resulting slope raster can be seen in Figure 39.

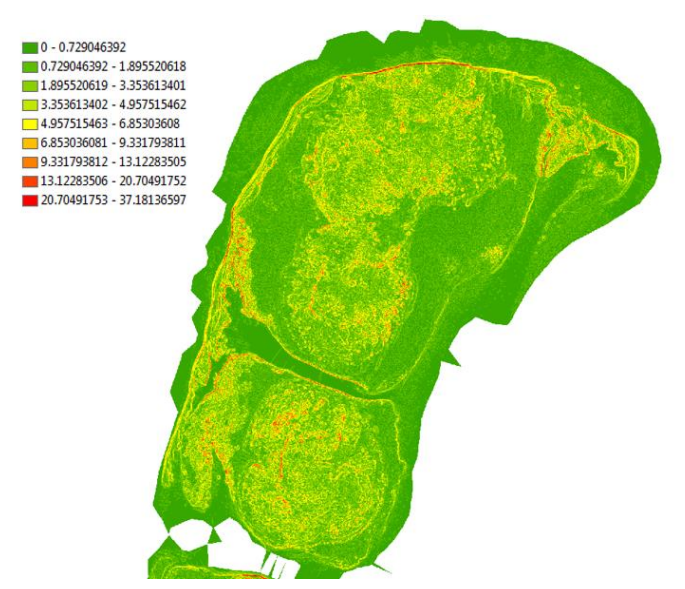


Figure 39. Slope raster of one of the spoil islands. Units are in degrees.

#### Sea Level Rise Historic Trend

The historic sea level rise trend was obtained from the NOAA Tides and Currents website using the nearest NOAA tidal gauge within the non-exposed bay system at Rockport TX (Gauge 8774770). Changes in MSL have been computed using a minimum span of 30 years of observations at each location. The measurements have been averaged by month to remove the effects of higher frequency phenomena in order to compute an accurate linear sea level trend. The MSL trends measured by tide gauges that are presented on the website are local relative MSL trends as opposed to the global seal level trends. Tide gauge measurements are made with respect to a local fixed reference level on land; therefore, if there is some long-term vertical land motion occurring at that location, the relative MSL trend measured there is a combination of the global eustatic sea level rate and the local vertical land motion. (http://tidesandcurrents.noaa.gov/sltrends/sltrends.html).

The mean sea level trend at the Rockport gauge is estimated to be 5.33 mm/year with a 95% confidence interval of +/- 0.47 mm/year based on monthly mean sea level data from 1937 to 2015 which is equivalent to a change of 1.75 feet in 100 years (Figure 40). The 5.33 mm/year trend was used for this study.

#### Mean Sea Level Trend 8774770 Rockport, Texas

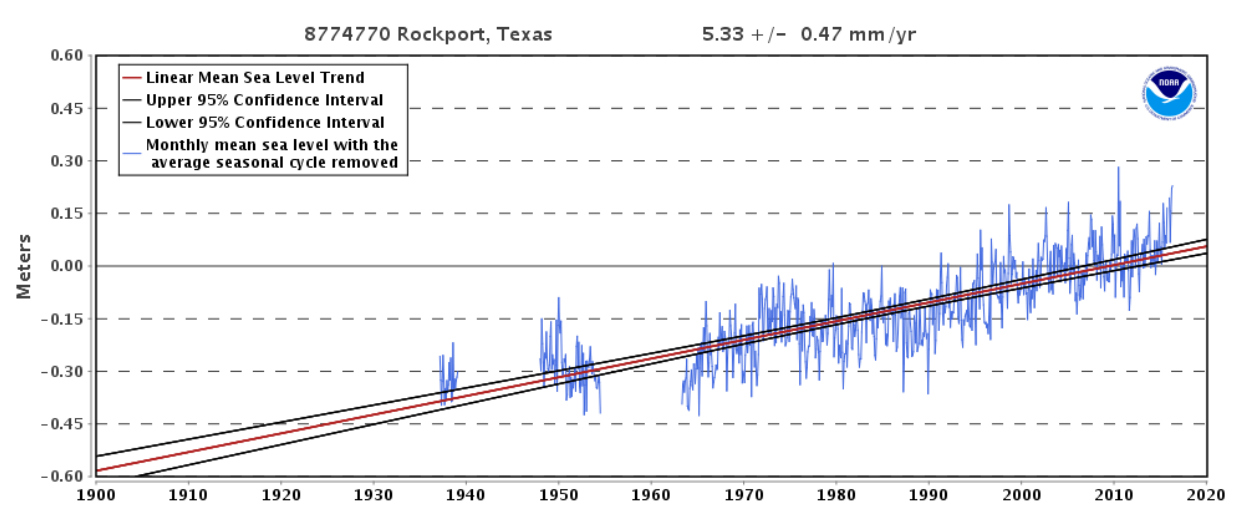


**Figure 40.** MSL linear trend estimated based on water level readings at the Rockport, TX tidal gauge. Source NOAA.

### Mean Sea Level to NAVD88 Offset

The MSL required for the model was taken from the same TCOONs water level readings that were used for the land classification (http://www.cbi.tamucc.edu/TCOON/). The three MSL values used for each of the three sections of the study site were 0.22 m (Packery Channel), 0.14 m (South Bird Island), and 0.1 m (Baffin Bay) from north to south respectively (Figure 38).

### Great Diurnal Tide Range

The great diurnal tide range is the difference in height between mean higher high water and mean lower low water. This value was taken from the Packery Channel observation buoy. Unfortunately the South Bird Island and Baffin Bay buoys that were used to obtain the MSL were not reporting the diurnal tide

range at the time of this work. Therefore, the Packery Channel value of 0.11 m was used for all three sections of the study site.

### Modeling Method

The parameters associated with each section of the study site were added to the model parameter list and the raster products for each section were added to the file setup page. The model was set up to create simulations starting from 2015 until 2100 at 25 year increments, therefore 5 maps were created for each section of the study site for a total 15 SLAMM maps. Each map was brought into ArcMap to create the final map product. Percent and areal change in exposed and submerged landcover were then computed based on the SLAMM model run and results reported. Furthermore, there comparison maps (one for each study section) show the difference in dry land area for 2015 and 2100.

#### 5.3 Results

#### 5.3.1 Results of Island Morphometrics

The GIS polygon layer of island shorelines (called here the Rookery Island shapefile) stores a variety of statistical attributes that help to describe and quantify characteristics associated with the individual islands. Table 12 below summarizes the statistical results of island morphometrics based on the lidar-derived DEMs. These results show the minimum and maximum values observed within the Upper Laguna Madre study region along with the value's associated island name. The naming convention is based on the naming convention utilized by the UT BEG in their lidar survey data.

**Table 12.** Statistical results of island morphometrics derived from the lidar-DEMs.

	Island Name	Value
Max Volume	Causeway Islands A	564,204 m³
Min Volume	Marker 72 Spoil Island NM 152 D	9.412 m³
<b>Highest Max Elevation</b>	West of North Bird Island K	5.605 m
<b>Lowest Max Elevation</b>	Marker 72 Spoil Island NM 152 D	0.379 m
<b>Highest Min Elevation</b>	Marker 77A Spoil Island NM 155	0.288 m
<b>Lowest Min Eleavtion</b>	Marker 103117 Spoil NM 207221 A	0.2 m
Max Mean Elevation	West of North Bird Island K	1.609 m
Min Mean Elevation	Marker 72 Spoil Island NM 152 D	0.325 m
<b>Max STD Elevation</b>	West of North Bird Island K	1.119 m
Min STD Elevation	Kennedy Causeway Islands1 G	0.026 m
<b>Max Elevation Range</b>	West of North Bird Island K	5.377 m
Min Elevation Range	Marker 72 Spoil Island NM 152 D	0.107 m
Max Area	Causeway Islands A	563,423 m²
Min Area	Marker 72 Spoil Island NM 152 D	29 m²
Max Perimeter	Causeway Islands A	7364.608 m
Min Perimeter	Marker 72 Spoil Island NM 152 D	23.83421 m

### 5.3.2 Results of the SLAMM Modeling

Appendix C shows results of the SLAMM runs for each study section in 25 year increments from 2015 to 2100; and three comparison maps of landcover change between 2015 and 2100 (one per study region: north, mid, south). SLAMM utilizes 23 different land cover categories to describe the initial land type under analysis as well as the transitioning land as the sea level rises. Each SLAMM map displays a table that describes the land cover change that occurs between the start date (2015) and the projected date. Table 13 below shows results from the 2015 to 2100 SLAMM landcover change comparison map (north section). The dry land loss column shows the amount of dry land that was lost to each land type. Similarly, the dry land percent loss column shows the percentage of dry land that was lost to each land type. A portion of what was dry land in 2015 is projected to be converted into 4 different land types; transitional marsh/scrub shrub, regularly flooded marsh, tidal flat, and estuarine open water. However, the main focus here should be on the difference in exposed and dry land cover (i.e. estimated inundation and land loss due to SLR); not necessarily the type of transitional landcover. Because these are spoil islands, they likely do not modulate the same as a natural marsh system assumed by SLAMM.

Table 13. Results from the 2015 to 2100 SLAMM landcover change comparison map (north section).

*Values From 2015 to 2100	Dry Land Loss	Dry Land Percent Loss
Transitional Marsh/Scrub Shrub	238,722 m <sup>2</sup>	14.18%
Regularly Flooded Marsh	461,470 m <sup>2</sup>	27.41%
Tidal Flat	546,693 m <sup>2</sup>	32.47%
Estuarine Open Water	10,613 m <sup>2</sup>	0.63%

Because these tables show the land cover change over time, the initial 2015 maps will not display a table. It should be noted that the 2015 to 2025 maps for both the mid and south section show negligble land cover change. As the model starts to accelerate sea level rise based on the input rate, these sections do start showing landcover transition in later years out to 2100.

### 5.4 Conclusion

The SLAMM model is capable of taking into consideration a large number of different parameters such as wind and wave driven shoreline erosion, beach sedimentation rate, sediment transport flux, vegetation accretion, and other factors. For this study, we created a generalized model of how the rising sea level can affect the spoil islands of the Upper Laguna Madre assuming standard beach landcover. These results do not account for historic shoreline erosion trends on the islands, episodic events, anthropogenic factors, or local sea level rise rates adjusted for scenarios based on worst case global projections of SLR over the coming century. Furthermore, the rate of relative sea level rise likely varies somewhat across the study region relative to the rate reported in Rockport due to land subsidence variability from compaction and other factors. The models created for this study, however, do simulate the impacts from a rising sea in regards to real world inputs such as high-resolution topography, slope, local mean sea level, tidal range, and regional historic trend in sea level rise. As such, these SLAMM maps provide a projection of potential land loss beyond what is capable with a standard bathtub model of sea level inundation. Simulated land loss from these results provides resource managers a quantitative assessment for the purpose of

identifying vulnerable rookery island habitat for water bird species. It is important to mention that the results here may underestimate potential land loss due to the non-coupling of shoreline erosion trends and episodic events. More analysis and simulation should be done at specific islands of interest where vulnerabilities are identified and mitigation efforts planned based on this assessment.

### 6. Conclusion

The first component of this project supported an airborne bathymetric lidar and digital imaging survey (conducted in January 2015) of a region within Shamrock Cove (~20 square kilometers) located in Corpus Christi Bay. The purpose of this survey was to investigate the potential of bathymetric lidar and aerial imagery in fusion to map submerged structures. Deliverables from this component included: (1) topobathymetric lidar survey, (2) lidar-derived DEM of topography and bathymetry, (3) GIS-layer delineating submerged structures utilizing the bathymetric lidar and aerial imagery. As discussed in Chapter 4, several methods were implemented and investigated to improve submerged structure delineation including glint removal and edge detection. The data products support a TGLO initiative to map and remove derelict structures (e.g. abandoned pipelines) in the region that pose a hazard to recreation and navigation.

The second component of this project utilized airborne lidar measurements (collected in January 2015) of island topography within the Upper Laguna Madre to characterize rookery island habitat vulnerability. The analysis targeted the chain of spoil islands near the JFK causeway and along the Intracoastal Waterway from Corpus Christi Bay south to the land bridge below Baffin Bay (~100 sq. km). The following deliverables were created: (1) high-resolution DEMs and DSMs of island terrain with accuracy assessment; (2) GIS-layer to describe island morphometrics; (3) inundation maps of island vulnerability to sea level rise. All data products are available and accessible via online sources as outlined in Appendix D. The project outputs can be applied by resource managers to monitor island evolution, identify vulnerable habitat or alternative habitat, derive new understanding about nesting and landscape interaction, and assess coastal hazards impacts.

### 7. Acknowledgements

The methods, results, and discussion presented here represent the combined efforts of PI Starek and a team of student researchers at Texas A&M University-Corpus Christi (TAMUCC). The following lists the student researchers and their contributions to the project by tasks:

Carly Erwin, Geographic Information Science undergraduate student: Michael Schwind, Geospatial Surveying Engineering master student: Behrohk Nazeri, Geospatial Surveying Engineering Masters student: Jason Louis, GIS Analyst at the Conrad Blucher Institute: Task 4, 6 (GIS)
Task 1,3,4,5 (Rookery Islands)
Task 1,2 (Submerged pipelines)

Task 6 (website development)

Without the combined effort of the team above, the results and success of the project would not have been possible.

Finally, the research team wishes to express their sincere gratitude and appreciation to NOAA and the TGLO Coastal Management Project for supporting this project. Support from this project provided the student participants exceptional research and learning opportunities. The project resulted in three peer-reviewed professional conference presentations by students, and the research on submerged pipeline delineation supported in part the completion of a Master student thesis in Geospatial Surveying Engineering at TAMUCC. Refer to Appendix E for details on presentations and thesis.

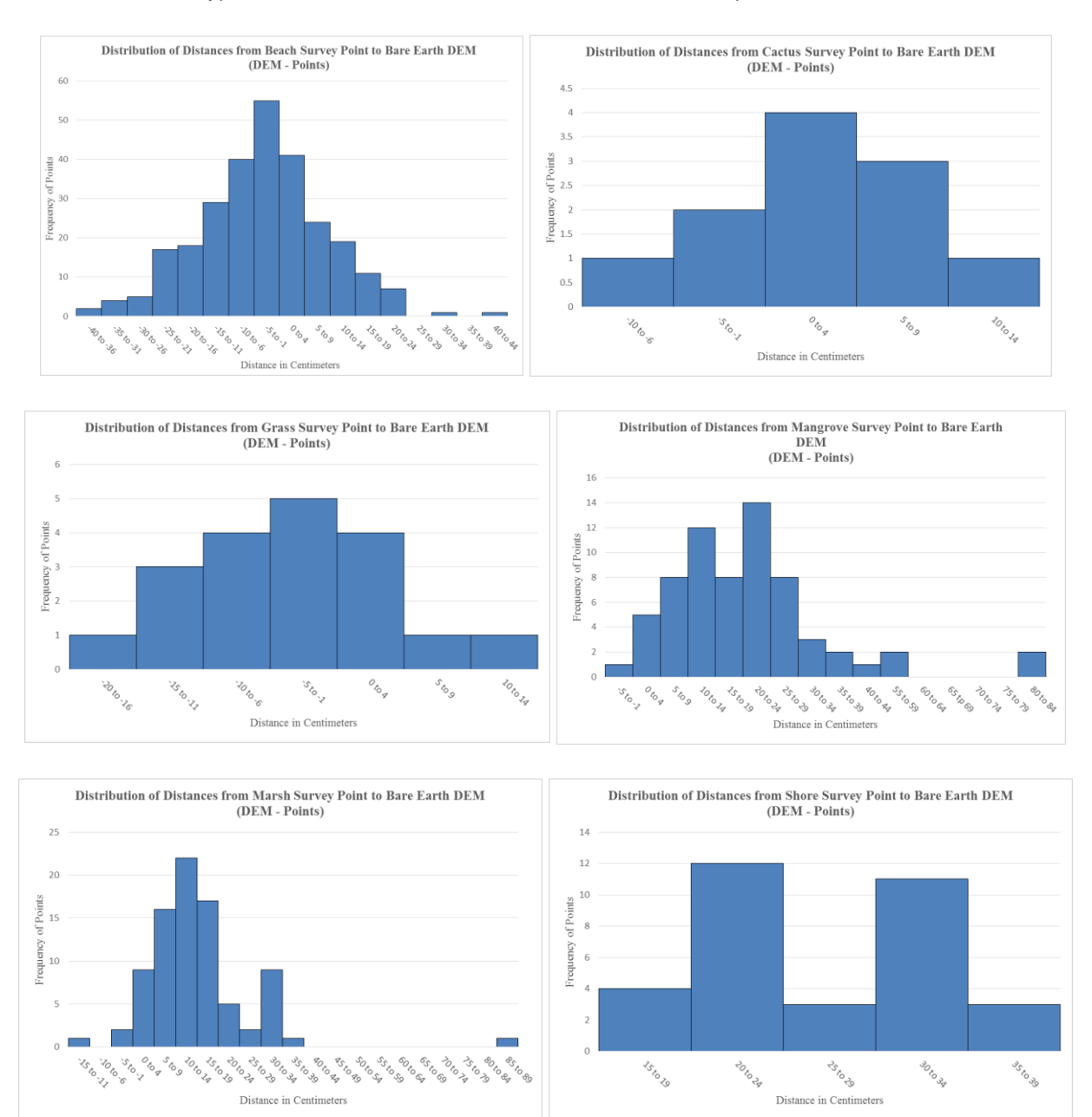
#### 8. References

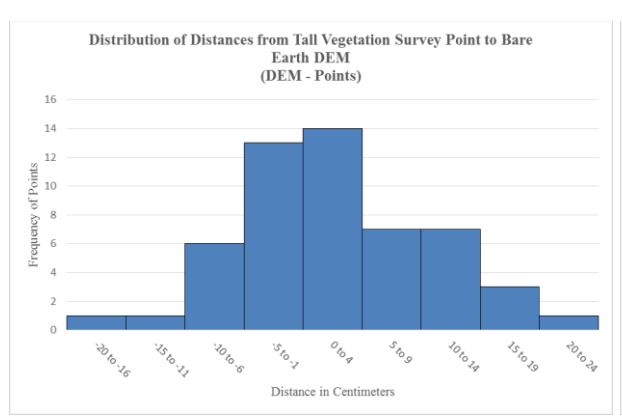
- [1] A. Wehr and U. Lohr, "Airborne laser scanning—An introduction and overview," J. Photogrammetry & Remote Sensing, vol. 54, pp. 68–82, 1999.
- [2] E.P. Baltsavias, "Airborne laser scanning: basic relations and formulas," ISPRS Journal of Photogrammetry and Remote Sensing, vol. 54, pp. 199-214, 1999.
- [3] R.L. Shrestha, W.E. Carter, M. Sartori, B.J. Luzum, K.C. Slatton, "Airborne laser swath mapping: quantifying changes in sandy beaches over time scales of weeks to years," ISPRS Journal of Photogrammetry and Remote Sensing, vol. 59, no. 4, pp. 222-232, 2005.
- [4] M.J. Starek, R.J. Vemula, K.C. Slatton, and R.L. Shrestha, Probabilistic Detection of Morphologic Indicators for Beach Segmentation with Lidar Time Series, IEEE Transactions on Geoscience and Remote Sensing, 50 (11), 2012.
- [5] K.C. Slatton, W.E. Carter, R.L. Shrestha, and W. Dietrich, "Airborne laser swath mapping: achieving the resolution and accuracy required for geosurficial research," Geophysical Research Letters, Vol. 34, 2007.
- [6] S. Peeri, J. V. Gardner, L. G. Ward, and J. R. Morrison, "The Seafloor: A Key Factor in Lidar Bottom Detection," IEEE Trans. Geosci. Remote Sens., vol. 49, issue 3, pp. 1150-1157, 2011.
- [7] A.H. Sallenger et al., "Evaluation of airborne topographic lidar for quantifying beach changes," Journal of Coastal Research, vol. 19,no. 1, pp. 125-133, 2003.
- [8] S.A. White and Y. Wang, "Utilizing DEMs derived from LIDAR data to analyze morphologic change in the North Carolina coastline," Remote Sensing of the Environment, vol. 85, 2003.
- [9] K. Zhang, D. Whitman, S. Leatherman, and W. Robertson, "Quantification of beach changes caused by Hurricane Floyd along Florida's Atlantic coast using airborne laser surveys," Journal of Coastal Research, vol. 21, no. 1, pp. 122–134, 2004.
- [10] M.J. Starek, K.C. Slatton, R.L. Shrestha, and W.E. Carter, W.E., "Airborne lidar measurements to quantify change in sandy beaches," in Laser Scanning for the Environmental Sciences, Oxford: Wiley Blackwell Publishing, 2009, pp. 147-164.
- [11] H. Mitasova, M. Overton, J.J. Recalde, D. Bernstein, and C. Freeman, "Raster-based analysis of coastal terrain dynamics from multitemporal lidar data," Journal of Coastal Research, vol. 25, no. 2, pp. 507-514, 2009.
- [12] Sithole, George, and George Vosselman. "Experimental comparison of filter algorithms for bare-Earth extraction from airborne laser scanning point clouds." ISPRS journal of photogrammetry and remote sensing 59.1 (2004): 85-101.
- [13] Cichocinski, Piotr, and Izabela Basista. "The Comparison of Spatial Interpolation Methods in Application to the Construction of Digital Terrain Models." International Multidisciplinary Scientific GeoConference: SGEM: Surveying Geology & mining Ecology Management 1 (2013): 959.
- [14] Hedley, J. D., A. R. Harborne, and P. J. Mumby. "Technical note: Simple and robust removal of sun glint for mapping shallow-water benthos." *International Journal of Remote Sensing* 26.10 (2005).
- [15] Lyzenga, David R., Norman P. Malinas, and Fred J. Tanis. "Multispectral bathymetry using a simple physically based algorithm." *IEEE Transactions on Geoscience and Remote Sensing* 44 (8), 2006.
- [16] Kay, Susan, John D. Hedley, and Samantha Lavender. "Sun glint correction of high and low spatial resolution images of aquatic scenes: A review of methods for visible and near-infrared wavelengths." Remote Sensing 1.4 (2009): 697-730.
- [17] Kang, Chung-Chia, and Wen-June Wang. "A novel edge detection method based on the maximizing objective function." Pattern Recognition 40.2 (2007): 609-618.

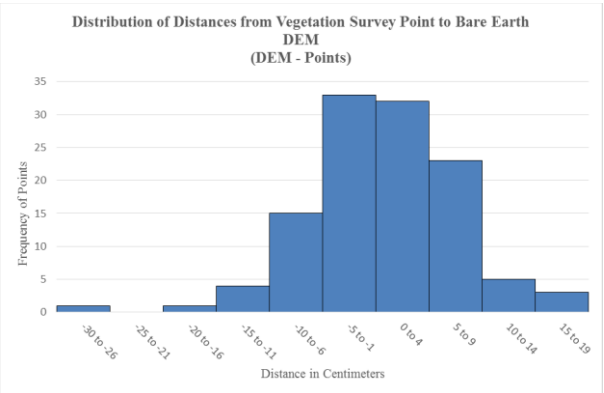
- [18] Seif, Aramesh, Mohammad Mohammadpour Salut, and Muhammad Nadzir Marsono. "A hardware architecture of Prewitt edge detection." Sustainable Utilization and Development in Engineering and Technology Conference, IEEE, 2010.
- [19] Heath, Michael D., et al. "A robust visual method for assessing the relative performance of edge-detection algorithms." *IEEE Transactions on Pattern Analysis and Machine Intelligence* 19.12 (1997): 1338-1359.
- [20] P. Axelsson, "DEM generation from laser scanner data using adaptive TIN models," International Archives of Photogrammetry and Remote Sensing, vol. 33, 2000.

# Appendix A. RTK GPS vs. LiDAR Statistics

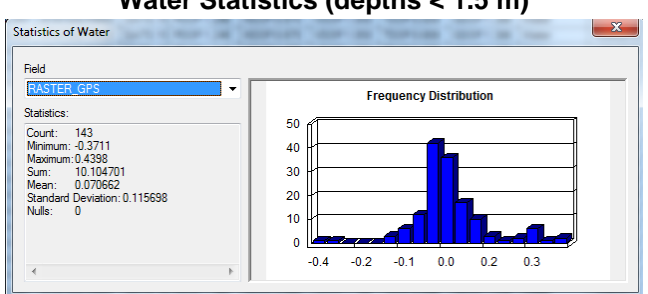
Figures below show histograms for elevation differences measured between LiDAR and RTK GPS for different landcover types on Sharock Island as shown in Table 1 of Chapter 3.







## Water Statistics (depths < 1.5 m)



Appendix B. Results from Bathymetric DEM Interpolation at Shamrock Cove

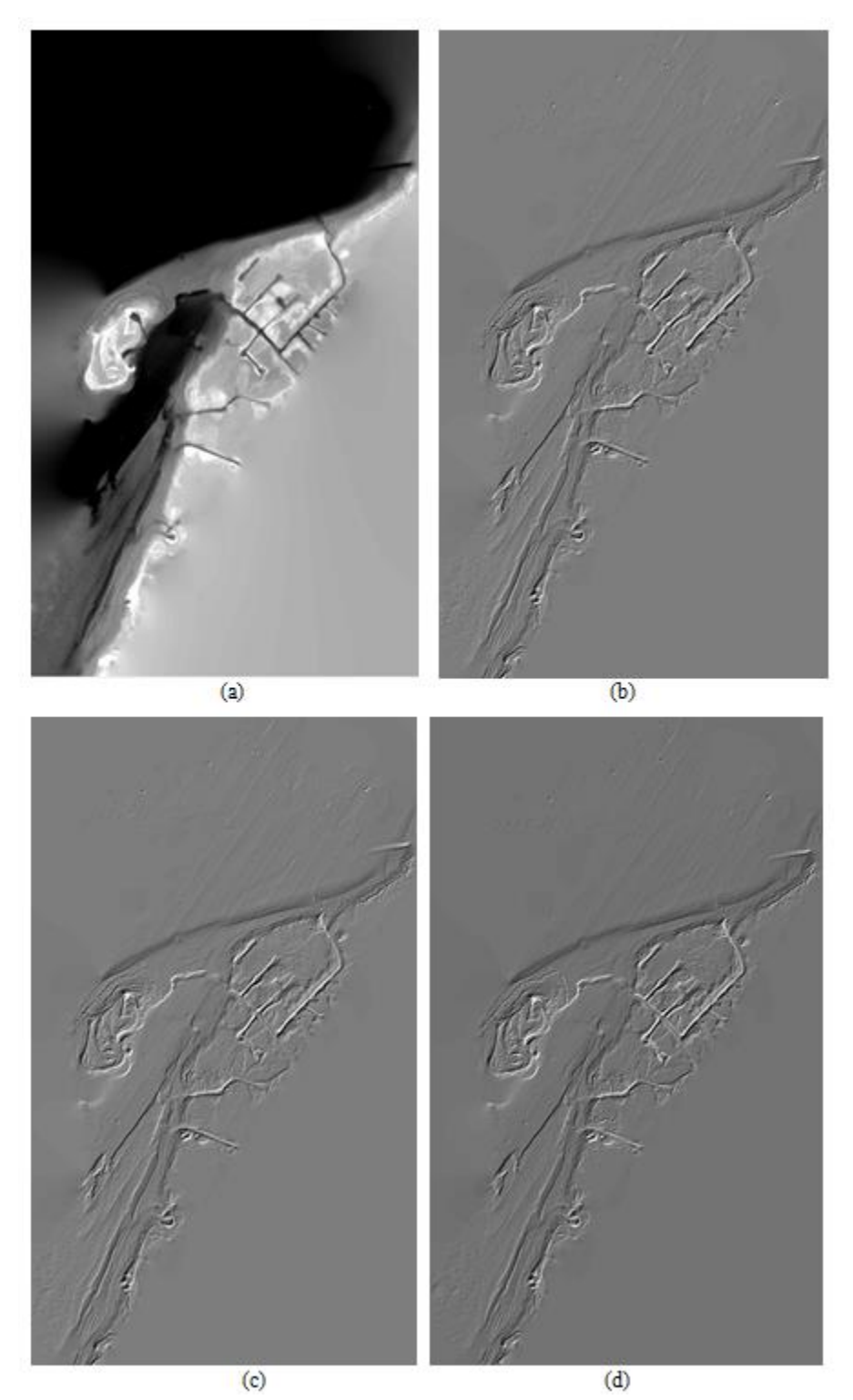


**Figure B1**. B-spline interpolation cell size=2 a) DEM b) Shaded relief h= 30 c) Shaded relief h= 45 d) Shaded relief h= 60

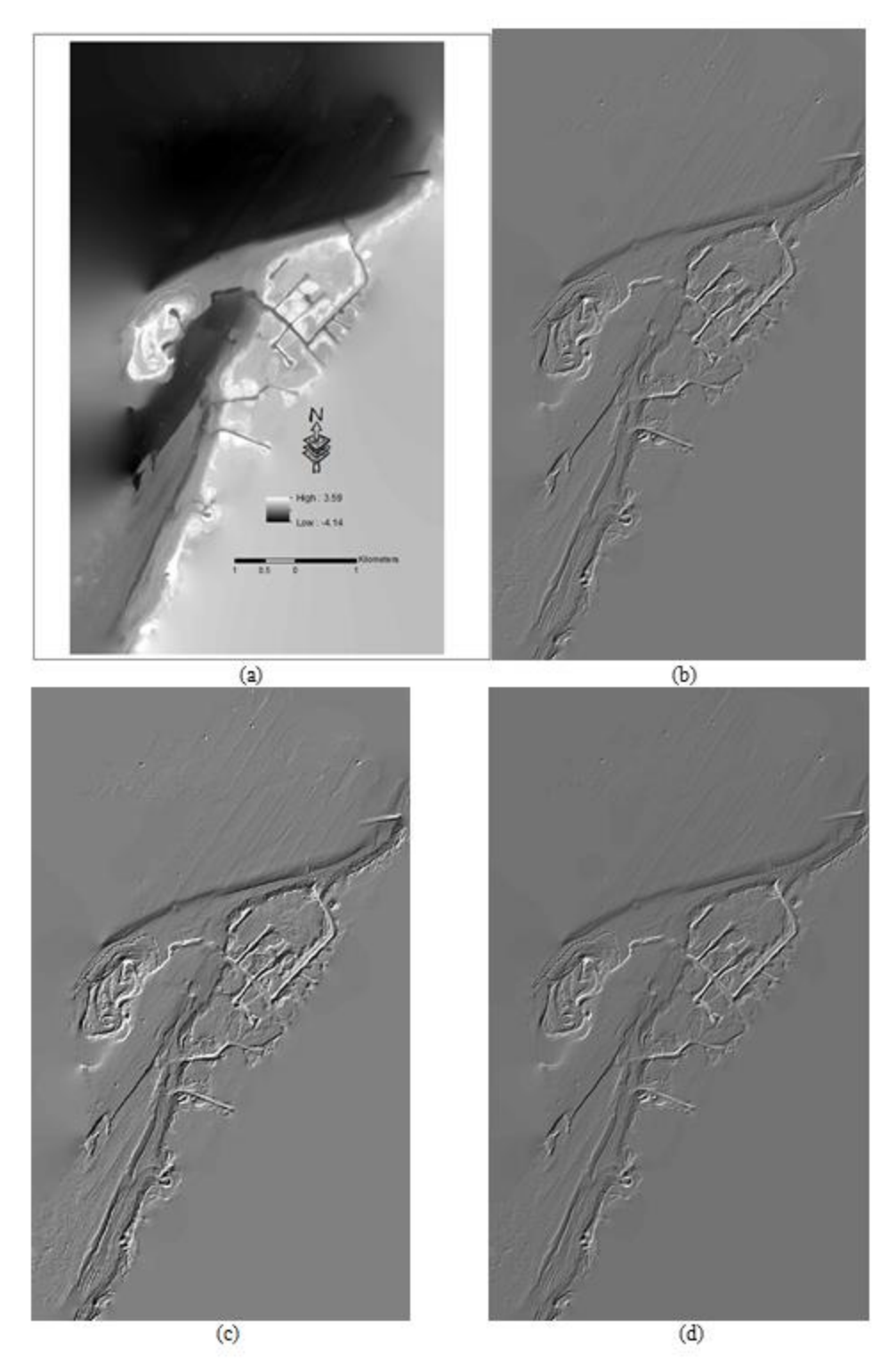


**Figure B2.** B-spline cell size=1 a) DEM b) Shaded relief h=30 c) Shaded relief h=45 d) Shaded relief h=60

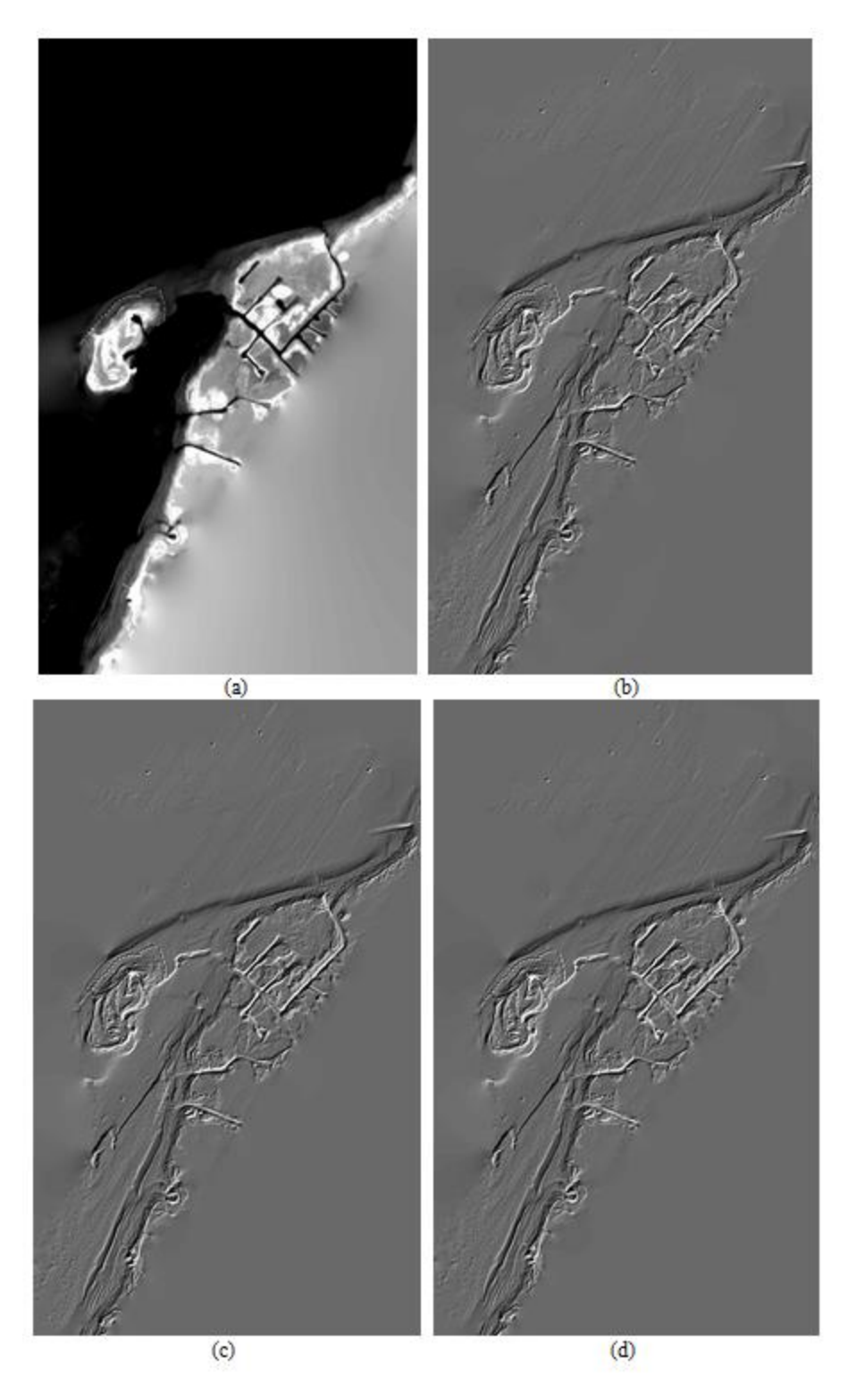


**Figure B3.** B-spline cell size 0.50 a) DEM b) Shaded relief h=30 c) shaded relief h=45 d) shaded relief h=60

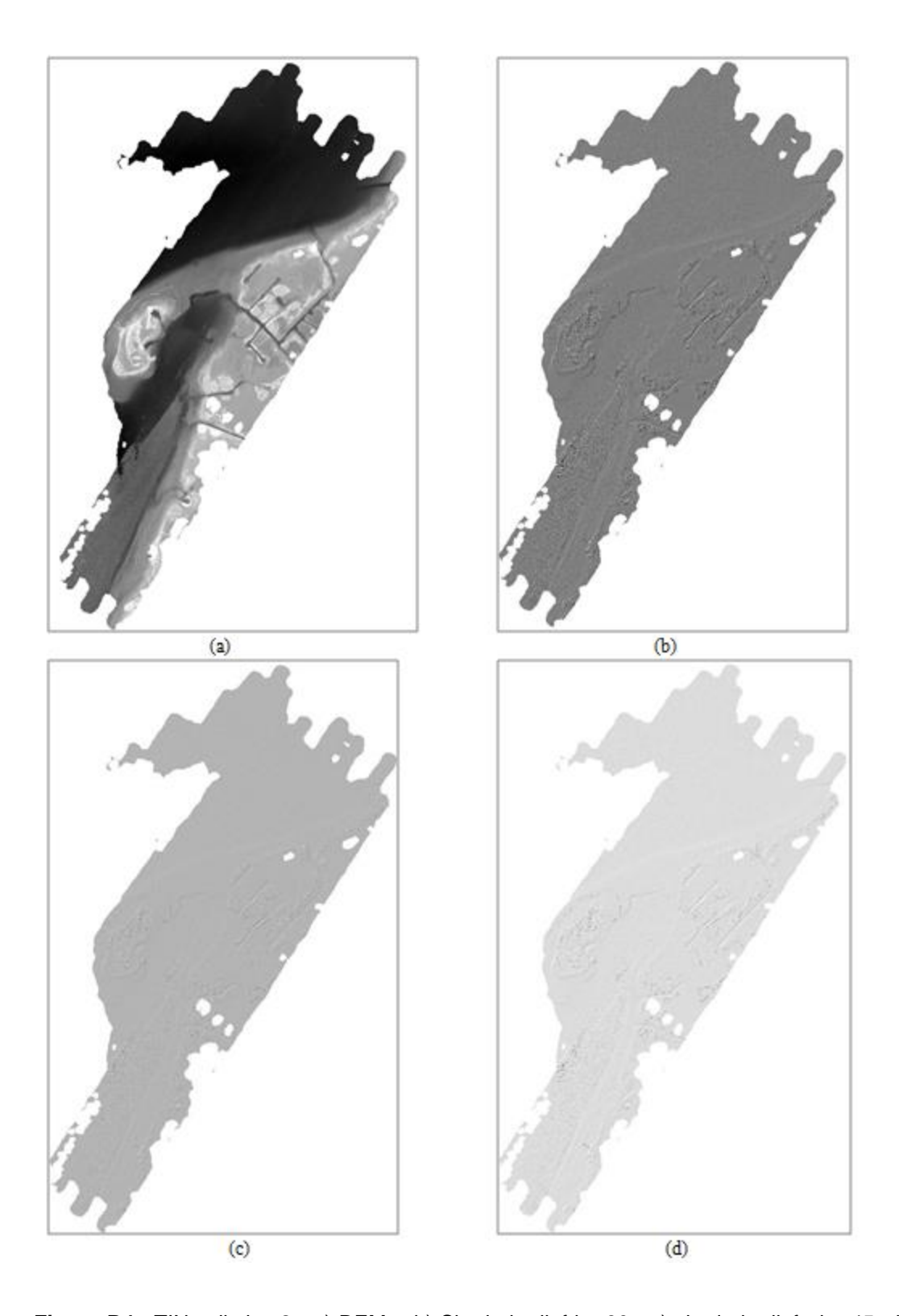


**Figure B4.** TIN cell size 2 a) DEM b) Shaded relief h=30 c) shaded relief h=45 d) shaded relief h=60

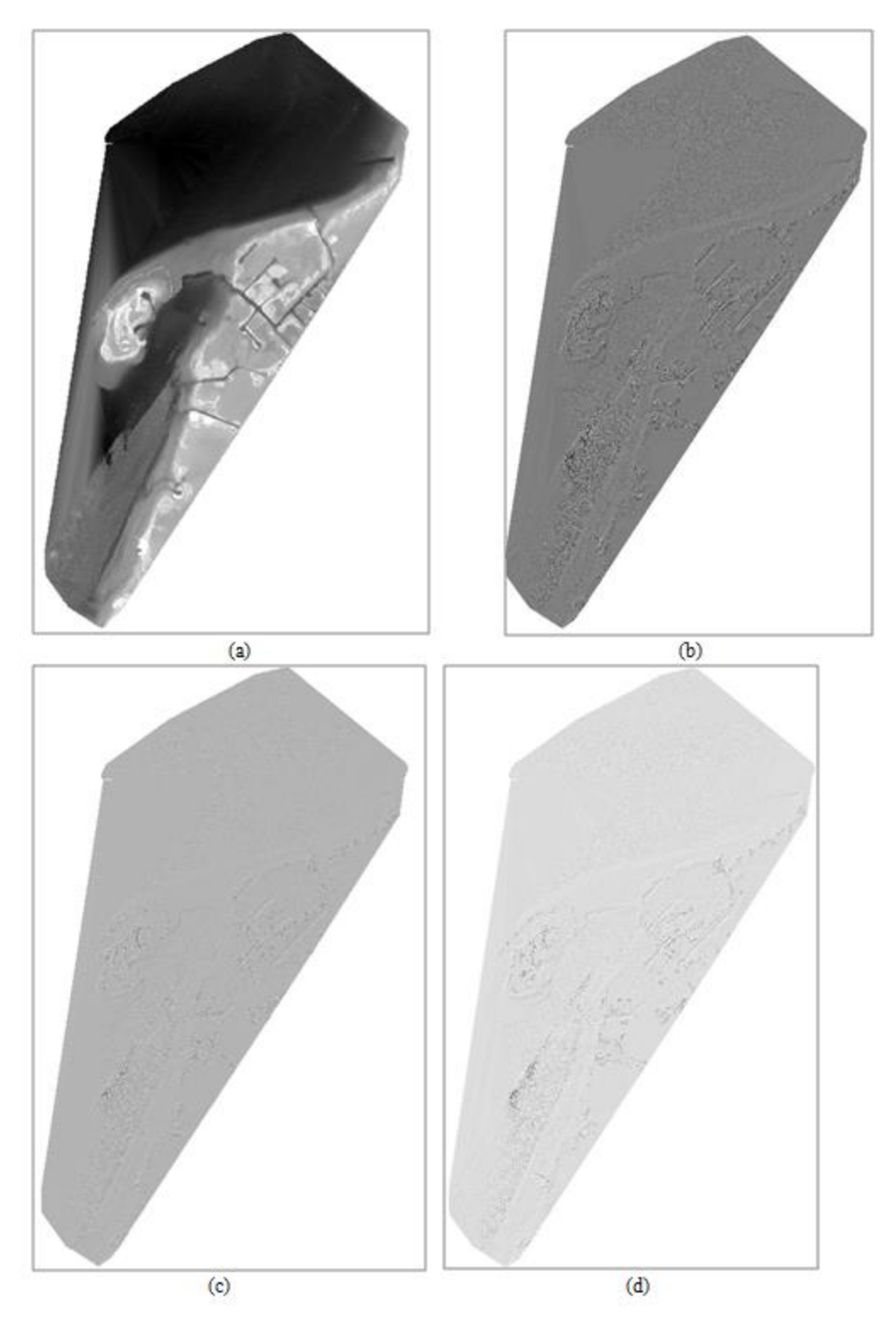
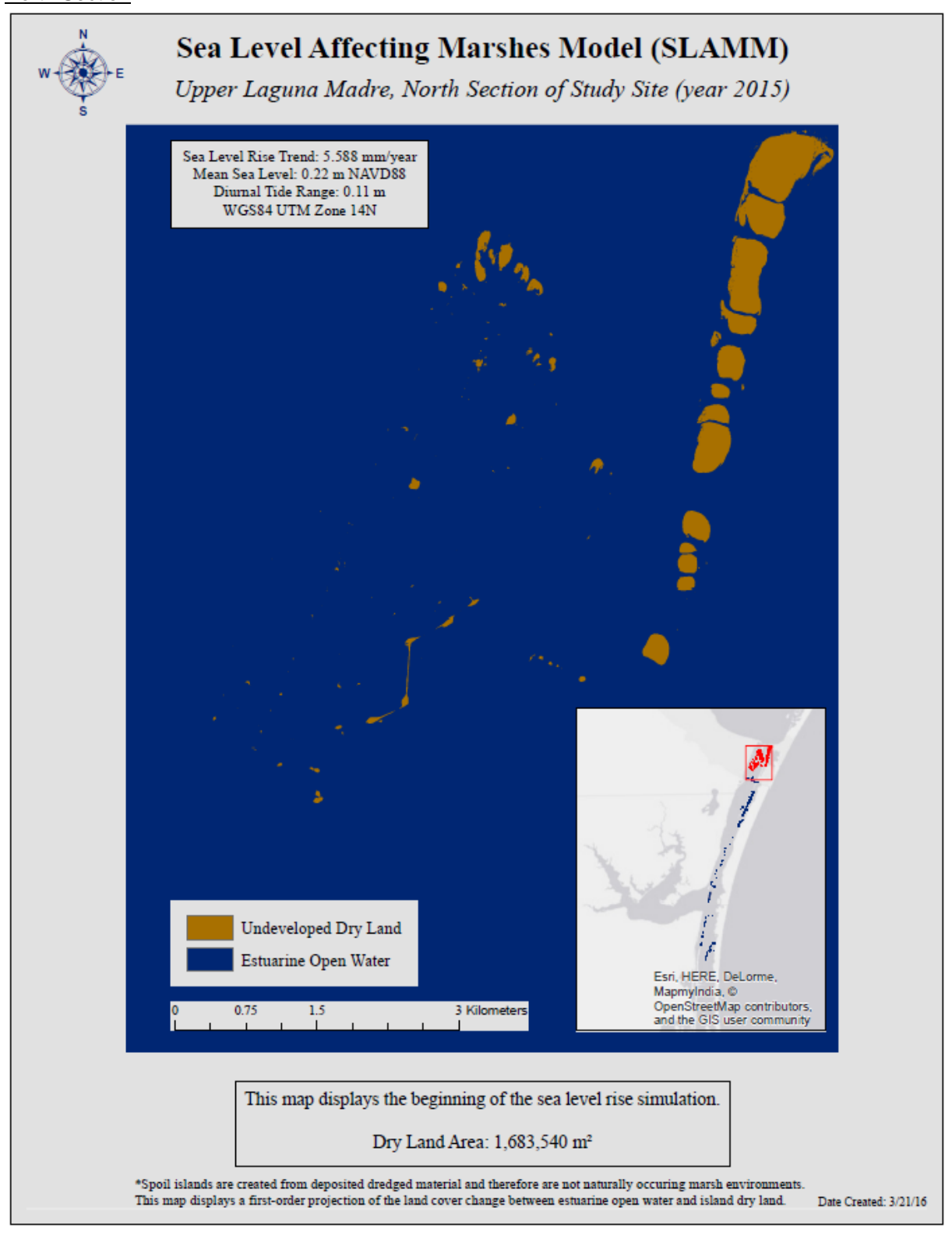


**Figure 5.5.** IDW cell size 2 a) DEM b) Shaded relief h= 30 c) shaded relief h= 45 d) shaded relief h= 60.

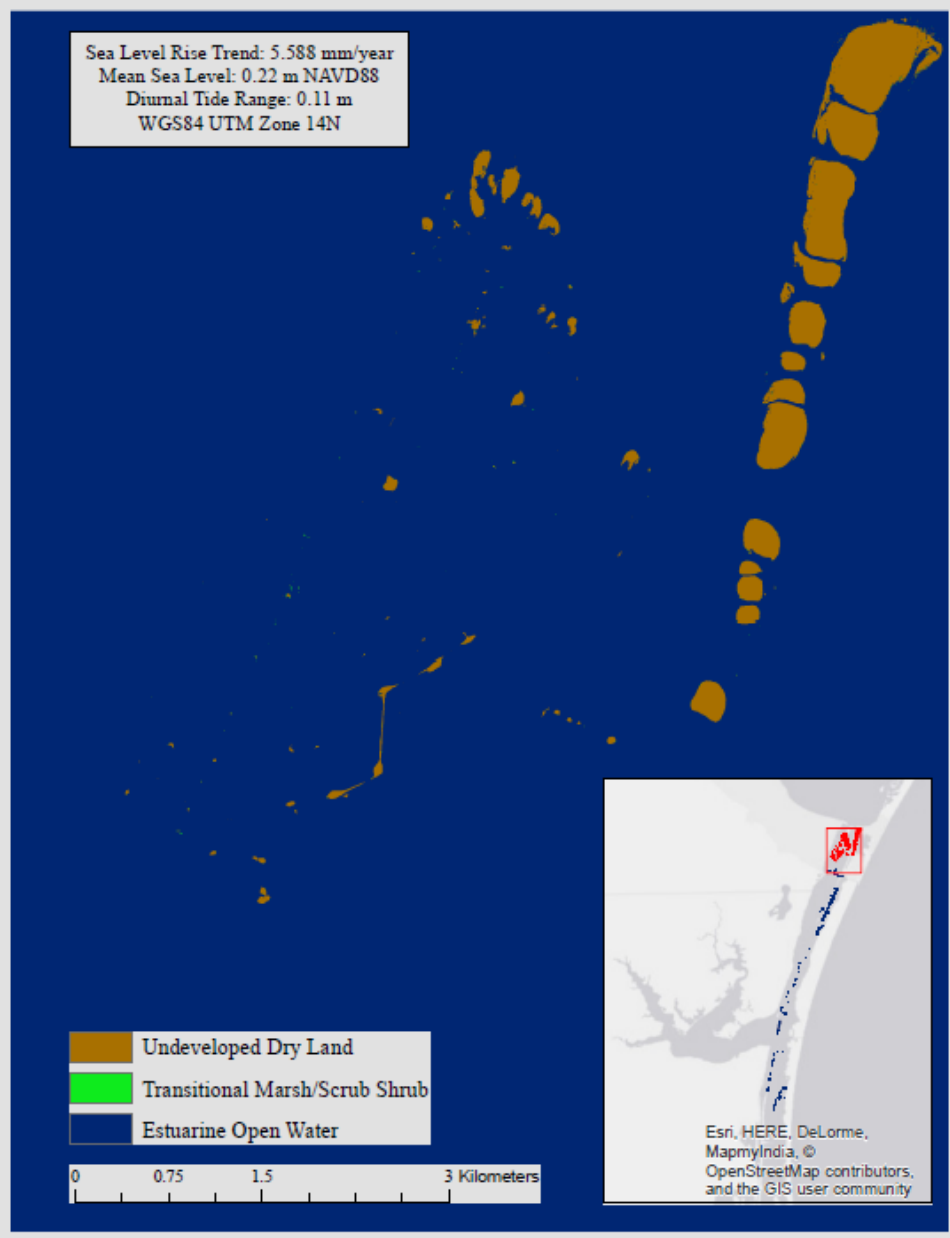
## Appendix C. SLAMM SLR Inundation Models of the Upper Laguna Madre

### North Section





Upper Laguna Madre, North Section of Study Site (year 2025)

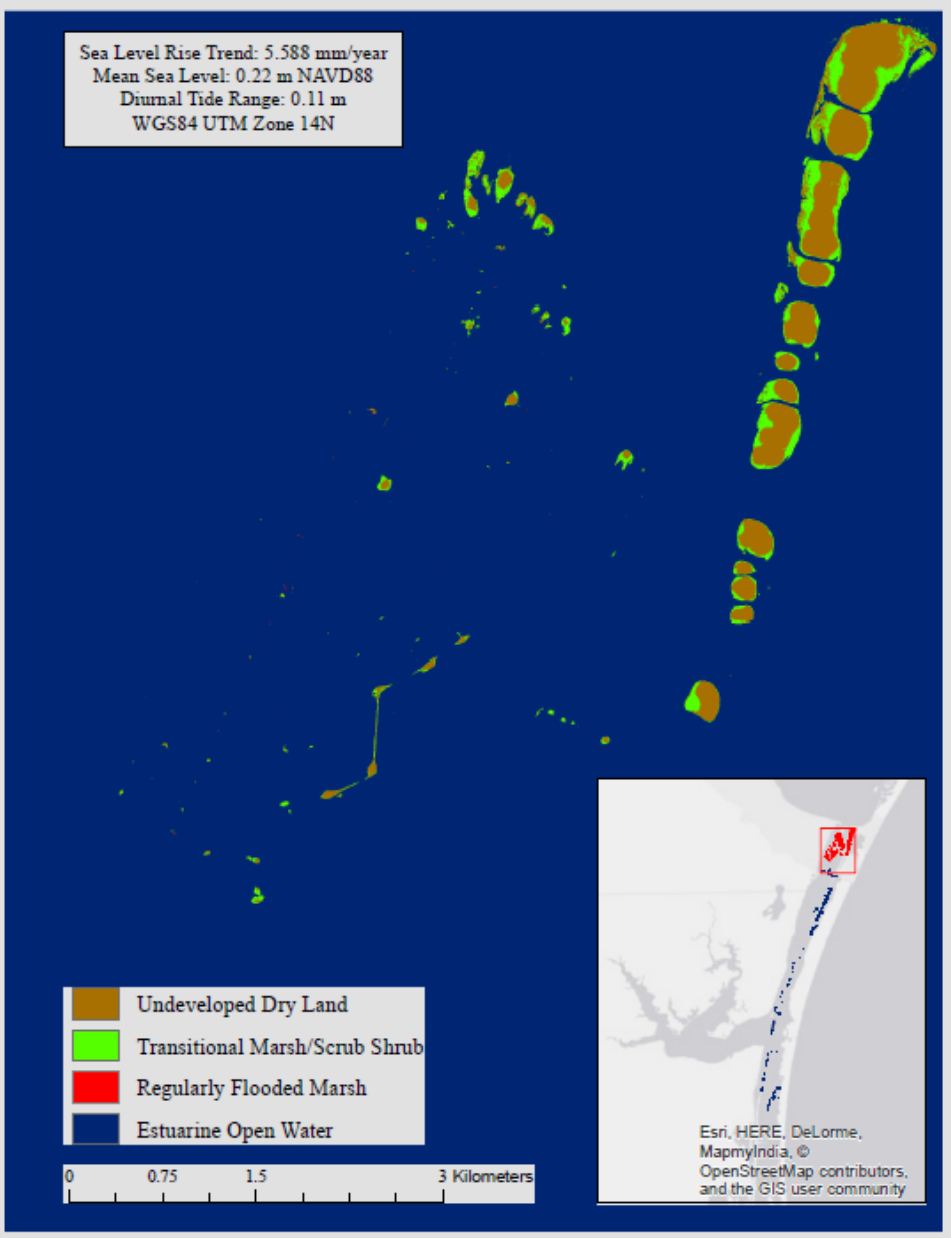


*Values From 2015 to 2025	Dry Land Loss	Dry Land Percent Loss
Transitional Marsh/Scrub Shrub	10,556 m²	0.63%
Estuarine Open Water	0 m²	0.00%

<sup>\*</sup>Spoil islands are created from deposited dredged material and therefore are not naturally occuring marsh environments. This map displays a first-order projection of the land cover change between estuarine open water and island dry land.



Upper Laguna Madre, North Section of Study Site (year 2050)

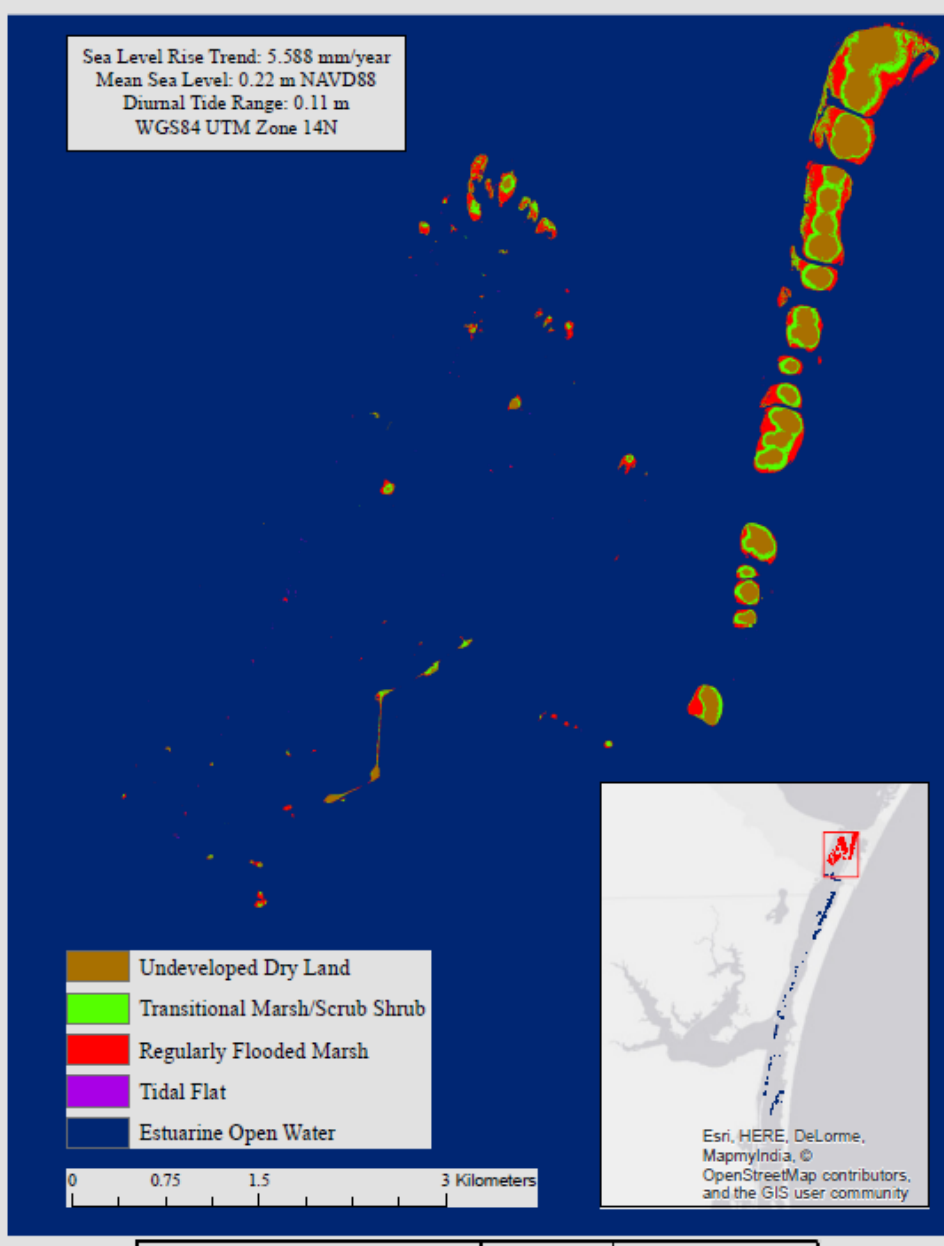


*Values From 2015 to 2050	Dry Land Loss	Dry Land Percent Loss
Transitional Marsh/Scrub Shrub	546750 m²	32.48%
Regularly Flooded Marsh	10556 m²	0.63%
Estuarine Open Water	0 m²	0.00%

<sup>\*</sup>Spoil islands are created from deposited dredged material and therefore are not naturally occuring marsh environments. This map displays a first-order projection of the land cover change between estuarine open water and island dry land.



Upper Laguna Madre, North Section of Study Site (year 2075)

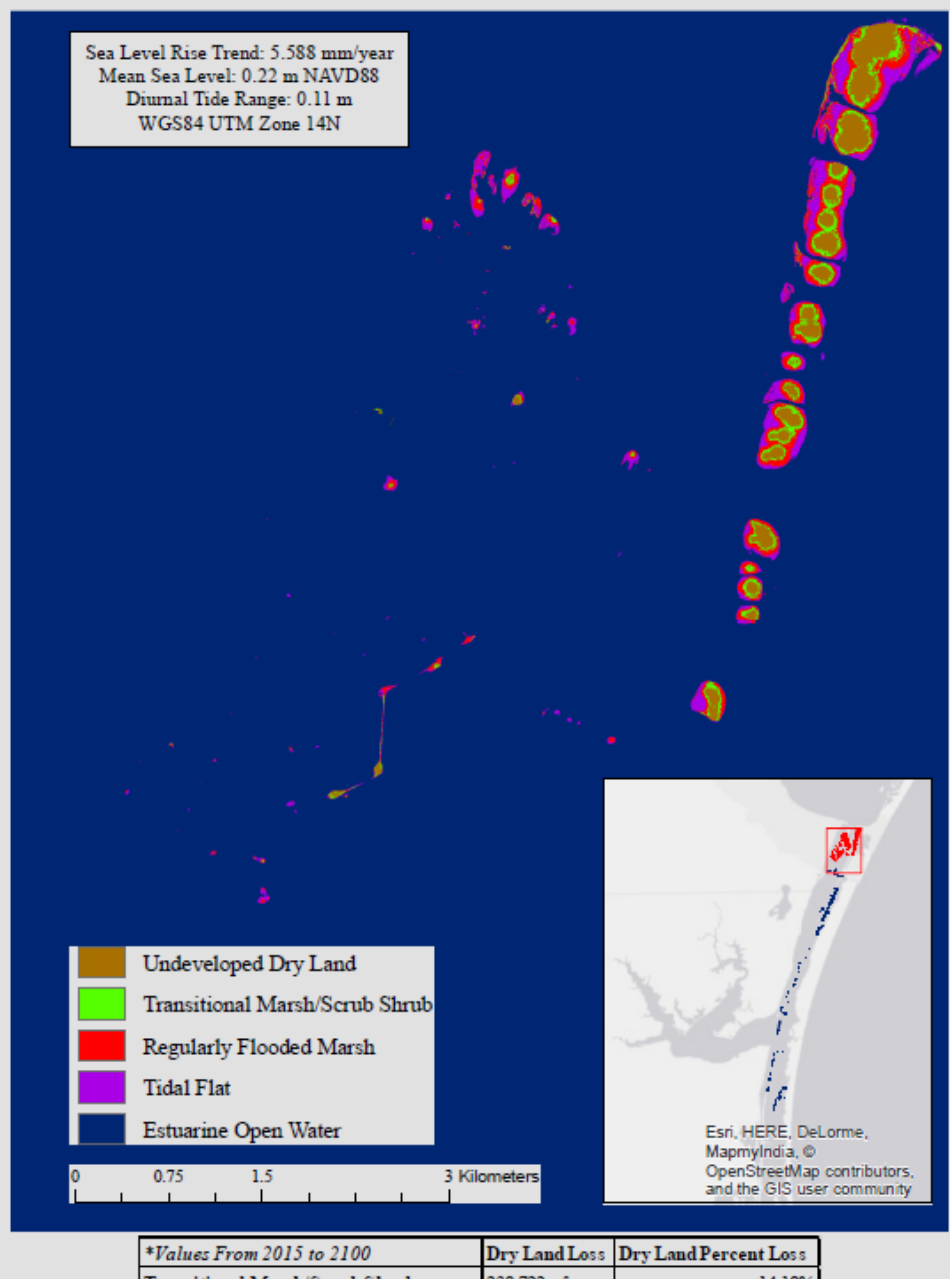


*Values From 2015 to 2075	Dry Land Loss	Dry Land Percent Loss
Transitional Marsh/Scrub Shrub	461,470 m²	27.41%
Regularly Flooded Marsh	546,750 m²	32.48%
Tidal Flat	10,556 nf	0.63%
Estuarine Open Water	0 m²	0.00%

<sup>\*</sup>Spoil islands are created from deposited dredged material and therefore are not naturally occuring marsh environments. This map displays a first-order projection of the land cover change between estuarine open water and island dry land.

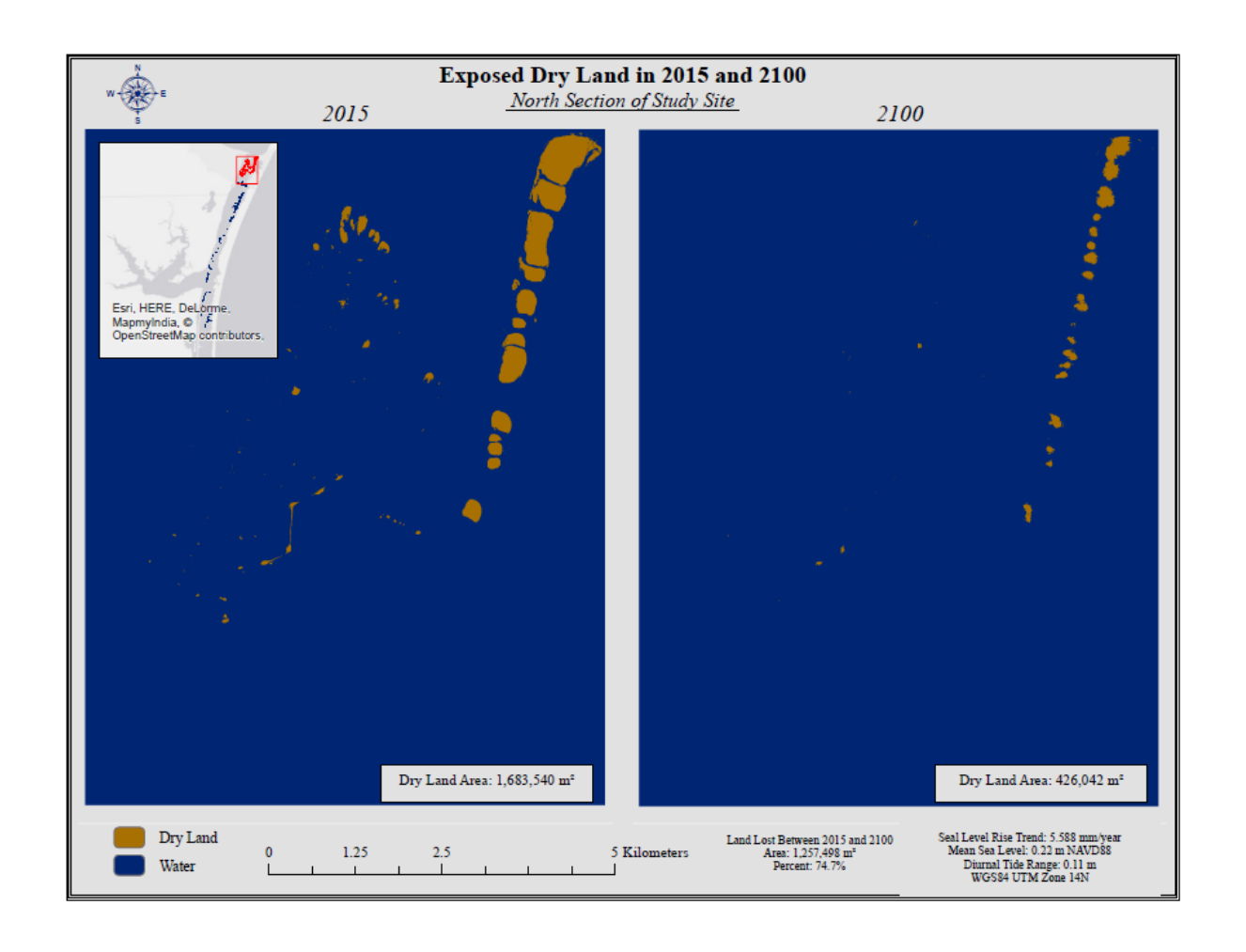


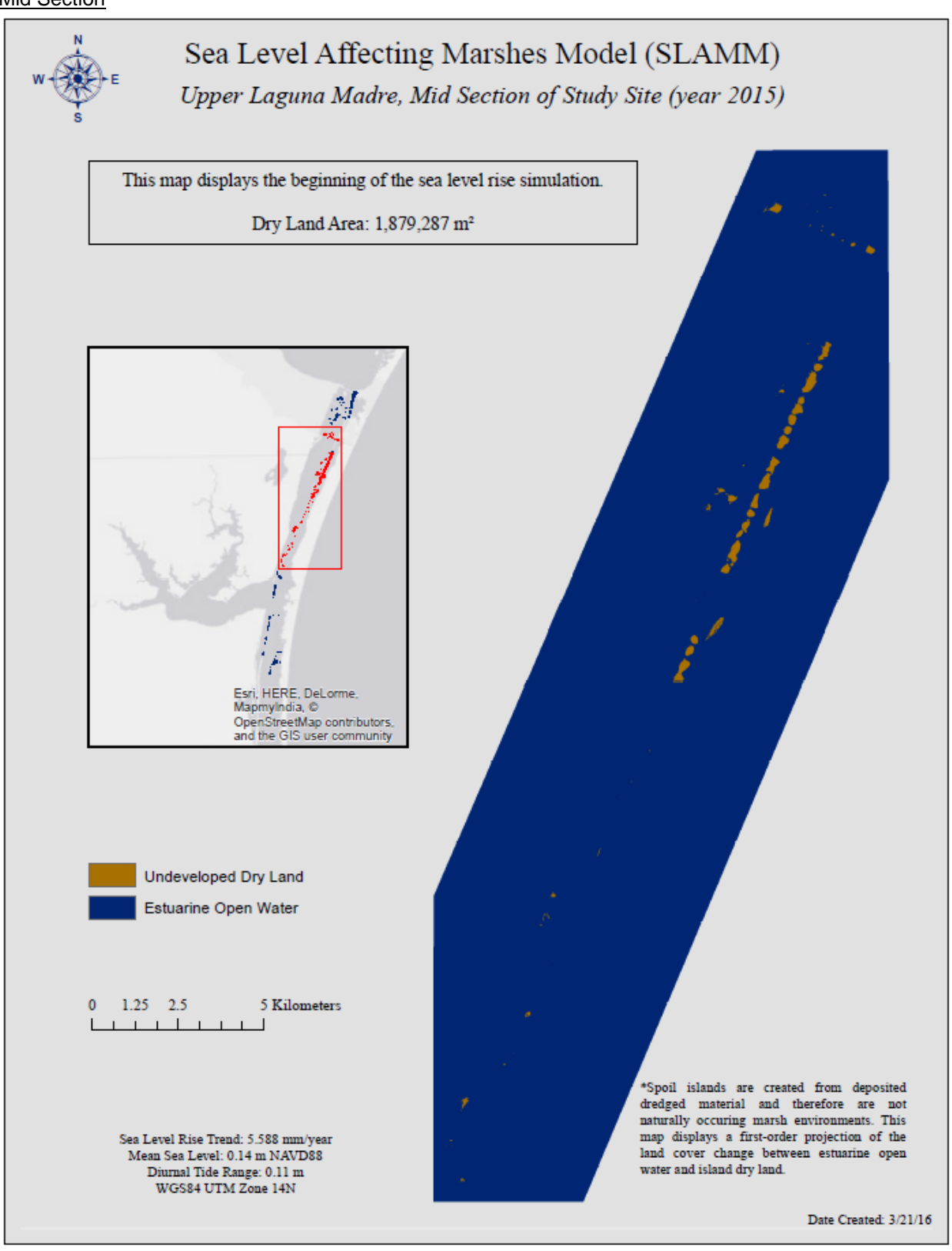
Upper Laguna Madre, North Section of Study Site (year 2100)

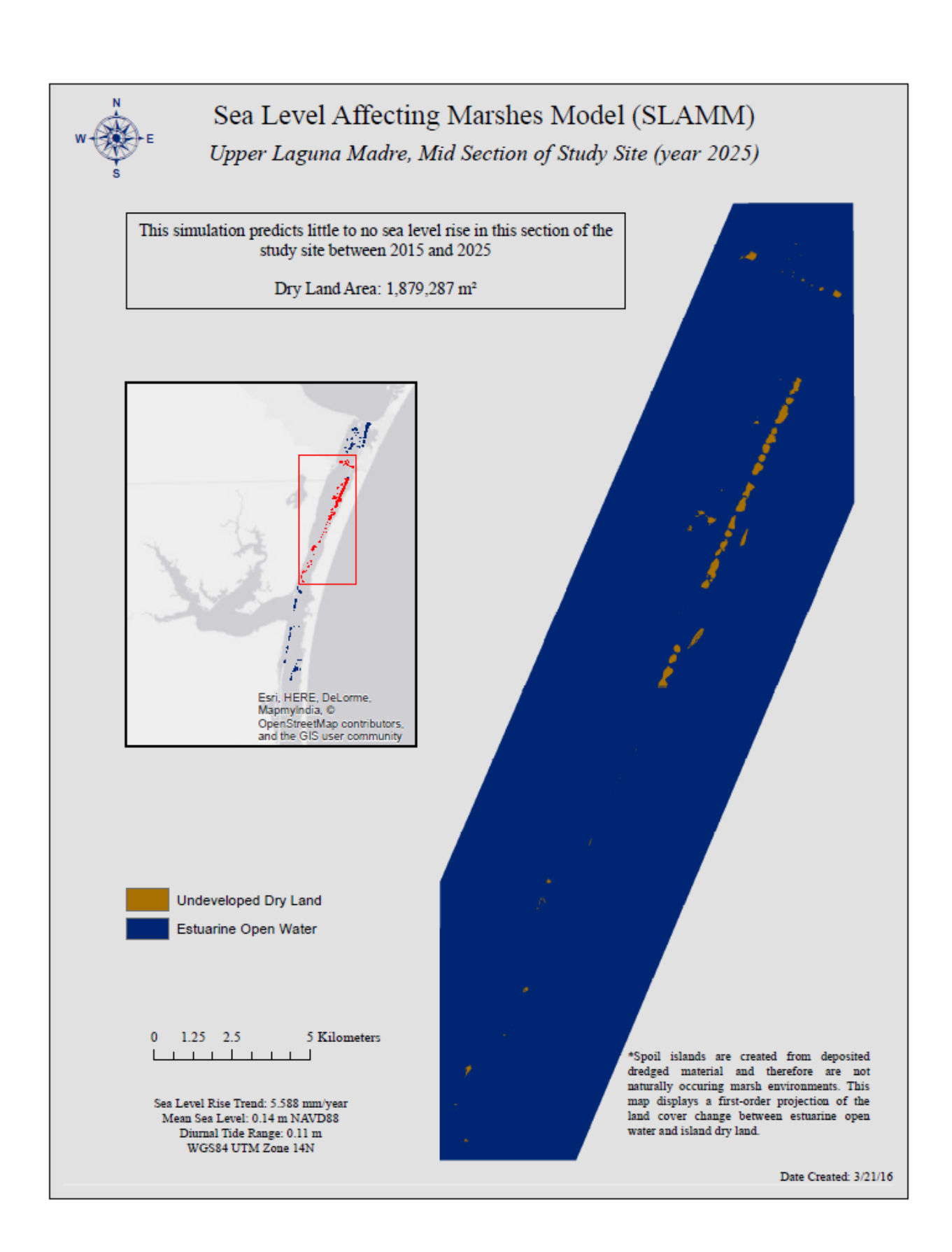


\*Values From 2015 to 2100 Dry Land Loss Dry Land Percent Loss
Transitional Marsh/Scrub Shrub 238,722 m² 14.18%
Regularly Flooded Marsh 461,470 m² 27.41%
Tidal Flat 546,693 m² 32.47%
Estuarine Open Water 10,613 m² 0.63%

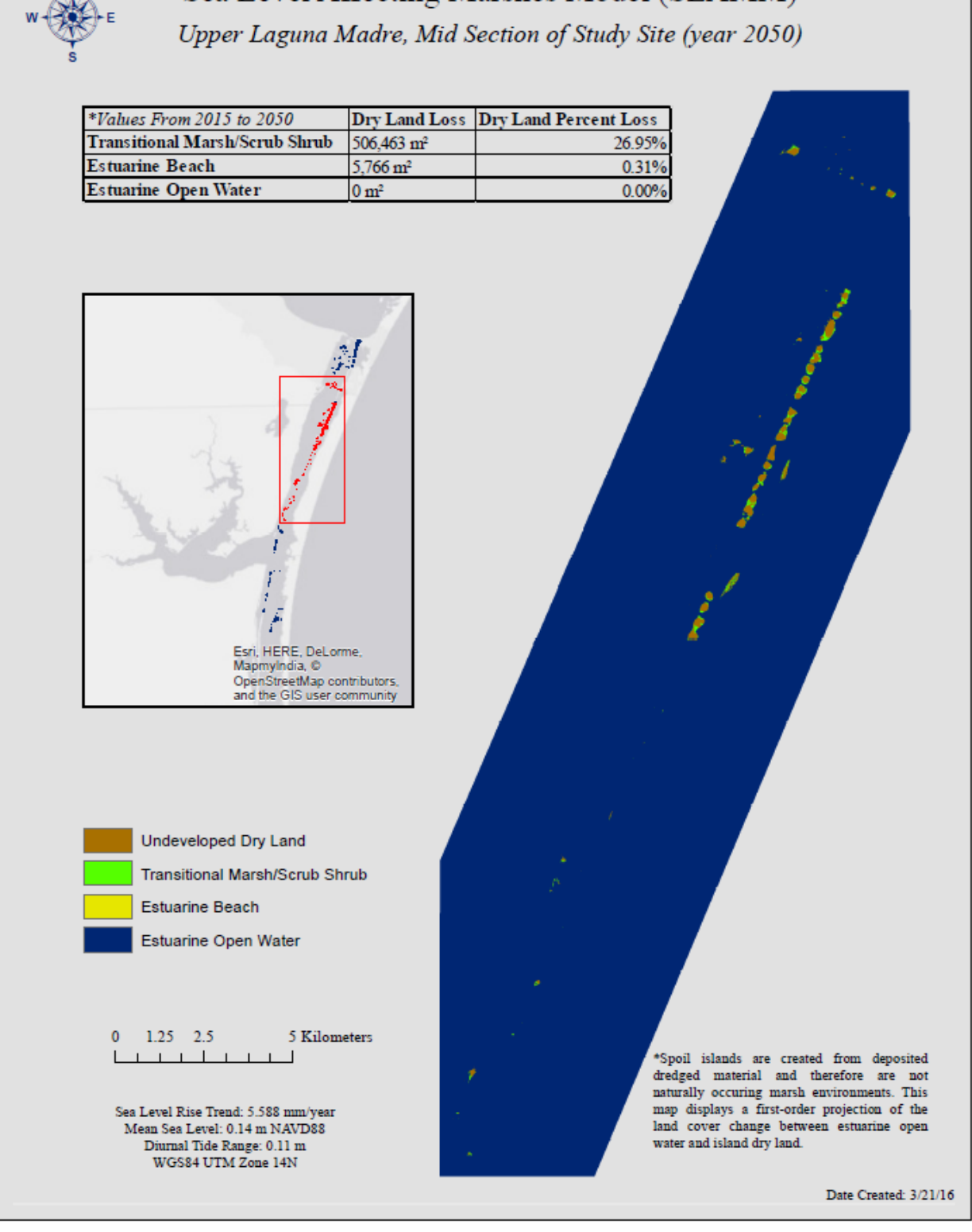
<sup>\*</sup>Spoil islands are created from deposited dredged material and therefore are not naturally occuring marsh environments. This map displays a first-order projection of the land cover change between estuarine open water and island dry land.



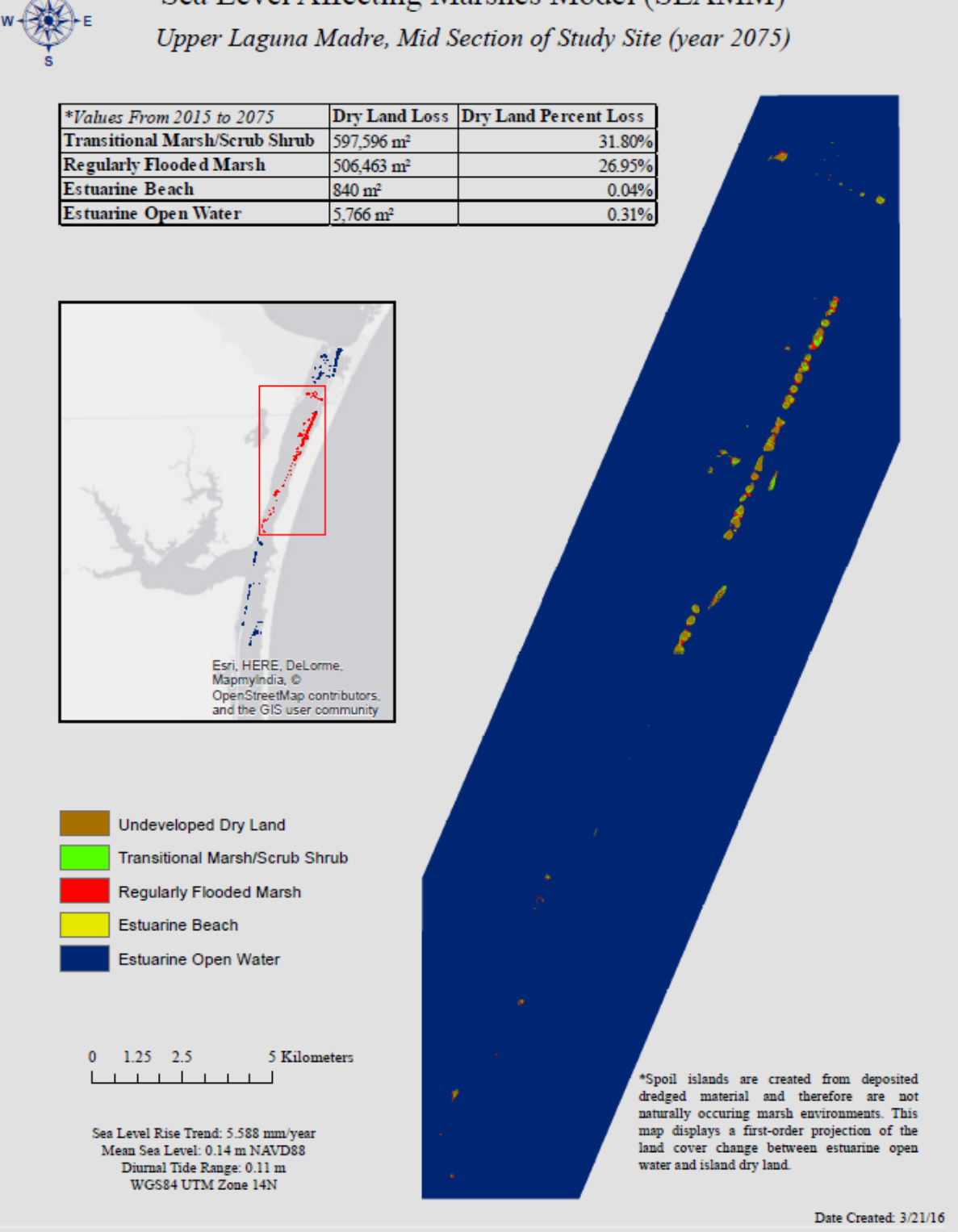








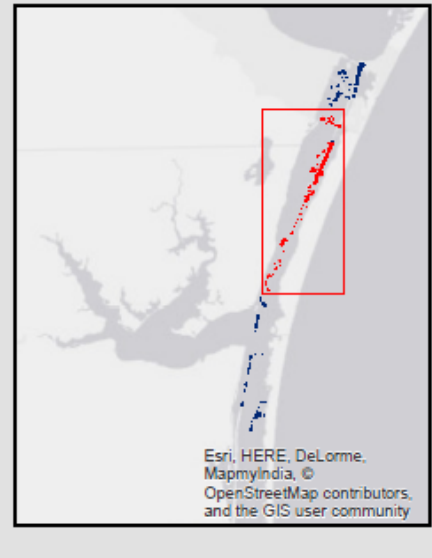






Upper Laguna Madre, Mid Section of Study Site (year 2100)

*Values From 2015 to 2100	Dry Land Loss	Dry Land Percent Loss
Transitional Marsh/Scrub Shrub	292,932 m <sup>2</sup>	15.59%
Regularly Flooded Marsh	597,596 m <sup>2</sup>	31.80%
Tidal Flat	506,463 m <sup>2</sup>	26.95%
Estuarine Beach	$618 \text{ m}^2$	0.03%
Estuarine Open Water	6,610 m <sup>2</sup>	0.35%





Transitional Marsh/Scrub Shrub

Regularly Flooded Marsh

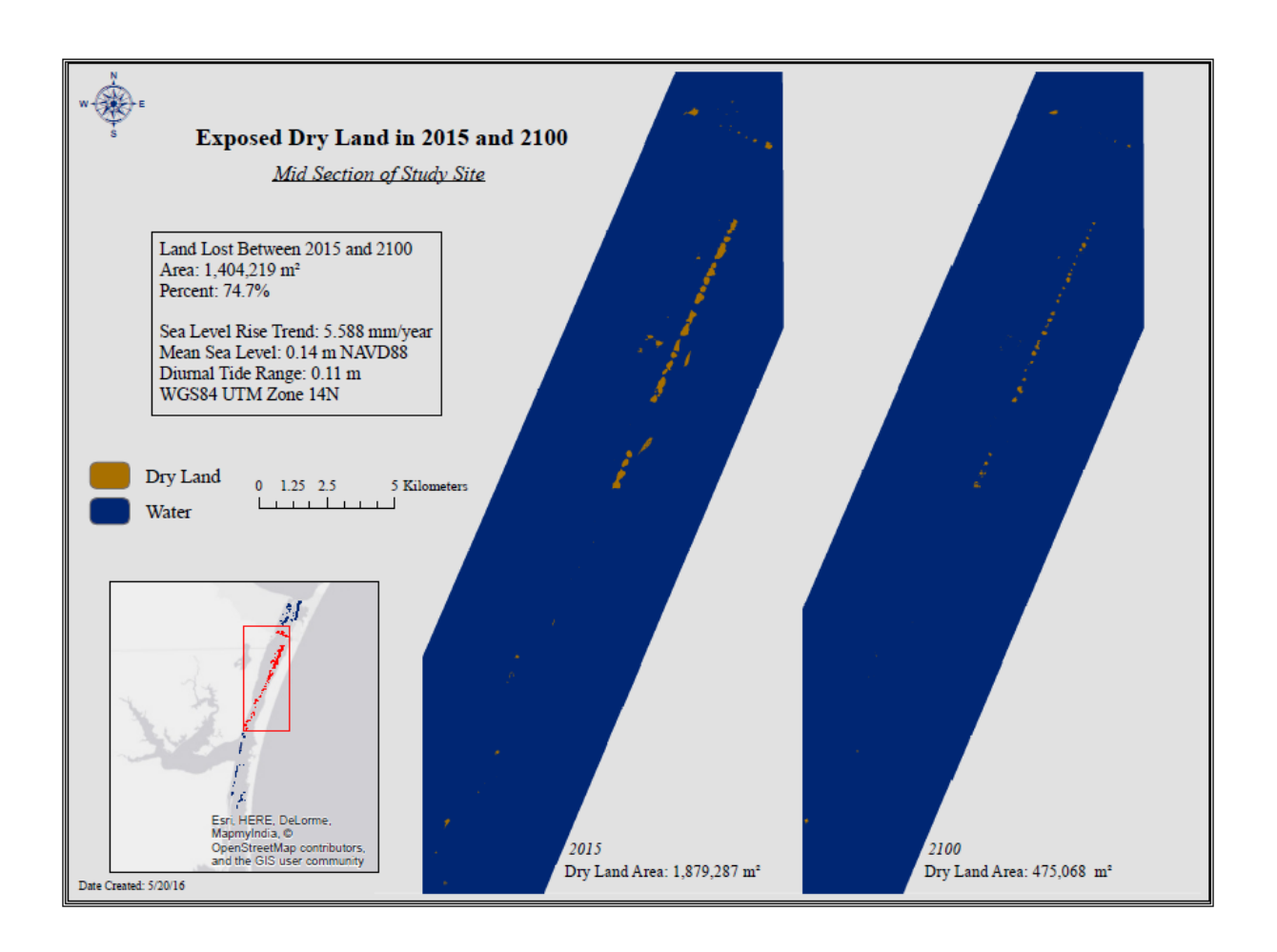
Estuarine Beach

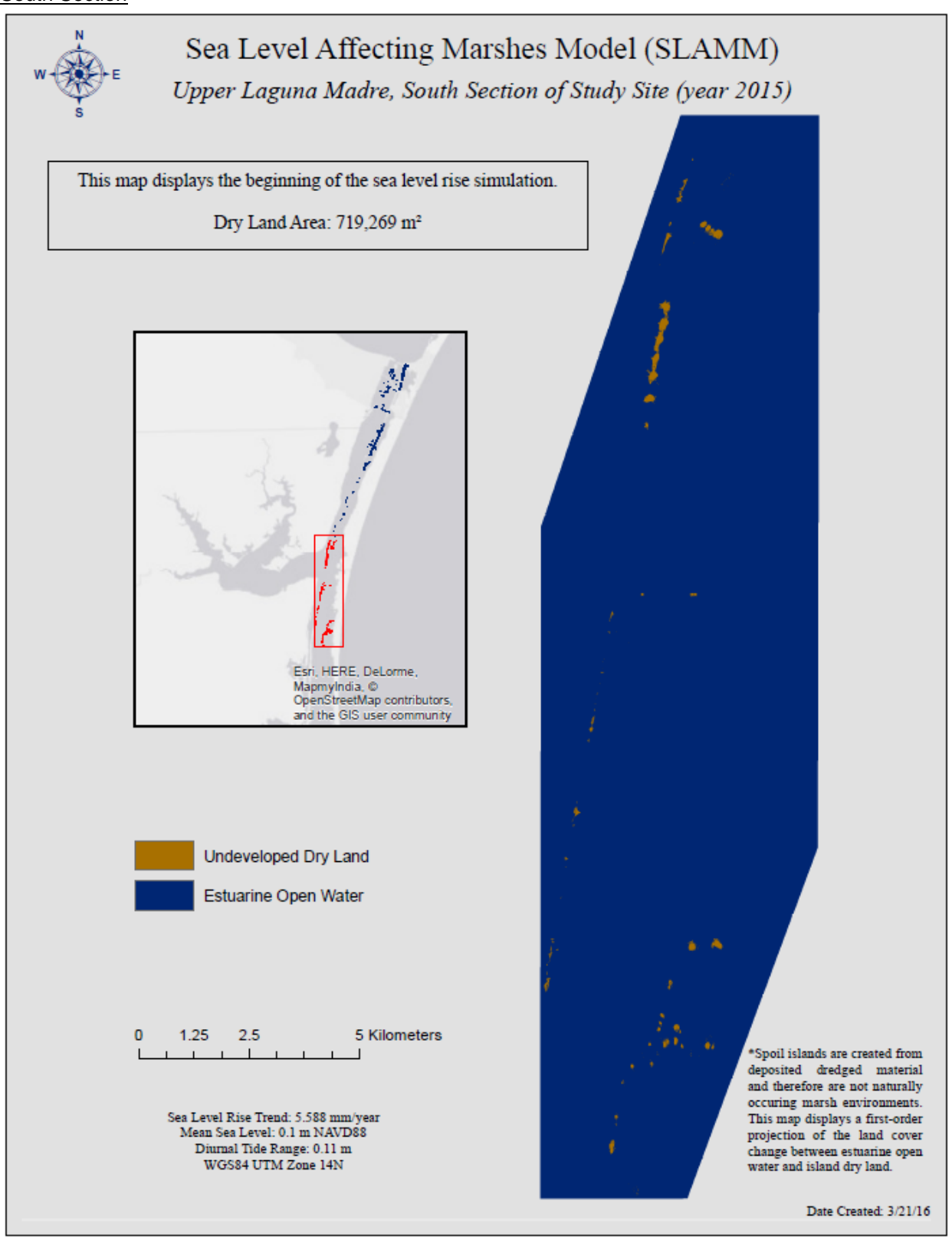
Tidal Flat

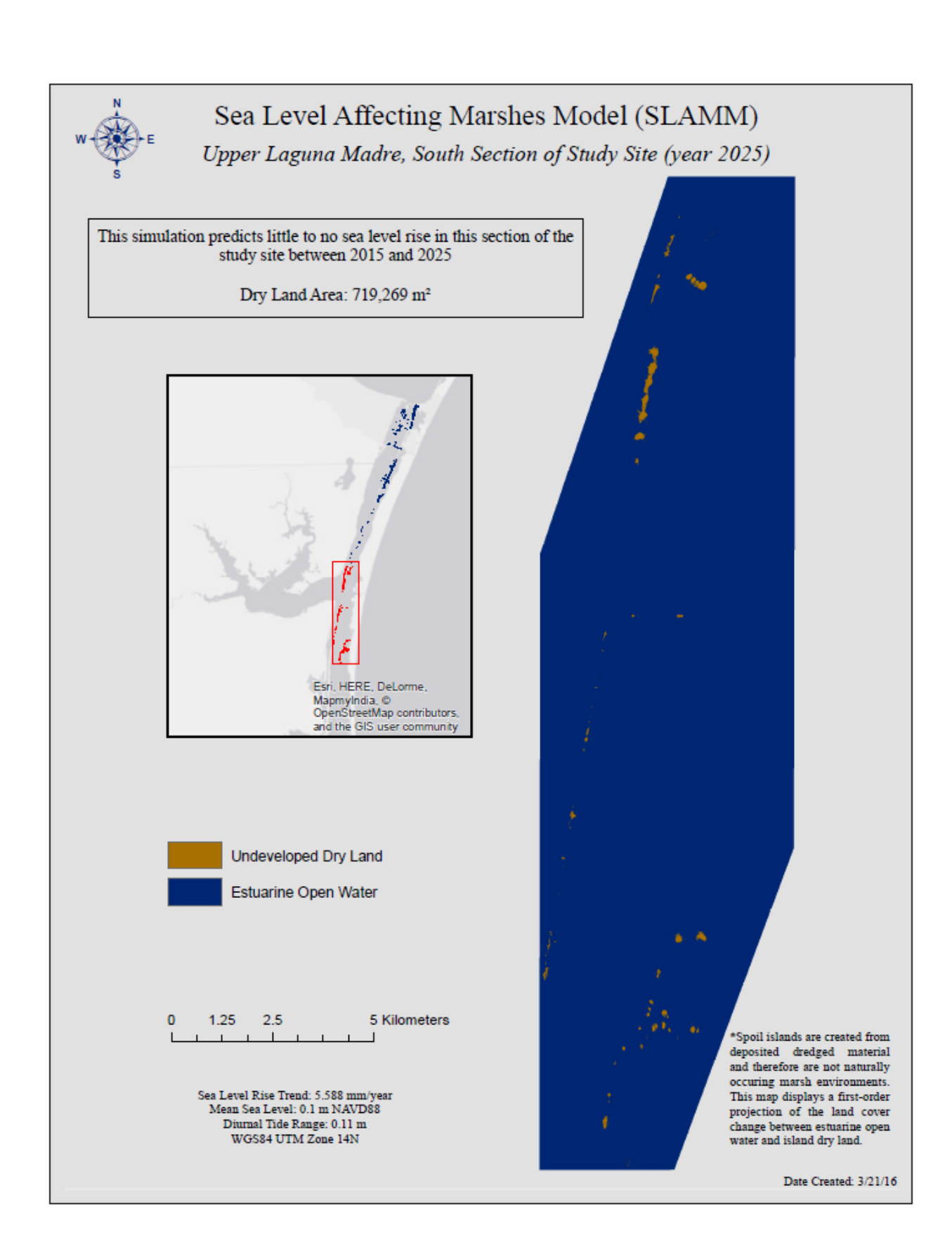
Estuarine Open Water

0 1.25 2.5 5 Kilometers

Sea Level Rise Trend: 5.588 mm/year Mean Sea Level: 0.14 m NAVD88 Diurnal Tide Range: 0.11 m WGS84 UTM Zone 14N \*Spoil islands are created from deposited dredged material and therefore are not naturally occuring marsh environments. This map displays a first-order projection of the land cover change between estuarine open water and island dry land.







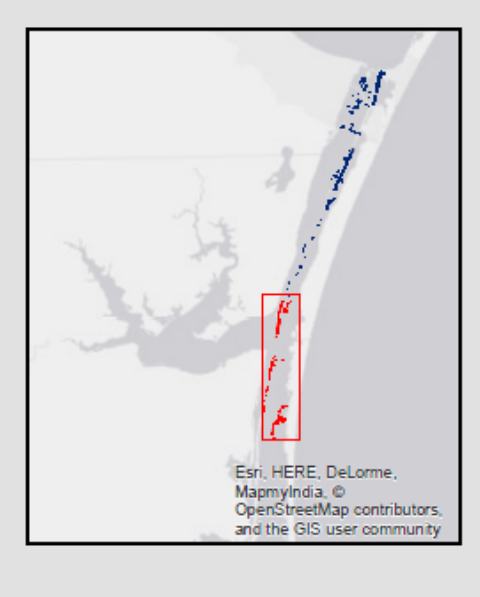


Sea Leve	l Affecting	g Marshe	s Model (SI	LAMM)	
W Upper Lagui	na Madre, So	uth Section	of Study Site	(year 2050)	
S					
*Values From 2015 to 2050	Dry Land Loss	Dry Land Per	cent Loss		
Transitional Marsh/Scrub Shrub	227851 m <sup>2</sup>	·	31.68%	1 4	
Estuarine Beach	1059 m <sup>2</sup>		0.15%	*	
Estuarine Open Water	$0 \text{ m}^2$	<u> </u>	0.00%	***	
	Esri, HERE, DeLorme, MapmyIndia, © OpenStreetMap contribu				
Estuarine Be Estuarine Op  0 1.25 2.5	Marsh/Scrub Shrul ach			* A Small inle	nds are created from
Sea Level Rise Trend: Mean Sea Level: 0.1 Diurnal Tide Rang WGS84 UTM Z	m NAVD88 ge: 0.11 m			*Spoil isla deposited and theref occuring r This map projection change be water and	nds are created from dredged material ore are not naturally marsh environments. displays a first-order of the land cover tween estuarine open island dry land.  Date Created: 3/21/16



Upper Laguna Madre, South Section of Study Site (year 2075)

*Values From 2015 to 2075	Dry Land Loss	Dry Land Percent Loss
Transitional Marsh/Scrub Shrub	199,622 m <sup>2</sup>	27.75%
Regularly Flooded Marsh	227,851 m <sup>2</sup>	31.68%
Estuarine Beach	19 m <sup>2</sup>	0.00%
Estuarine Open Water	1,059 m <sup>2</sup>	0.15%





Transitional Marsh/Scrub Shrub

Regularly Flooded Marsh

Estuarine Beach

Estuarine Open Water

2.5

1.25

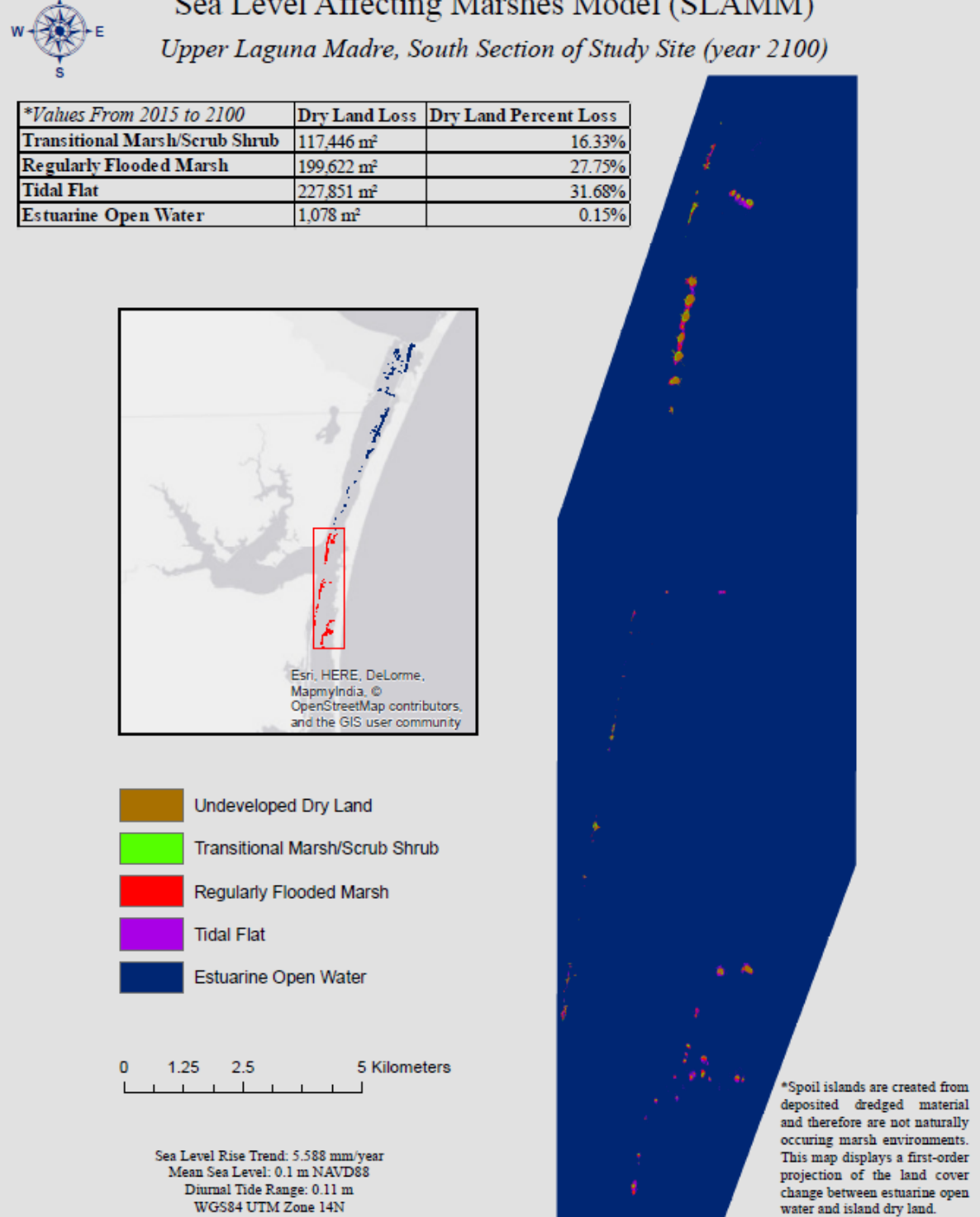
5 Kilometers

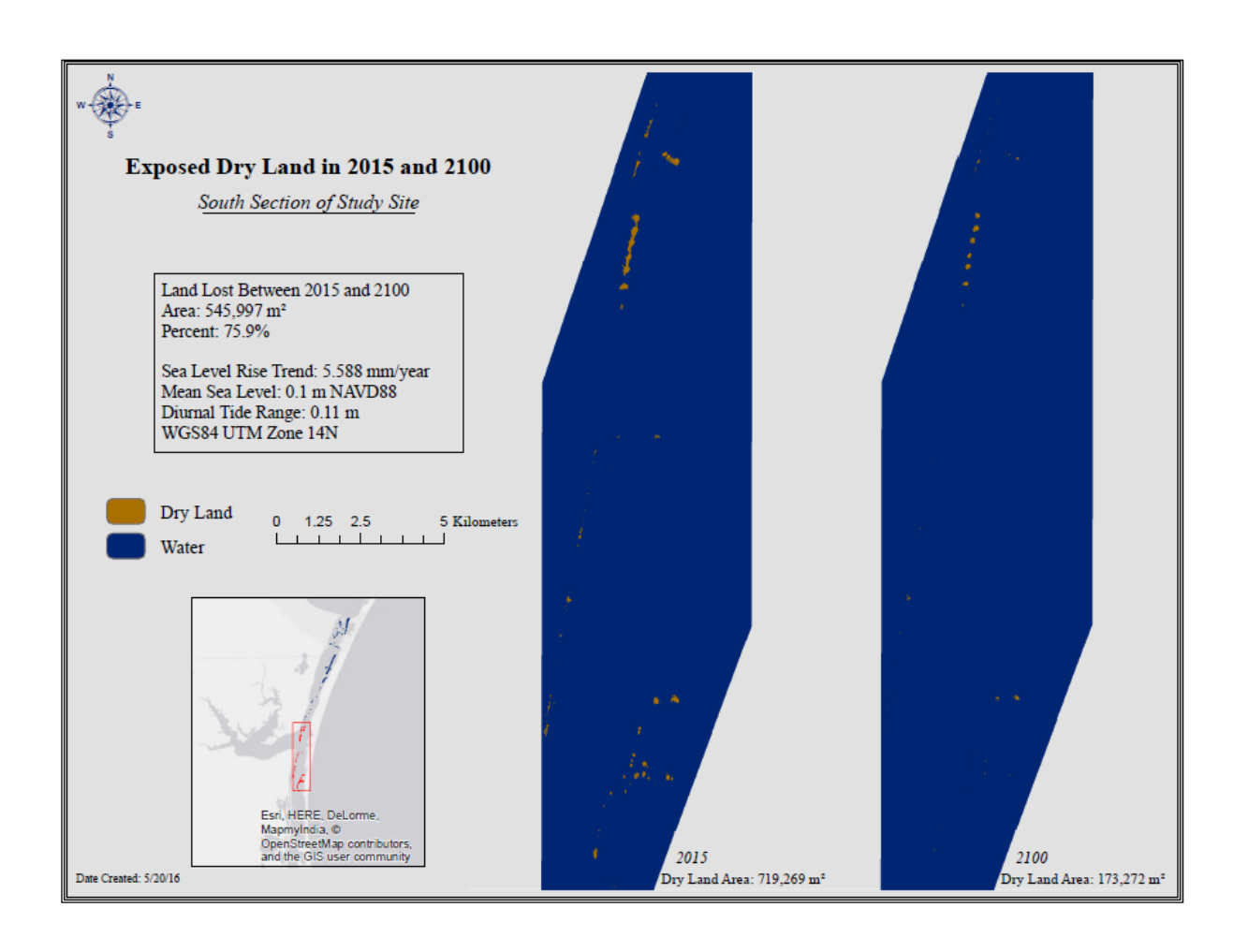
Sea Level Rise Trend: 5.588 mm/year Mean Sea Level: 0.1 m NAVD88 Diurnal Tide Range: 0.11 m WGS84 UTM Zone 14N



\*Spoil islands are created from deposited dredged material and therefore are not naturally occuring marsh environments. This map displays a first-order projection of the land cover change between estuarine open water and island dry land.







### **Appendix D.** Data Dissemination for Web Accessibility

Explanations of how the deliverables by task were shared are explained below. For more details on product deliverable times and dissemination dates, refer to the quarterly progress reports.

### Raw Lidar Data and Pipeline Segmentation GIS-Layer (Task 1 and 2)

All raw point cloud data provided to the team by the UT BEG have been directly shared to regional TGLO (Ms. Amy Nunez) and TGLO headquarters in Austin (Ms. Julie McEntire). The raw survey data have also been shared directly with NOAA digital coast. NOAA provided an external drive (received on June 30, 2016) to upload the data and send back to them for distribution. At the time of this report, the data is in process of being sent back to NOAA. From there, accessing of the data via Digital Coast will depend on NOAA's timeframe for distribution. The submerged structure/pipeline GIS-layer from Task 2 was directly provided to the regional TGLO stakeholder (Ms. Amy Nunez) as well as shared directly with TGLO headquarters in Austin, TX.

### Lidar-derived DEMs, DSMs, Polygon Shapefiles of Rookery Islands (Task 3 and 4)

These data are hosted on the Harte Research Institute for Gulf of Mexico Studies' GOMA portal and searchable by using a key word such as "Laguna Madre" (see image below).

### Link to GOMA portal:

http://gomaportal.org/geoportal/

### Direct links to download the data

SHP - ftp://gomaftp.tamucc.edu/Texas/bird\_rookeries\_monitoring\_tamucc\_2016.zip

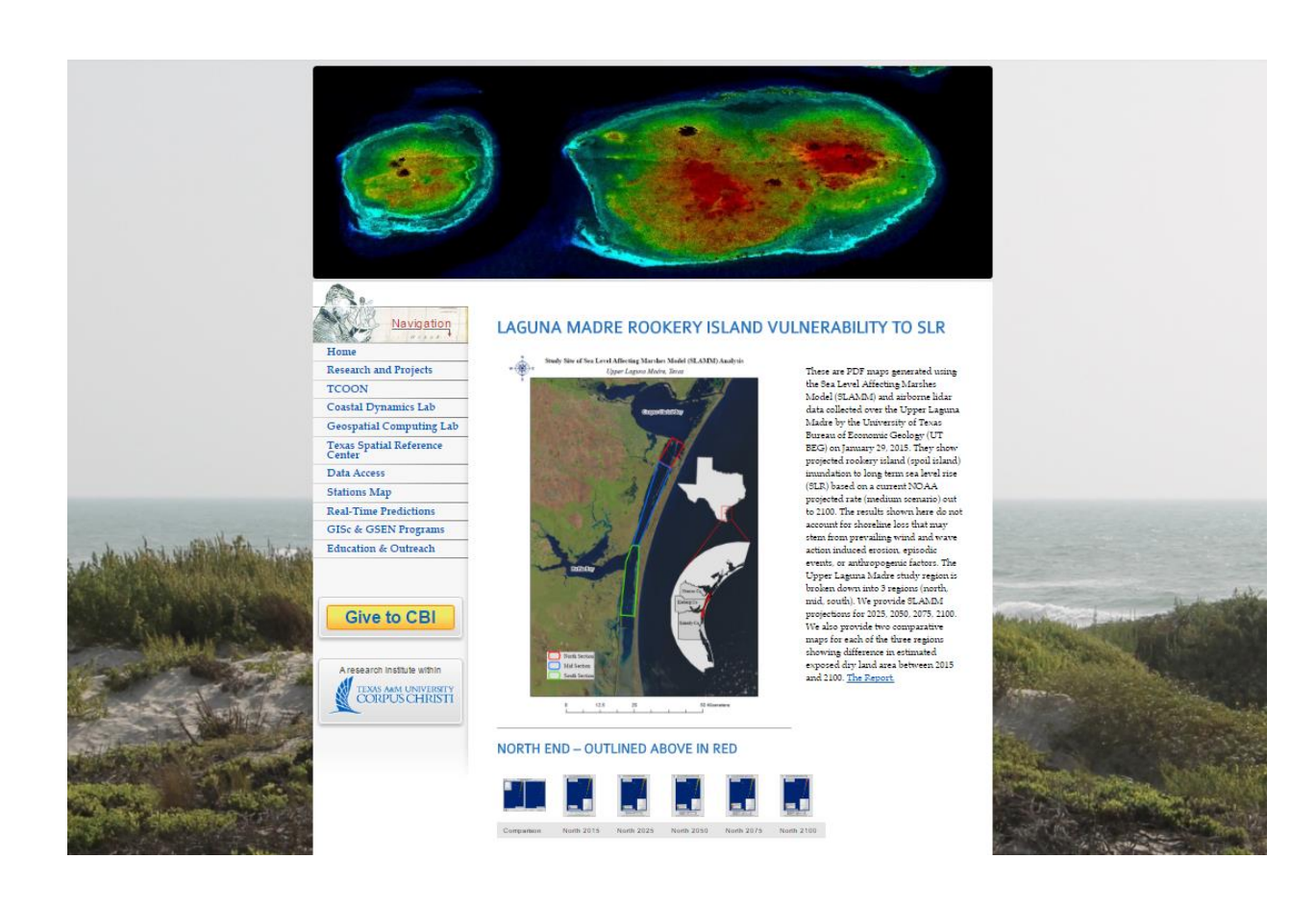
DEMs - ftp://gomaftp.tamucc.edu/Texas/rookery island monitoring 1m dem tamucc 2015.zip

DSMs - ftp://gomaftp.tamucc.edu/Texas/rookery\_island\_monitoring\_1m\_dsm\_tamucc\_2015.zip



### Rookery Island Sea Level Rise Vulnerability Maps (Task 5)

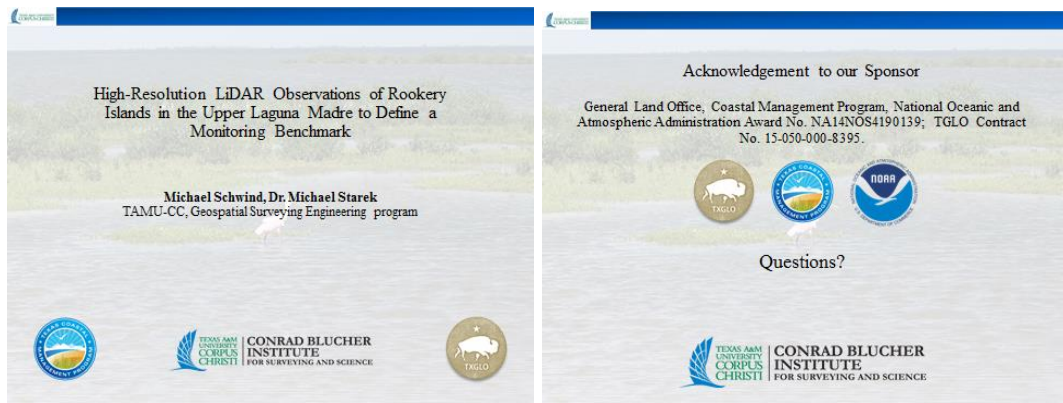
These maps are shared as PDFs downloadable from a website created and hosted by the Conrad Blucher Institute at TAMUC-CC for this project. Here is a link to the website (see image below): <a href="http://www.cbi.tamucc.edu/rookeryslr/">http://www.cbi.tamucc.edu/rookeryslr/</a>



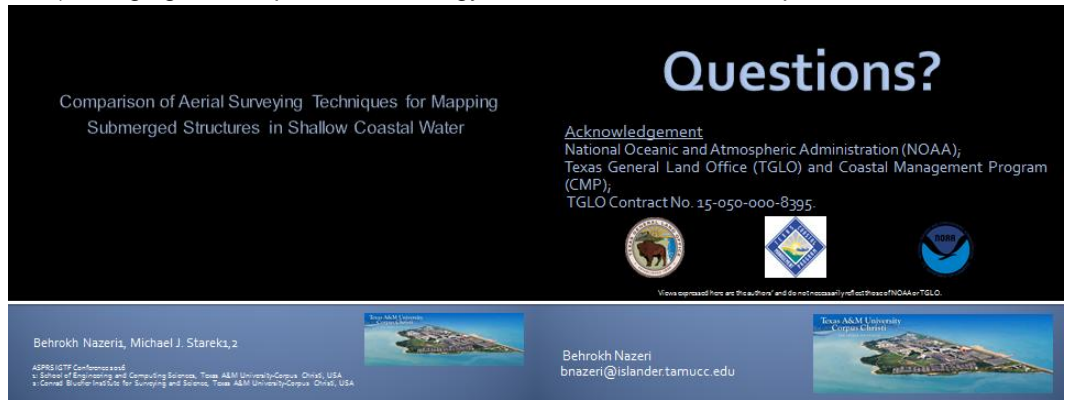
### **Appendix E.** Conference Presentations and Publications

The following lists student technical conference presentations and publications resulting from this project:

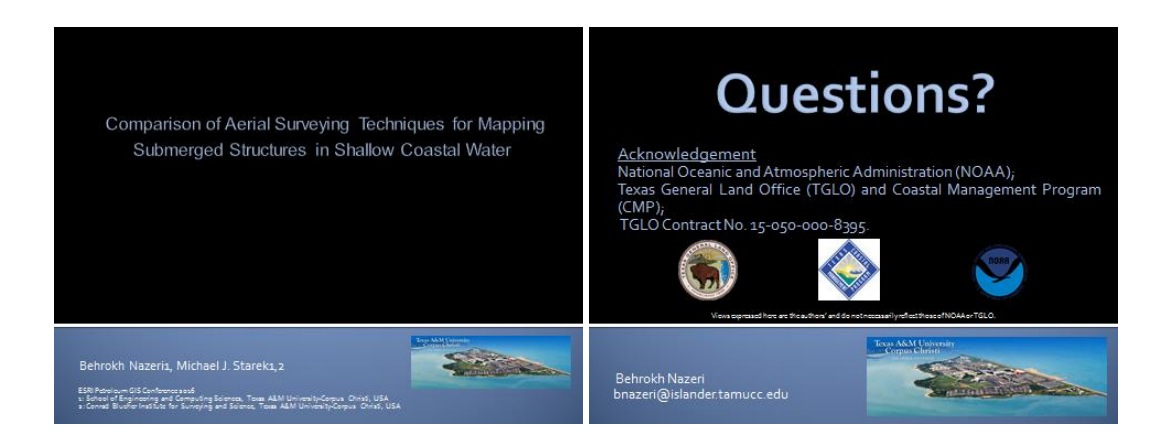
 M. Schwind and M.J. Starek, High-resolution Lidar Observations of Rookery Islands in the Upper Laguna Madre to Define a Monitoring Benchmark, American Society of Photogrammetry and Remote Sensing (ASPRS), Imaging & Geospatial Technology Forum, Fort Worth, TX April 11-15, 2016.



 B. Nazeri and M.J. Starek, Comparison of Aerial Surveying Techniques for Mapping Submerged Structures in Shallow Coastal Water, American Society of Photogrammetry and Remote Sensing (ASPRS), Imaging & Geospatial Technology Forum, Fort Worth, TX April 11-15, 2016.



 B. Nazeri and M.J. Starek, Comparison of Aerial Surveying Techniques for Mapping Submerged Structures in Shallow Coastal Water, ESRI Petroleum and Gas GIS Conference, Houston, TX April 26-28, 2016.



 B. Nazeri, under the direction of M.J. Starek, Comparison of Airborne Surveying Techniques for Mapping Submerged Objects in Shallow Water, Master's Thesis in Geospatial Surveying Engineering at Texas A&M University-Corpus Christi, 2016.

